DEVELOPMENT OF MR-FLUID BASED SEMI-ACTIVE DAMPERS TO BE USED IN HAPTIC DEVICES

A Thesis Submitted to
the Graduate School of Engineering and Science of
İzmir Institute of Technology
in Partial Fulfillment of the Requirements for the Degree of

MASTER OF SCIENCE

in Mechanical Engineering

by
Mehmet Görkem KARABULUT

July 2017
İZMİR

We approve the thesis of **Mehmet Görkem KARABULUT**

Examining Committee Members:

Assoc. Prof. Dr. M. İ. Can DEDE
Department of Mechanical Engineering, İzmir Institute of Technology

Assist. Prof. Dr. Barbaros ÖZDEMİREL
Department of Mechanical Engineering, İzmir Institute of Technology

Assist. Prof. Dr. Fatih Cemal CAN
Department of Mechatronics Engineering, İzmir Katip Celebi University

31 July 2017

Assoc. Prof. Dr. M. İ. Can DEDE
Supervisor, Department of Mechanical Engineering, İzmir Institute of Technology

Prof. Dr. Metin TANOĞLU
Head of the Department of Mechanical Engineering

Prof. Dr. Aysun SOFUOĞLU
Dean of the Graduate School of Engineering and Sciences

DEDICATION

I dedicate this thesis to my parents, my sister and my dear aunt, Fatma Mulla.

ACKNOWLEDGMENTS

I would like to express my sincere appreciation and gratitude to my supervisor Assoc. Prof. Dr. M. İ. Can Dede for his guidance and patience during the M.Sc. Thesis study. His excellent guidance enlightens and helps me to accomplish this thesis.

I would like to thank to Prof. Serhan Özdemir, Assist. Prof. Gökhan Kiper and Assoc. Prof. H. Seçil Artem for their guidance and help during the M.Sc. courses.

I also thank to my dear friends in IZTECH Robotics Laboratory, Barış Taner, Emre Uzunoğlu, Osman Nuri Şahin and the others for their support and friendship.

Particularly, I would like to express my gratitude to my parents and sister for their continuous support and faith in me. I owe gratefulness to my girlfriend for her support and companionship. I would not be able to succeed without their love and support.

This thesis is partially supported by The Scientific and Technological Research Council of Turkey via grant number 115E726.

ABSTRACT

DEVELOPMENT OF MR-FLUID BASED SEMI-ACTIVE DAMPERS TO BE USED IN HAPTIC DEVICES

In this thesis, development of a novel Magneto-Rheological (MR) fluid based brake system is described which is designated to be used in kinesthetic haptic devices. The new design of MR-brake system consists of two identical directional brakes and with this feature, it presents a solution to the stiction problem that occurs when the MR-brake is activated which constrains the rotational motion in both direction. This constraint of the motion results in developing a feeling that the user is stuck in the virtual wall. By using two independently controlled brakes in a system, the rotational brake direction is controlled and thus the motion of the handle is constrained in one direction while the user is free to move the handle in the reverse direction.

MR-brake is developed from a conceptual design to the final design by applying a design optimization method. This method incorporates the use of Finite Element Analysis (FEA) and mathematical model of the system. Using this method, it is possible to predict the performance of the design to check if it meets the requirements that are specified by considering the future use of the device. After manufacturing a prototype, its performance is experimentally validated in a test rig which is also constructed in the scope of this thesis study.

Experimental study includes two sections as characterization and frequency response test. As a result, the prototype is characterized with constructing the torque-current relation, which clearly shows the expected hysteresis in operation. The control model of the system is mathematically modeled with %95 accuracy ratio using the obtained experimental results. Experimental results show that the maximum brake torque of the system is 3.84 Nm and the minimum torque value is 0.15 Nm. The frequency response of the system is experimentally investigated and using this result, the system's transfer function is estimated and its bode diagram is drawn. According to this result, the bandwidth of the system is calculated to be 63 rad/s.

ÖZET

HAPTİK CİHAZLARDA KULLANILMASI İÇİN MR-SIVISI BAZLI YARI-AKTİF DAMPER GELİŞTİRİLMESİ

Bu tezde, kinestetik haptik cihazlarda kullanılmak üzere geliştirilen Magneto-Reolojik (MR) sıvısı ile çalışan özgün bir fren sisteminin tasarımı anlatılmaktadır. MR fren sisteminin yeni tasarımı, iki adet tek yönde çalışan frenlerin bir araya gelmesinden oluşmaktadır ve bu özellik ile MR frenin aktif olduğunda rotasyon hareketini iki yönde sınırlamasından ortaya çıkan takılma sorununa bir çözüm sunmaktadır. Hareketin sınırlanması, kullanıcıda sanal bir duvarda takılma hissi meydana getirmektedir. Birbirinden bağımsız olarak kontrol edilebilen iki ayrı frenden oluşan sistem sayesinde, fren yapılacak olan dönüş yönü kontrol edilebilir ve bu sayede kullanıcı tek yönde serbest şekilde hareket edebilirken diğer yönde sınırlandırılmış olur.

MR freni konsept tasarımdan final tasarımına, tasarım optimizasyon metodu uygulanarak geliştirilmiştir. Bu metot sonlu elemanlar analizi (FEA) ve sistemin matematik modelini içermektedir. Bu metodu kullanarak, geliştirilen sistemin performansının gelecekteki kullanım hedeflerini karşılayıp karşılamadığını tahmin etmek mümkün olmaktadır. Prototip üretildikten sonra, sistemin performansı bu tez kapsamında oluşturulan bir test düzeneği ile deneysel olarak doğrulanmıştır.

Deneysel çalışma, sistemi karakterize etme ve frekans davranışlarının incelenmesi olmak üzere iki kısımdan oluşmaktadır. Sonuç olarak, sistemin karakteri, beklenilen histerezis etkisinin de açıkça gösterildiği akım ve tork ilişkisi ile ortaya çıkarılmıştır. Elde edilen deneysel sonuçlar kullanılarak sistemin kontrol modeli yüzde 95'lik doğruluk oranı ile matematiksel olarak modellenmiştir. Deneysel sonuçlar, sistemin maksimum tork değerinin 3.84 Nm ve minimum tork değerinin 0.15 Nm olduğunu göstermektedir. Sistemin tepkisi farklı frekanslarda deneysel olarak incelenmiş ve buradan elde edilen sonuç ile sistemin transfer fonksiyonu elde edilerek bode şeması oluşturulmuştur. Bu sonuçlara göre sistemin bant genişliği 63 rad/s olarak hesaplanmıştır.

TABLE OF CONTENTS

LIST OF FIGURES

Figure **Page**

LIST OF TABLES

CHAPTER 1

INTRODUCTION

The use of a motor-transmission system is a common solution in haptic device design since it can be used to apply forces/torques to the user and at the same time it can be used to provide a dynamic motion whenever necessary. Since the DC motor modeling is well studied and the capstan transmission systems are proven to provide smooth operation, most of the commercially available haptic devices are constructed by using this actuator-transmission system.

In kinesthetic haptic devices, a greater portion of power spent is for displaying a rigid/stiff constraint. This fact causes problems in terms of stability and calls for cautious design procedure in order to meet the passivity equation below (Colgate & Brown, 1994).

$$b > \frac{K}{2f} + B \tag{1.1}$$

In the above equation b is the physical damping in the system K and B parameters are the maximum stiffness and damping that can be rendered in virtual environment and f is the sampling frequency. Therefore, to simulate higher stiffness with the haptic device either the physical damping or the sampling frequency should be increased. However, the increase in the physical damping would affect the minimum impedance of the device adversely.

One solution to the above problem is including a component that can provide variable physical damping to the system. It was introduced in (An & Kwon, 2004) that the additional variable damping to the system can be provided by using a magneto-rheological (MR) fluid based damper. In this case, (1.1) is revised to the following equation.

$$b + b_c(H) > \frac{K}{2f} + B \tag{1.2}$$

In the above equation $b_c(H)$ is the additional damping provided by the MR-fluid based damper, which is a function of the magnetic field, H. The use of this component

removes the adverse effect of increase in the minimum impedance while providing much higher stiffness values with respect to commonly used motor-transmission systems.

Magneto-rheological fluid is a smart material which can exhibit different rheological characteristic if the fluid is exposed to the magnetic field. With the effects of magnetic field, the magnetic particles (usually iron particles) inside the carrier fluid align through the magnetic flux direction (Figure 1.1.). The alignment of these particles changes viscosity of the fluid and the phase of the fluid to semi-solid form. Therefore, it is possible to vary the yield stress by changing the current on the coil that provides the magnetic field.

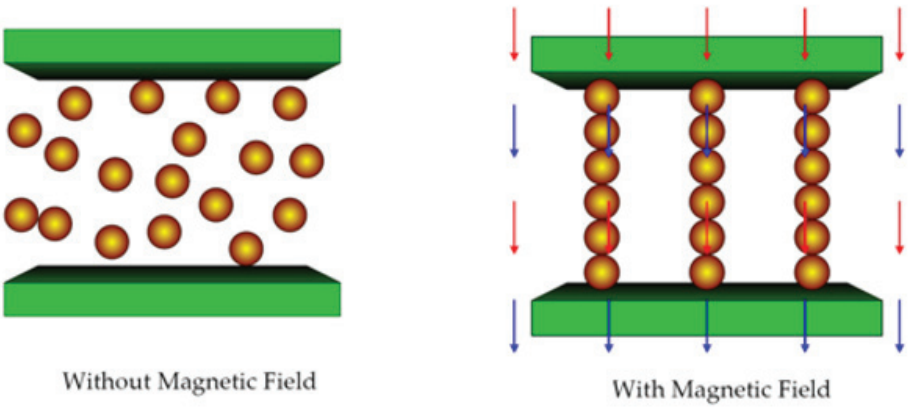

Figure 1.1. MR-fluid behavior with the magnetic field
(Source: Truong & Ahn, 2012).

The controllable viscosity based damping provided with MR-fluid is used for developing clutch, brake and damper systems. In terms of haptic device development, MR-fluids are usually used as brake systems that can provide a range of brake forces. In the previous works, the design of an MR-brake based haptic device is explained in detail (B. Liu, Li, Kosasih, & Zhang, 2006) and a multi degree-of-freedom (DoF) haptic device was built by using an MR-fluid based design (Senkal & Gurocak, 2009). Some researchers even used the MR-brakes along with the conventional motor-capstan drive systems (Samur et al., 2008) in order to increase the Z-width of the device by increasing the maximum stiffness of the system.

As an initial study of this thesis, a haptic paddle Figure 1.2 (a) is designed and manufactured. Although this haptic device has 1-DoF, it is constructed with two MR-brake systems that consists of a clutch and a one-way bearing. The idea of design here is that the MR-brakes work in opposite directions in order to avoid restricting motion in both directions when the MR-fluid is activated. This work has been published and presented in a national conference (Karabulut, Taner, & Dede, 2015).

Although the haptic paddle solves the stiction problem with its mechanical properties, it is required to be redesigned in order to develop an MR-brake that can adapt to the high precision haptic device (HIPHAD), which was previously built in IZTECH robotics lab, for further study (Bilgincan, Gezgin, & Dede, 2010). First version of HIPHAD. To do so, the MR clutch and the one-way bearing are coupled in a compact MR-brake. Then, two of the brakes are mounted to the same shaft as seen in Figure 1.2 (b). As a result, the total width of the haptic paddle (each MR-brake diameter is 126 mm) decreased from 262 mm to the diameter of the new MR-brake which is 80 mm. The study of the new design of the MR-brake is presented as a Work-in-Progress in IEEE World Haptics 2017.

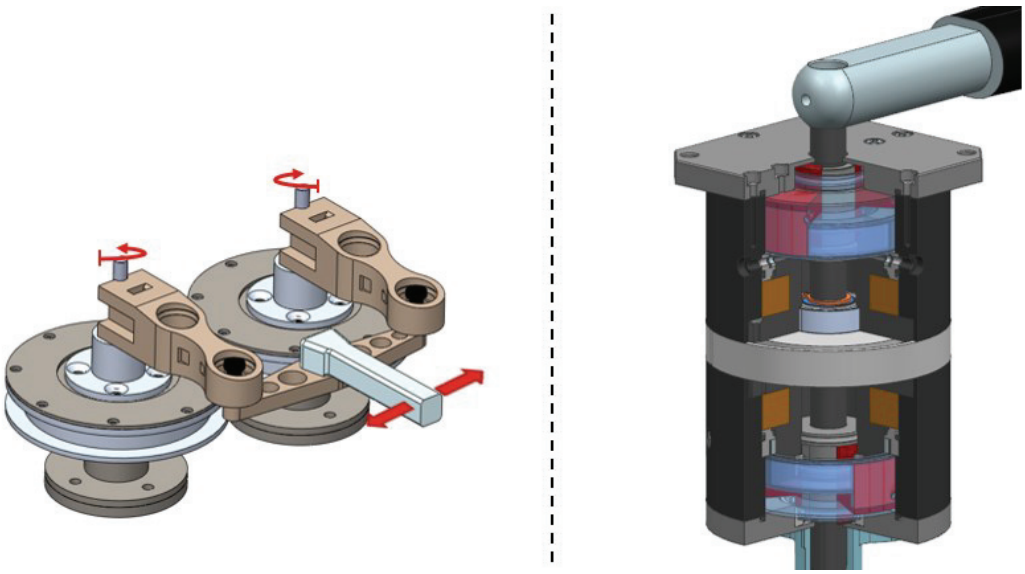

(a) (b)

Figure 1.2. 3D model of (a) Haptic paddle (Source: Karabulut et al., 2015), (b) Bidirectional MR-brake.

1.1. Thesis Objective and Motivation

Based on the literature survey, the common problem with MR-fluid based haptic devices is identified as unwanted stiction sense when a conventional MR-brake is activated. The reason for this is that once the MR-brake is activated to constrain the motion in one direction, although the user wants to move in the other direction, the motion in the other direction is also constrained. This phenomenon is called sticky wall (Rosenberg & Adelstein, 1993) and stiction problem (An & Kwon, 2008) in MR-fluid based haptic devices.

There have been studies performed to overcome this problem, e.g. Kwon and Song (2006) adapted a force sensor to sense the force applied by the user, and Rossa, Lozada, and Micaelli (2014) developed an hybrid MR-brake by using DC motor beside bi-directional MR-brake additionally. However, this thesis aims to provide a novel solution in the MR-brake design which cancels out the stiction problem without the need of any other active components or software precautions.

The main objectives of this thesis are:

1. Design and development of a new type MR-brake that solves the stiction problem.
2. Optimize the design with a method consisting of FEA simulation and analytical model.
3. Selection of proper material considering the structural, thermal and magnetic properties
4. Determination of the design specifications of the MR-brake such as type, number of disc or drum, sealing and the coil.
5. Construction of a prototype using the final 3D model.
6. Performing experimental tests to characterize and validate MR-brake whether the prototype meets the requirements.

1.2. Main Contributions

The main contributions of this thesis are listed as follows:

1. Propose a possible solution for the stiction problem.

As mentioned earlier, there is a common problem of using MR-fluid based actuators in the haptic devices. The idea of using one-way bearing along with the MR-brake results in avoiding motion restrictions caused by the MR-fluid solidification and solves the stiction problem without the need of any other equipment.

2. Design optimization and compression of design configuration of the MR-brakes.

An optimization method using FEA simulation and analytical calculations is studied. This method is applied for possible MR-brake models. These models are created to compare the design configurations such as type of the MR-brake (disc or drum), MR-fluid gap, disc or drum thickness, coil size and placement. Then, the outcome of this work is used to achieve optimal dimensioning in the design process.

3. Experimental characterization and validation of the MR-brake prototype.

The performance of the MR-brake is calculated using the method previously mentioned. However, the simulation results must be validated and the system should be characterized by experimentally testing the prototype. Furthermore, using the experimental test setup, the torque-current relation of the MR-brake prototype is obtained to be used in a haptic application.

1.3. Thesis Outline

This thesis consists of 6 chapters; Introduction, Literature Review, Design Methodology, Design of the MR-brake, Experimental Validation and Conclusion.

In Chapter 2, a comprehensive overview of the haptic technology is given and the terms related with the stiffness and the Z-width are emphasized. Haptic devices are investigated according to their actuation types. Since the MR-fluid based actuators are strong candidate to current actuation types, MR-fluid based haptic devices are researched.

In Chapter 3, design configuration of MR-brakes are briefly introduced. These design configurations are comparatively investigated in terms of the performance. For this purpose, an optimization method that includes FEA simulation and analytical calculation methods is used.

Chapter 4 discusses the design process and requirements. The design process mainly consists of conceptual design, design optimization and verification. Then, following this procedure, a new type of MR-brake is designed and developed. All steps of development process are presented.

In Chapter 5 experimental test results are presented. The test setup is constructed to characterize the prototype and validate the torque calculation method that combines the FEA simulation and analytical calculations. Furthermore, the manufacturing of the prototype is explained.

The conclusion of this thesis work is presented in Chapter 6. Additionally, the possible improvements to achieve a high performance within an optimized volume is discussed.

CHAPTER 2

LITERATURE REVIEW

Haptics is derived from the Greek word '*haptios*' which describes the sense of touch. Human haptic perception consists of two sensations as kinesthetic related to force and position, and tactile (cutaneous). Kinesthetic sensory receptors are located in muscle fibers and body joints that capture body motion and forces. Tactile receptors exist intensely in human skin which provide cutaneous sensations such as temperature, pressure, shear, vibration and contact location. Both sensations help humans to perceive the presence of surrounding objects and the environment (Kern, 2009).

Haptic displays enable the human operator to feel a virtual object as if the object is really existing and touchable through a haptic device. The success of haptic interface relies on a series of concepts such as passivity, transparency, impedance range and back-drivability of the haptic system. For instance, the operator's motion should not be restricted in free motion when there is no contact with virtual or remote object. Therefore, generally haptic devices are constructed with mechanisms with low inertia and less friction by avoiding transmission parts with high weight or ratio. Because of that, the maximum exertable forces of the impedance type haptic devices mostly depend on the actuator capacity used in haptic device. Likewise, the stability of the haptic system can be ensured by the passivity concept in terms of linear control theory. For instance, Adams and Hannaford (1999) proposed a virtual coupling network based on linear circuit theory to get sufficient conditions for stability in a haptic interface. In this approach, the human and the virtual environment considered as passive systems that guarantees the stability of the haptic simulation.

In this chapter, the concept of haptic technology with commercial products and applications are presented, and then the related terminology for control purposes are given. As a main subject of this thesis, the actuator types are reviewed. Later, the feature of MR-fluid and its devices are investigated. Finally, examples of haptic devices using MR-fluid brake that take part in literature are discussed in detail.

2.1. Overview of Haptics

Haptic interfaces aim to stimulate the human sense of touch through mechatronic devices which are called haptic devices with a computer based controller. In the haptic control loop of a haptic interface, the haptic device senses human operator motion or force as input for controller. Based on a virtual or tele-operated application, the response of the environment is computed by the controller. Consequently, the haptic device displays the computed information to the human operator by generating force or motion with actuator and/or transmission system. Due to human's sensitivity to high frequency sensory information and the stability of the haptic system, haptic control loop must repeat at high frequency level at 1 kHz (Hannaford & Okamura, 2008).

2.1.1. Haptic Applications

Haptic applications mainly include two sections as teleoperation and virtual reality simulation. Teleoperation means that the human operator can manipulate a slave robot remotely through a master device. For instance, the human operator can perform an operation in hazardous or inaccessible place such as nuclear disaster zone, space or underwater, at a safe distance. As a result of these advantages, haptic teleoperation is widely used in numerous fields like surgical robotics, assistive technology and space. For instance, the da Vinci surgical robot shown in Figure 2.1. (a) is a laparoscopic tele-manipulation system without a force feedback. Thanks to the camera at the laparoscope, the surgeon can monitor the operation during the surgery. The mechanism of the system translates the surgeon's hand movements into smaller, precise movements (Intuitive Surgical, 2016). However, the surgical operations require sense of touch. In addition to visual and auditory information, force feedback can increase the success of the teleoperation by creating the feeling of telepresence. Recently, a surgical robot named Sofie with a force feedback was developed at Eindhoven University of Technology (Bedem, 2010) as shown in Figure 2.1. (b).

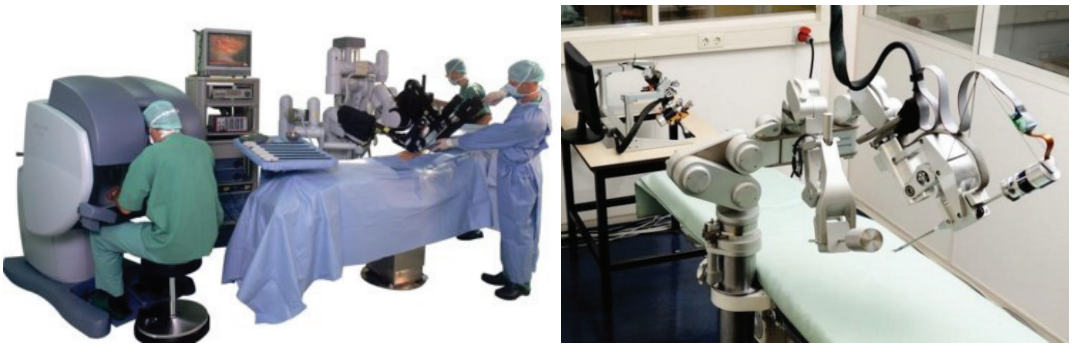

(a) (b)

Figure 2.1. (a) da Vinci surgical robot (Source: Intuitive Surgical, 2016), (b) Sofie surgical robot (Source: Bedem, 2010).

RedHawk MPR is a teleoperated mobile bomb disposal robot that comprises haptic feedback system developed for military deployments by Harris Robotic Systems. As seen in Figure 2.2., the system includes 6-DOF arm with force/torque sensor integrated inside the gripper that enables human operator to feel remote objects in contact (Harris Robotic Systems, 2016).

Figure 2.2. RedHawk MPR mobile robotic system with haptic control (Source: Harris Robotic Systems, 2016).

Haptic devices are mostly used for education, entertainment, and design purposes by creating virtual environment in where the user can perceive haptic feedback while interacting with virtual objects in simulation. An application named Virtual Design Works that uses haptic interface in design process of CAD models is developed by Liu and his team (2004). In this application user controls a haptic cursor to design a CAD model by pulling, pushing and dragging its surface in virtual space. Throughout the design process, force feedback helps the user to feel the surface of the virtual CAD model (X. Liu et al., 2004). In addition, today it is possible to find variety of haptic applications integrated into medical simulators for training purposes. In one of these research it was proven that haptics in minimally invasive surgical simulation are highly effective for training medical personnel (Basdogan et al., 2004).

2.1.2. Haptic Control Types and Commercial Haptic Devices

In impedance type control, motion is applied by the human operator to the system and in return, the haptic system generates a force feedback sent from the slave side in teleoperation or from the virtual reality system where the intersection forces are calculated. Especially for the mechanism of haptic device that is open-loop impedance type control, it is desired to have a low inertia and high stiffness. Hence, the weight and the friction of the mechanism should be minimized in order to provide free motion feeling to the user.

Figure 2.3. The Geomagic® Touch™ Haptic Device
(Source: Geomagic, 2016).

Open-loop impedance type control is widely used among the commercial haptic devices because of the simplicity of the mechanism design and the low cost of the required equipment for the haptic feedback control. One of the well-known devices in the market is the Geomagic® Touch™ haptic device from Geomagic (2016). As seen in Figure 2.3., it is an inexpensive haptic device with a stylus tip which senses position of user in six degrees of freedom (DOF) and the haptic device applies translational forces in 3-DOF to the user.

In 2007, Novint Falcon was released to the market by Novint Technologies. Figure 2.4. (a) shows that this inexpensive device has parallel mechanism with 3-DOF and it is aimed at entertainment sector. Moreover, a basic dynamic model is used in its hardware to compensate gravity and minimize the frictional effects of the haptic device (Novint Technologies, 2016).

(a) (b)

Figure 2.4. (a) Novint Falcon haptic device (Source: Novint Technologies, 2016), (b) omega.3 (Source: Force Dimension, 2016).

In close-loop impedance controlled system, applied force by the user is measured by the force sensor to compensate the disturbing forces such as friction and inertia of the dynamic system. The mechanism itself can be designed stiffer than open loop impedance control, however, the force sensor which makes these devices expensive is also technologically challenging. For instance, as shown in Figure 2.4. (b), the omega.3 from Force Dimension has a similar kinematic design with Novint Falcon, though comparatively it is much more expensive. Its mechanism is developed much stiffer thanks

to the close-loop impedance control. With a force sensor placed in gripper, Omega 3 fully compensates gravity and disturbance forces, and exhibits good accuracy performance (Force Dimension, 2016).

In admittance type control, contrary to impedance type control, the force applied by the user is sensed by the haptic device to lead the haptic device to the desired motion of the user. Admittance controlled haptic devices can be built much stiffer than impedance control devices while the friction and inertial effects are compensated in control. However, the control of such a device relies on force sensor which is quite expensive and complex to use. One of the example for admittance controlled haptic device is the HapticMaster (Figure 2.5.) which is remarkable for high force capacity up to 100 N with a large workspace. Contrary to its size, HapticMaster has high haptic resolution and exhibits dynamically impressive performance (Van der Linde, Lammertse, Frederiksen, & Ruiter, 2002)

Figure 2.5. HapticMaster (Source: Van der Linde et al., 2002).

2.1.3. Performance Criteria of Haptic Interface

The performance of haptic interface mainly depend on two criteria as transparency and Z-width. Designers of actuators for haptic devices must consider the performance criteria of haptic interface for stability and user comfort. Therefore, in this section,

performance criteria, both transparency and Z-width, are investigated from not only active but also passive haptic interface point of views.

The mechanical impedance Z is a dynamic relation between velocity and force. In short, high impedance refers to a stiff system while low impedance represents a light or soft system. The impedance of the entire system depends on the user impedance and the mechanical impedance that can be a simplified model of the user hand behavior while in contact with gripper and the impedance of the technical systems, respectively. The concept of impedance is highly important for the control and designing parts for the haptic system.

Transparency T was proposed as a tool for quantifying haptic interface performance and stability by Lawrence (1993). T is a frequency dependent factor between input impedance to the haptic interface Z_{in} and the output impedance Z_{out} received from the device (Kern, 2009).

$$T = \frac{Z_{in}}{Z_{out}} \tag{2.1}$$

In a haptic interface, it is desired to achieve transparency T=1 which means in the haptic interface the input impedance is not affected, namely that the user of the haptic system experiences the haptic output exactly the same as the desired haptic input.

Colgate and Brown proposed stability condition as impedance width, Z-width, which is a measure of the dynamic range of achievable virtual stiffness K and virtual damping B of the haptic display. In their paper (Colgate & Brown, 1994), performance criteria for building a haptic interface with wide range of mechanical impedance to satisfy the stability condition of the haptic interface are demonstrated. The stability condition in terms of passivity is defined relative to physical damping b and sampling time T in the following equation.

$$b > \frac{KT}{2} + B \tag{2.2}$$

It can be observed from (2.2) that the essential stability parameter is the physical damping which depends on the capacity of the haptic system and it cannot be exceeded. Therefore, it defines the limits of the virtual object stiffness that can be created.

They (Colgate & Brown, 1994) also assumed that the Z-width of the haptic interface can be enlarged by adding a damping constant b_c to physical damping b in (2.2). Then the following formula is derived.

$$b + b_c > \frac{KT}{2} + B \tag{2.3}$$

As a result of the additional damping constant b_c, the maximum virtual stiffness K and virtual damping B is increased. However, there is an inverse relation between Z-width and the transparency. Increase in overall physical damping $(b + b_c)$ affects transparency negatively, in other words, the user feels extra damping forces even in free motion.

Jinung et al. derived a new approach (Jinung & Dong-Soo, 2004) using (2.2) for MR-fluid actuator as a passive haptic interface by replacing physical damping constant with a controllable physical damping $b_c(H)$. Here, H represents the strength of magnetic field since the damping force of the MR-fluid based actuator relies on it.

$$b + b_c(H) > \frac{KT}{2} + B \tag{2.4}$$

In this case, the system can exhibit low damping in free motion and when it is required, the system can have high damping force than regular active haptic interfaces in order to simulate high stiffness in contact with the virtual object. As a result, the approach of Kwon and Song (2006) showed that MR-brake adaptation into the haptic system allows designer to achieve more stable haptic interface by enlarging Z-width and without worsening the transparency.

2.2. Actuator Types of Haptic Devices

Actuator selection plays a crucial role in designing a haptic device. For a haptic application, it is desired to have a transparent interface, high torque capacity and frictionless mechanism. Therefore, the developer must decide the actuator type considering the application. In this section, mostly used actuator types of haptic devices are investigated by categorizing them into two subjects regarding to the force feedback types as tactile and kinesthetic sensation.

2.2.1. Tactile Haptic Devices

A tactile haptic device is a machine that deals with the stimulation of the human tactile sensory receptors by generating a tactile feedback such as the texture, roughness, temperature and shape of the virtual object. Since the human tactile sensation is highly sensitive, the actuator of the tactile haptic device must operate at a high frequency level. The current technology of the tactile devices is inspired by matrix pin-printers and Braille systems for sight-disabled people. In this section, recently developed haptic devices which are actuated by electromagnetic, ultrasonic, piezoelectric, shape memory alloys and pneumatic based systems are investigated.

Hayward and Wang developed a tactile transducer device based on lateral skin deformation for Braille related applications (Qi & Hayward, 2006). The tactile device shown in Figure 2.6. (b) were actuated by 6×10 piezo ceramic actuators with a 250 Hz bandwidth. In their paper, it is claimed that the generated tangential force created very realistic tactile effect regarding pilot test results. This tactile sensation was demonstrated in an early work of Hayward as "hair-comb-effect" (Hayward & Cruz-Hernandez, 2000).

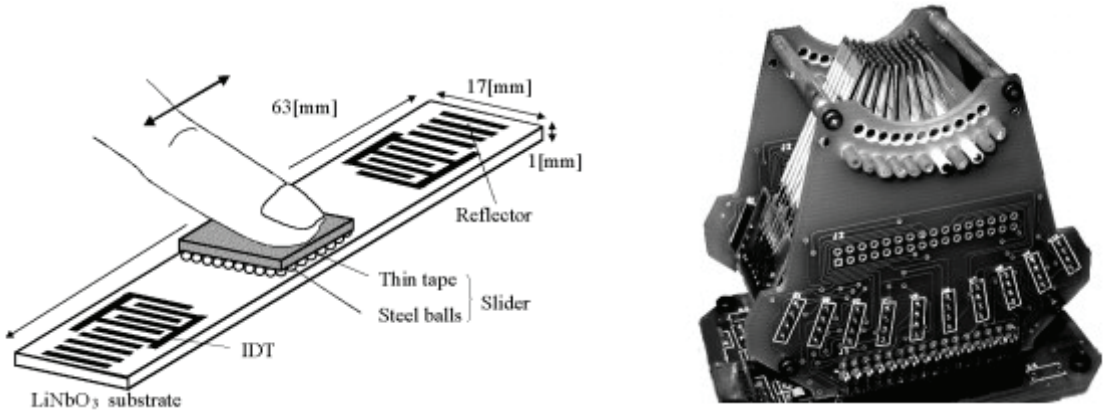

(a) (b)

Figure 2.6. (a) Tactile display based on SAW (Source: Nara et al., 2001), b) Tactile display device with Piezo-ceramic actuators (Source: Qi & Hayward, 2006).

To replicate a texture of a surface or sliding effect, surface acoustic wave (SAW), electrostatic actuator or rheological fluid technology were used by some researchers. Nara et al. developed a haptic tactile display for the generation of shear stress using SAW. Tactile display is generated by an alternating voltage with an inter-digital transducer in a Li-Nb-O_3 substrate as seen in Figure 2.6. (a). The wavelength of SAW is 265 μm with a driving frequency of 15 MHz. In their work, the roughness of the surface was controlled by changing the burst frequency of SAW from 20 to 200 Hz (Nara et al., 2001).

Yang et al. proposed a work of development of a pin-array tactile model for mobile devices in (Yang, Kim, Kim, Kwon, & Book, 2009). The developed tactile actuator consists of a solenoid, a permanent magnet and an elastic spring as shown in Figure 2.7 (a). The principle of the system relies on applying an electric current pulse on the solenoid, thus repulsive force between solenoid and permanent magnet is generated. It is emphasized that even though the developed actuator has small sizes and low power consumption, it can produce enough tactile feedback to stimulate receptors on human skin.

In one of the similar work, a tactile display system was developed focusing on temperature feedback. The device consists of Peltier elements and a ceramic disk. The temperature of the display surface was controlled by changing the electric current direction into the Peltier elements. The temperature range of the system was between -10 and 60 ℃ with a Peltier module driven by an 11 A current supply (Ino et al., 1993). Figure 2.7 (b) that can present both kinesthetic and tactile feedbacks, was developed by Kikuchi and Hamamoto. For force-feedback, artificial muscle which is a shape memory alloy fiber was used. The length of the SMA fiber can be controlled by electrical current. Additionally, they used magneto-rheological fluid in a button for tactile feedback. By controlling MR-fluid viscosity with magnetic field strength, the tactile button presents different level of hardness (Kikuchi & Hamamoto, 2008). Similarly, Taylor et al. proposed a 5x5 tactile array using electrorheological fluid for application in virtual environments. The tactile array creates adjustable resistance against the finger motion to create the illusion of the presence of a virtual object (Taylor, Hosseini-Sianaki, & Varley, 1996).

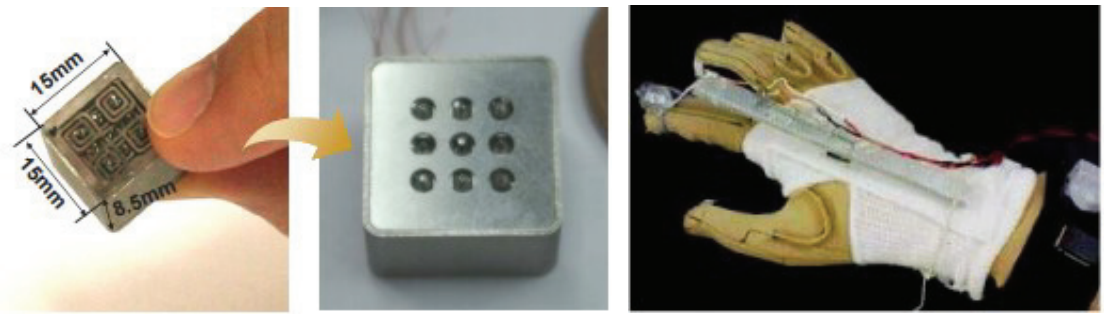

(a) (b)

Figure 2.7. (a) Pin-array tactile module (Source: Yang et al., 2009), (b) the HAMA haptic glove (Source: Kikuchi & Hamamoto, 2008).

Consequently, it is observed that electromagnetic actuation is the most common technology among the tactile systems. The SMA wire technology is also commonly used despite its low bandwidth and poor performance. For Braille type systems, piezoelectric based actuations are mostly preferred. Additionally, smart materials like ER and MR-fluids are applied into a few tactile display systems, however they are not yet sufficiently developed.

2.2.2. Kinesthetic Haptic Devices

DC motors are commonly used in kinesthetic type haptic devices as actuators because of their simplicity of use and low cost. Their operating logic grounds on the electrodynamics and electromagnetics principles. In other words, there is a direct proportional relation between output torque and input current value that allows the control with a direct current source within the haptic applications. Brushless DC motors also known as electronically commutated motors (EC motors) have low rotor inertia and are highly efficient that they show very impressive dynamic properties than brushed DC motors. Brushless DC motors require a more complex motor controller which makes them much expensive, nevertheless, they are the most frequently used type of actuator for haptic applications. It is possible to find EC motors in most of the haptic devices on the market and among the devices designed by researchers (Kern, 2009).

Even though the electrical motors are the most common type of actuators for haptic devices, they have some disadvantages that makes the system unstable. Considering the interaction between a human and the machine, especially human-size haptic devices can cause serious harm to humans when the system is unstable. However, the passive haptic interaction guarantees the stability due to its nature. There was a growing interest in integrating semi-active actuator into the haptic system to ensure the stability of the system in the last decade. A frictional brake would be a good choice as a semi-active actuator for haptic devices if it had linear properties and fast response time. But the properties of frictional brake fail to satisfy the requirements for a haptic application. Nevertheless, some alternative technologies such as Eddy current, ultrasonic, particle, electrorheological (ER) and magnetorheological (MR) brakes/clutches are applied to the haptic devices lately. In the following part, recently developed haptic devices using all kinds of actuators are introduced.

Magnetic particle brakes generate resistive torque to brake or slow the motion. There is a linear relation between the output torque of the particle brake and supply voltage that their torques can be controlled very accurately. Therefore, researchers have used them in haptic devices. In one of the related work, particle brake was coupled with 120 W brushless DC motor from Maxon motor to construct a hybrid haptic device using a five-bar linkage structure as seen in Figure 2.8. (a). In (Kwon & Song, 2006), it is pointed out that large steady-state error occurs due to the properties of the brake. The response time of the particle brake was 50 ms while the response time of the motor was 7 ms. Because of its relatively slow response time and nonlinear behavior compared to fluid based brakes, particle brakes are not commonly used in the haptic devices.

Unlike the friction brake, an eddy current brake uses the electromagnetic force generated by the effect of electromagnetic induction between a magnet and conductive object. Figure 2.8. (b) shows a prototype pantograph 2-DOF haptic device with Eddy current brakes that were built by the team of Gosline (2006). Their experimental results assert that the turn-on time of the brake is 2.6 ms and the dynamic damping frequency is 250 Hz. Moreover, eddy current brakes show linear properties as a tunable damper.

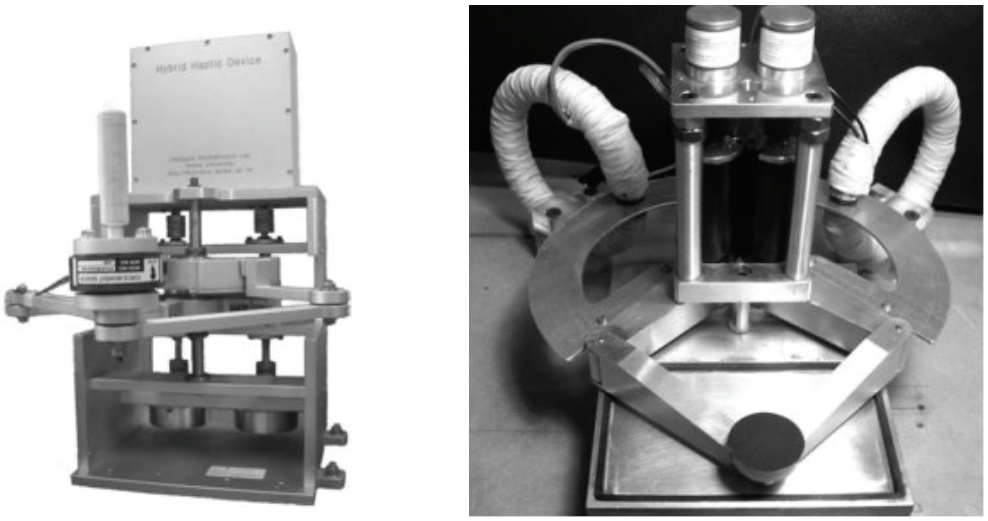

(a) (b)

Figure 2.8. (a) Hybrid haptic device with DC motor and particle brake (Source: Kwon & Song, 2006), (b) prototype haptic device with two eddy current dampers (Source: Gosline et al., 2006).

Ultrasonic actuator generates output force depending on the levitation phenomena which is related with the resonance of the piezoelectric material. Hence, they can perform at frequency within ultrasonic range (>15kHz). The output velocity of the ultrasonic actuator shows linear behavior. Because of its fast response time and non-magnetic characteristics, several researchers chose them as an actuator for haptic devices. For instance, Koyama and his colleagues (2003) developed a ultrasonic clutch with a piezoelectric vibrator material for multi-fingered exoskeleton haptic device. The ultrasonic clutch works with the ultrasonic levitation phenomenon. They claimed that the ultrasonic clutch can generate levitation force up to 20 N with a 45V input voltage and 20 kHz driving frequency.

In another work, Giraud and his team developed a 1-DOF haptic device using traveling wave ultrasonic motor (TUSM) USR30 from Shinsei. The ultrasonic motor USR30 torque capacity is 0.1 Nm and the outer diameter of the motor is 30 mm and the thickness is 5 mm. The operation voltage frequency of motor is about 50 kHz which allowed the researcher to set sampling period as 0.1 ms. In their experimental results, it is reported that the torque is not controlled and the users felt some oscillations during penetration through the virtual wall. Additionally, it is emphasized that when the user

reverses the motion, some problems occurred that effects the feeling of the force-feedback (Giraud, Amberg, & Lemaire-Semail, 2010).

Similarly, Flueckiger developed a 1-DOF prototype haptic device (Figure 2.9.) which is compatible with Magnetic Resonance Imaging (MRI) for neuroscience studies using USR60 traveling wave ultrasonic motor from Shinsei. Motor selection for an MRI compatible system is vital since the regular electromagnetic motors may affect the scanner's magnetic field namely imaging process and also it can be harmful to the environment. However, TUSM presents weak electromagnetic disturbances assuming the use in high magnetic field environment. Since TUSM are friction drives, they are non-back-drivable. Therefore, it was required to use admittance control. In their paper, it is commented that the TUSM initially presented highly nonlinear behavior, hence the tailor-made control algorithm was adapted to optimize the operating characteristics (Flueckiger, Bullo, Chapuis, Gassert, & Perriard, 2005).

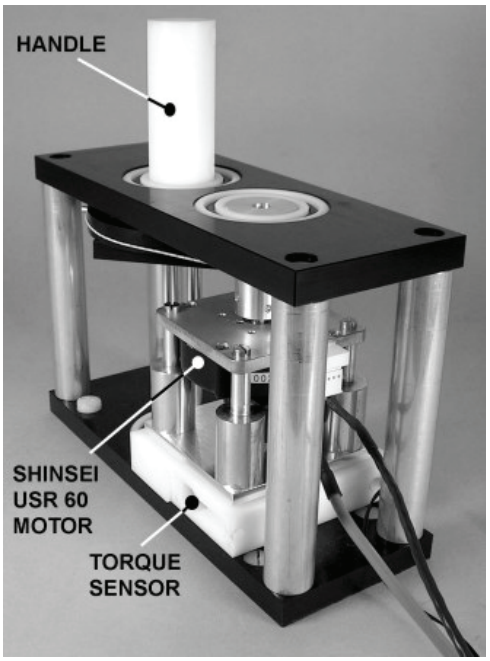

Figure 2.9. Prototype of the MRI compatible 1-DOF haptic device
(Source: Flueckiger et al., 2005).

However, the ultrasonic motors have some limitations due to their non-linear velocity dead-band about zero velocity and time delays. Therefore, it can be challenging to control them in haptic applications. Recently, Parthiban presented a parallel actuation

approach using two ultrasonic motors with a differential mechanism to overcome the limitations of ultrasonic motors (Parthiban, Esser, & Zinn, 2012). The conceptional design of their system is presented in Figure 2.10..

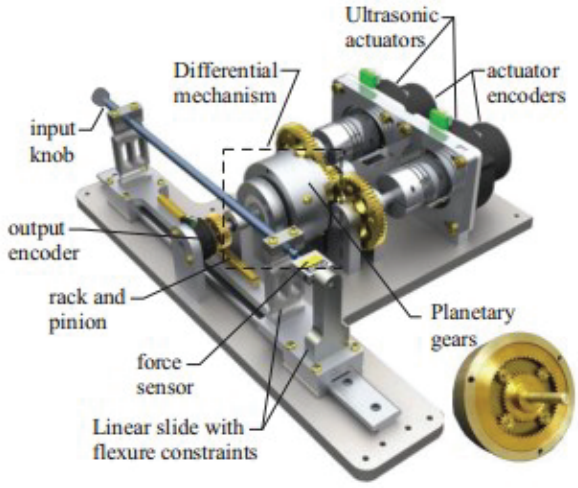

Figure 2.10. The design of parallel actuation haptic knob.

To fulfill the requirements of haptic devices such as high stability and force capacity within a limited space, researchers focus on the hybrid actuation systems, mostly combining motor and brake. For instance, Chapuis designed a hybrid ultrasonic motor (Figure 2.11. a) using USR30 (Shinsei Corporation Inc.) with an electrorheological brake system for haptic applications (Chapuis, Gassert, Burdet, & Bleuler, 2006). The ER brake is controlled with a 2 kV supply voltage for two different operation modes as brake and slips so that the system can be controlled by both impedance and admittance type of control. In another work of Chapuis, he developed a novel hybrid actuator which consists of an ultrasonic motor and a powder brake for haptic applications (Chapuis et al., 2007). The hybrid actuator was used in a haptic knob as shown in Figure 2.11. (b). The USR30 (Shinsei Corporation Inc.) ultrasonic motor with rated torque of 0.1 Nm and the S90MPA (Sterling Instrument) powder brake with a rated torque of 32 mNm were chosen as actuators for hybrid system. In their work, it is observed that the ultrasonic motor driver caused time delay at the initial and the reverse motion of the motor.

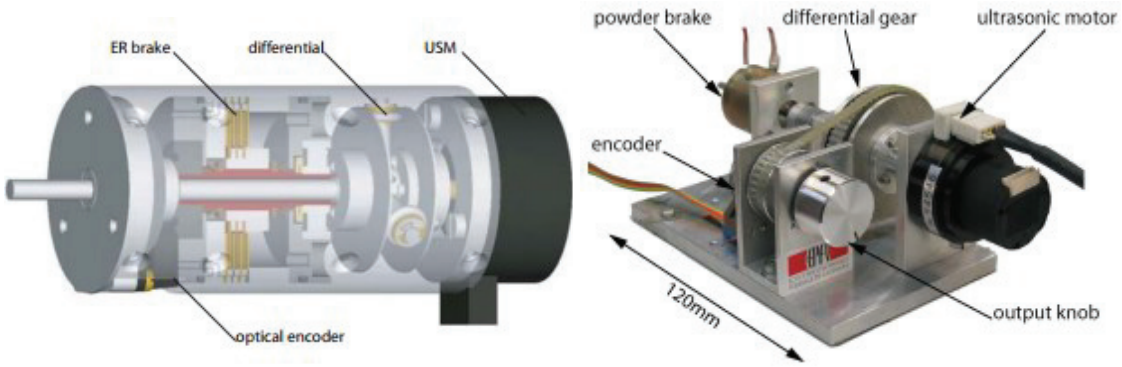

(a) (b)

Figure 2.11. (a) The design of hybrid ultrasonic/ER brake actuator (Source: Chapuis et al., 2006), (b) the prototype of haptic knob actuated by hybrid actuator (Source: Chapuis et al., 2007).

Most actuators used in haptic devices have a direct relation between electric input and torque output. On the contrary, in pneumatic actuation principle, air pressure and volume-flow are transformed into displacement and force. Generally, pressure is generated via electrical compressor or with an actuator attached to the compressor. There are some examples of haptic devices in which pneumatic actuators are used. For instance, the Rutgers Master II is a haptic glove which can provide force-feedback for each fingertip up to 16 N. As seen in Figure 2.12., it uses custom pneumatic actuators rather than DC motor as in commercial haptic glove CyberGrasp. In (Bouzit, Burdea, Popescu, & Boian, 2002), the developers of the Rutgers Master II compared their product with the CyberGrasp. It is demonstrated that the weight of the haptic glove could be reduced by using pneumatic actuator instead of DC motors with the transmission parts which increase the overall weight of the haptic glove. For such a wearable device, the overall weight is critical in order to reduce the fatigue effects on the user. However, it is also known that pneumatic actuators have some difficulties in control since there is not a direct relation with the torque and electric current and as a result the system requires additional sensor.

Figure 2.12. The Rutgers Master II
(Source: Bouzit et al., 2002).

Smart materials like MR and ER fluids change their viscosity within milliseconds according to the applied magnetic or electric field respectively. Recently, using electro or magneto rheological fluid in clutch or brake mechanism, researchers aimed to develop a haptic device with improved transparency and dynamic range. For instance, Furusho and Sakaguchi (1999) developed a force display device using ER actuators with low inertia. Consisting of an ER clutch and electrical motor as seen in Figure 2.13., the developed ER actuator has low-inertia properties and fast response time than regular powder clutches. Their force display device can produce force more than 25 N with a 3 kV/mm electric field intensity.

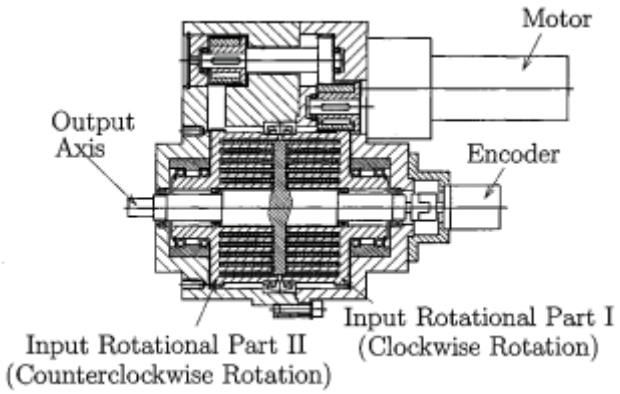

Figure 2.13. Sectional view of ER actuator
(Source: Furusho & Sakaguchi, 1999).

Bar-Cohen et al. (2001) developed an ER fluid based haptic glove system called MEMICA for robotic tele-surgery simulations. MEMICA includes electrically controlled force and stiffness (ECFS) actuator that works as a suspension brake system controlled by electric field and the ECFS actuator can produce force up to 15 N regardless of its small size. In another work, Melli-Huber and his team developed ER fluid based semi-active actuators for 2-DOF haptic joystick system to be used in human-vehicle interface. Their ER fluid actuator can create resistive dynamic and static force up to 0.628 N m and 1.367 Nm with a 4 kV electric voltage (Melli-Huber et al., 2003). Later on, Han et al. (2007) developed a spherical haptic device by using ER fluid with the aim of minimally invasive surgery. As shown in Figure 2.14., the spherical haptic device consists of a clutch and brake mechanism within the spherical ER joint and AC motor. Thanks to its hybrid actuation system, developed ER haptic system can perform active and passive force reflection with a 0.09 N maximum force error due to hysteresis and mechanical friction. Their haptic system can generate 1.08 N active force at 2 kV/mm electric field intensity.

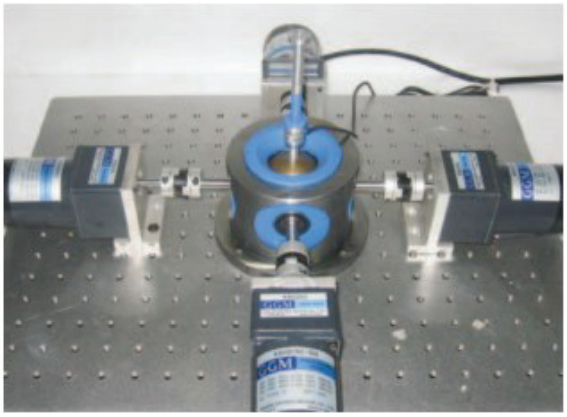

Figure 2.14. The spherical ER haptic system
(Source: Han et al., 2007).

In this section, most common types of active and semi-active actuators are examined except MR-fluid based ones. When the safety and stability are considered, the rheological fluid based clutches or brakes can be a good solution for a semi-active actuator. Their response times are much fast (up to five milliseconds) than other clutches, and this rapid response makes them unique equipment for the passive and hybrid actuation system for haptic applications. After a comprehensive research, it is seen that MR-fluids

are comparatively better than ER fluids for haptic applications. ER fluid requires high voltage to control the rheological properties of the fluid while MR-fluid reacts with a magnetic field which can be created with low voltage and current (up to 2 A). Considering the human safety, when ER technology is used high, voltages may be harmful when a human interacts closely with the haptic device especially for wearable haptic devices as a haptic glove. The range of shear stress (with or without magnetic field) of MR-fluid is almost ten times larger than ER fluid. Therefore, higher torque/force ratio can be achieved with the same size devices besides, haptic devices using MR actuator can present better free space without the effects of reflection force and viscosity. As a result, MR-fluid is chosen for the semi-active actuator design as a scope of this theses.

2.3. Overview of MR-Fluid and Related Devices

In this section, features of MR-fluid, namely its rheological properties, mechanical model and basic operational modes as well as related applications that available on the market are presented. In addition, haptic devices that use MR-fluid brake or clutch as a passive or hybrid actuator are discussed.

2.3.1. Properties of MR-Fluid

Magnetorheological fluid is a smart material that changes its viscous (rheological) characteristic with an applied magnetic field. The change in yield stress of MR-fluid is linearly linked to the applied field density. Main features of the commercial MR-fluids from LORD Company are given in Table 2.1. The properties of MR-fluid allow to create mechanical systems that provide quiet and rapid-response interface with an electronic control. Therefore, MR-fluid is applied to many commercial products (Jolly, Bender, & Carlson, 1998).

Table 2.1. Typical properties of commercial MR-fluids (Source: LORD Corp., 2016).

Property	**Typical value**
Viscosity, $Pa.s$ @40 ℃	0.040 to 0.350
Density, g/cm^3	2.28 to 3.54
Solids content by weight, %	72 to 86
Magnetic field strength, $kAmp/m$	up to 300
Yield stress, kPa	up to 60
Reaction time, ms	< 5
Operating voltage and current, $V; Amp$	2 to 24; 0 to 2
Operating temperature, ℃	-40 to 130

The first MR-fluid clutch was invented by Jacob Rabinow at US National Bureau of Standards (Rabinow, 1948). In his paper, besides an experimental result, the features of the MR-fluid were presented. His experimental result claimed that MR-fluid clutch showed smooth performance in action and it was easy to control such a device with a low electric power. After a silent period, the research interest arose with the commercial success of MR-fluid based applications in the 1990s. Currently, variety of applications that use the MR-fluid device can be found. MR-fluid dampers are applied to suspension system of vehicles to increase the driving performance and the comfort of the driver. For instance, General Motors introduced the MagneRide suspension system that include an MR-fluid damper and an on-board Electronic Control Unit (ECU) within the Cadillac Seville STS automobile, in 2002 (Bwigroup, 2016). Since then MR-fluid dampers have become more available on quite a few General Motors vehicles as well as Ferrari Fiorano and Audi TT Coupe (Carlson, 2006). In addition, recently, many researchers adopted MR-fluid brake to the haptic devices as a semi-active actuator because of the unique characteristics (e.g. Reed & Book, 2004; Li et al., 2006; Senkal & Gurocak, 2009; An & Kwon, 2008; Sung et al., 2014).

The magnetorheological fluid consists of the micro-size iron particles (1 to 20 microns) which are contained in the oil or water based carrier fluid (LORD Corp., 2016). When the magnetic field is applied, the iron particles align with the magnetic flux direction and create chain-like structures that restrict the motion of the fluid, thereby increasing the viscous characteristics. Consequently, the yield stress of the fluid is dependent on the chain-like structures that occur as the magnetic field increases. The fluid exhibits Newtonian-like behavior without an applied magnetic field. Hence, the Bingham plastic model that has the magnetic field depended yield strength variable is often used to represent the behavior of the rheological fluids (WH Li, Liu, Kosasih, & Zhang, 2007). In this model, for the shear rate $\dot{\gamma}$, the shear stress τ , is given by

$$\tau = \tau_y(H) + \eta\dot{\gamma} \tag{2.5}$$

where τ_y is the yield stress induced by the magnetic field stress, H and η is the viscosity of the fluid. In another work based on Bouc-Wen method, hysteresis behavior is also considered to predict successfully the mechanical behavior of magnetorheological fluid (Spencer, Dyke, Sain, & Carlson, 1997).

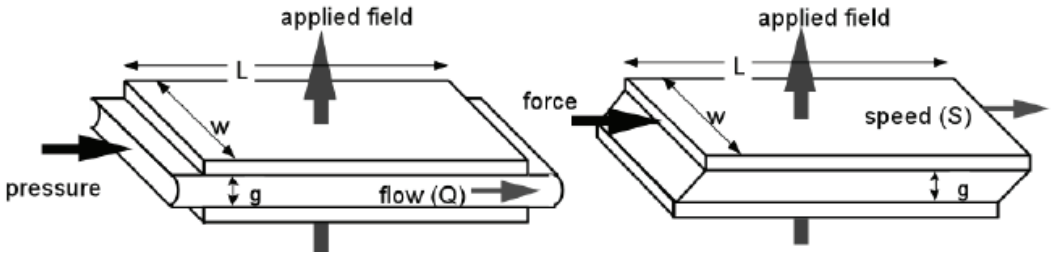

Figure 2.15. Basic operational modes of MR-fluid: (a) pressure driven fluid mode, and (b) direct shear mode (Source: Carlson, Chrzan, & James, 1994).

MR-fluid devices has two operational modes as a pressure driven fluid mode and a direct shear mode as shown in Figure 2.15.. Servo-valves, dampers and shock absorbers employ the pressure driven mode while clutches, brakes use the direct shear mode (Jolly et al., 1998).

2.3.2. Magneto-Rheological Semi-Active Actuators

The properties of MR-fluid allow to accurately control clutch by means of intensity of magnetic field by applying electric current. The most common MR-fluid clutch is the rotary one that basically consists of input components (inner disk/disks attached to the inner shaft) and output components (outer case attached to the outer shaft). The gap between the disk and the case is filled by MR-fluid and electromagnetic coils are wounded around the case in order to generate a magnetic field which is applied in vertical direction with respect to the direction of motion. When magnetic field is applied to the MR-fluid, the rheological characteristic of the fluid alters rapidly. In other words, the viscosity of the fluid increases concurrently with the magnetic field strength, which allows the MR clutch transmitting the input forces towards the output shaft. Rotary type MR-brake configurations are shown in Figure 2.16..

The rotary disk type of MR-fluid clutch is the most common configuration, that it is used in a variety of devices which can be found as a commercial product on the market as well as research projects in the literature. However, the selection of MR-fluid clutch configuration is highly important for the purpose of the usage. Wenjun Li (2014) compared three different MR clutch configurations which are drum, single-disk and multi-disk clutches, and his result declared that the multi-disk configuration exhibits the best characteristics regarding to compactness, weight/torque ratio and moment of inertia.

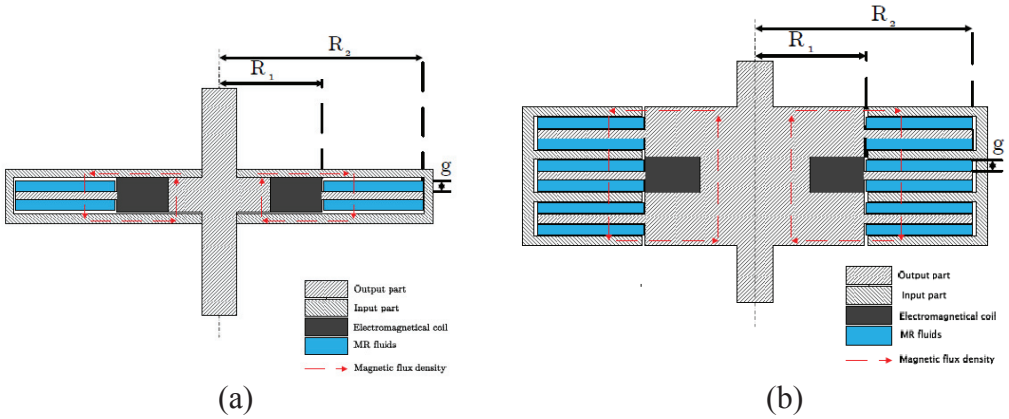

Figure 2.16. Cross section view of a (a) single-disk MR clutch, (b) multi-disk MR clutch (Source: Wenjun Li, 2014).

Regular MR clutches can generate resistive torque/force in one direction, against the motion. However, bi-directional MR clutches include two rotors that can rotate separately. Contrary to regular rotary clutches, bi-directional clutches include two input shafts joined to the separate rotors that are controlled by two different coil systems. To separate two magnetic fields from each other, a non-magnetic material is placed between the casing parts (Nguyen & Choi, 2011). The configuration of the bi-directional MR clutch is shown in Figure 2.17..

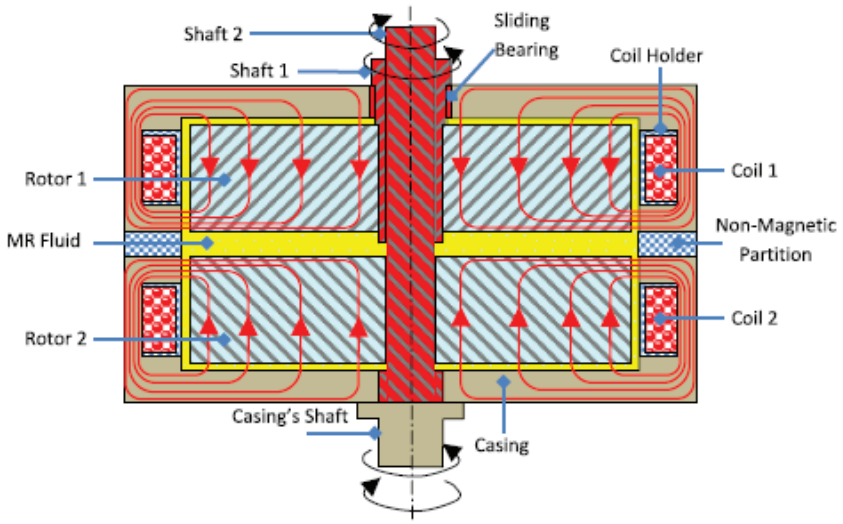

Figure 2.17. Cross section view of the bi-directional MR clutch
(Source: Nguyen & Choi, 2011).

2.4. Recently Developed Haptic Devices Using MR-Brake or Clutch

The semi-active actuator as MR-fluid brake can only dissipate the energy from the system in the opposite direction of the user motion. In general, MR-fluid brakes are integrated into haptic devices to obtain a passive haptic interaction. MR-brakes coupled to electric motors can also be used to develop a hybrid actuation systems. Additionally, when MR clutches are combined with electric motors, haptic system can generate active interaction while ensuring the user safety. In this section, passive and hybrid actuation type haptic devices that use MR-fluid brake or clutch are discussed.

2.4.1. Semi-Active Haptic Interface

User safety and the system stability are highly desirable for haptic devices, especially for the human-size devices that use powerful motors. Semi-active actuators dissipate the energy from the system by absorbing the active forces/torques. Therefore, the only active energy in the system comes from the user in passive haptic interaction. That feature guarantees the stability of the interaction as well as the safety of the user. In the following, recently developed haptic devices with passive actuation are examined.

Reed and Book (2004) developed a new passive haptic device with MR-fluid brakes and it was used in path following application. In this work, a modeling procedure that characterizes the behavior of MR-fluids was introduced. In their paper, a solution for the limitation of passive system was proposed. They suggested that more semi-active actuators than the degree of freedom can be used to reduce the region of unachievable force directions. In two different configurations, three and four commercial MR-fluid brakes from LORD were used for 2-DOF planar five bar linkage. Their results claim that the new passive haptic display system reduces the path following error, but there were not performance advantages between three and four-brake configurations.

In another work, a 2-DOF passive haptic joystick was developed for virtual reality applications by WH Li et al. (2007). As seen in Figure 2.18., the MR joystick consists of a gimbal structure which was constructed using two passive disc-shaped MR actuators. Each of the MR actuators includes a 78 mm diameter disc and the MR joystick provides resistance force or torque up to 10 Nm. They proposed a sub-hysteresis model as a control method for MR actuator which suffers from hysteresis behavior. The hysteresis behavior occurs when the magnetization remains in ferromagnetic elements after removing magnetic field. Additionally, Li and his colleagues mentioned that MR actuator facilitates the creation of different material feeling which has different hardness scale such as the tissue and the bones at the virtual finger. Therefore, MR actuators can be used in a virtual surgery interface, in which the user could experience the different force exertion regarding the hardness of the virtual object of the human body.

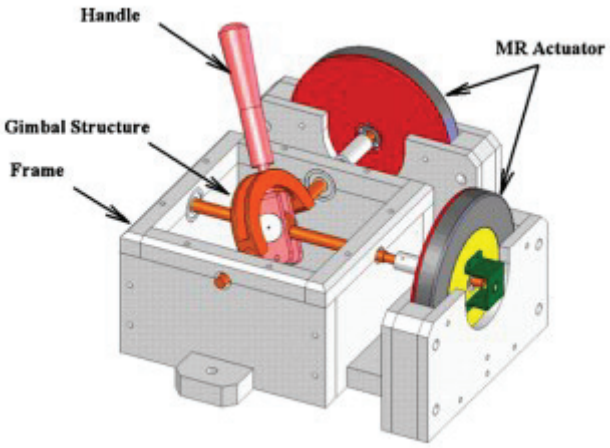

Figure 2.18. MR-fluid based 2-DoF haptic joystick system
(Source: WH Li et al., 2007).

Contrary to the regular disc type MR-brakes, Senkal and Gurocak (2009) developed the first multi-DOF spherical MR-brake. The spherical MR-brake is used in force feedback joystick for haptic applications as shown in Figure 2.19.. When the spherical MR-brake is activated, it can restrict or lock all three rotational degrees of freedom simultaneously. The joystick handle is equipped with force sensor to measure the forces applied by the user. The force feedback is used to control the behavior of the haptic device without encountering stick wall situation. They evaluated the applicability of spherical MR-brake in haptic field with a couple of virtual reality applications. In these virtual reality applications, the user shifts the manual gear as in automobile and contacts with virtual wall using haptic joystick.

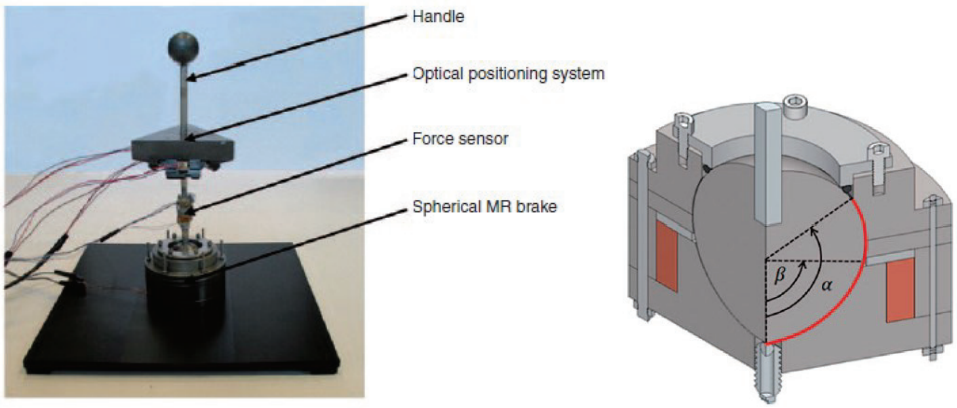

(a) (b)

Figure 2.19. (a) Force feedback joystick, (b) Cross sectional view of Spherical MR break (Source: Senkal & Gurocal, 2009).

2.4.2. Hybrid Haptic Interface

Hybrid actuator consists of an active and a semi-active actuator. It is considered that the hybrid actuated system overcomes the limitations of passive actuated haptic devices. Commonly MR-fluid brake is coupled with DC motor to create hybrid actuation system for the haptic device. In the following, developed haptic devices that have hybrid actuation system including MR-brake are discussed.

Yamaguchi and his team (2005) introduced a hybrid MR actuator consisting of two MR clutches and a DC motor. Using five bar linkage mechanism, they developed a 2-DOF force display system that can generate force up to 190 N.

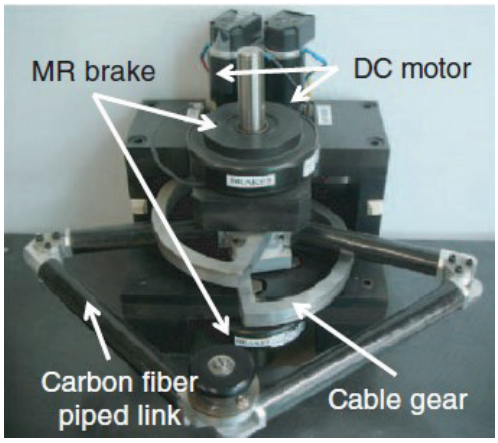

Figure 2.20. The five-bar linkage haptic device with DC motors and MR-brakes (Source: An & Kwon, 2008).

Similarly, a hybrid five-bar linkage haptic device was developed by An and Kwon (2008). As seen in Figure 2.20., the actuation system of haptic device consists of DC motors and MR breaks. In their article, the quasi-quantitative Z-width method is used as a performance tool for the assessment of hybrid actuated system. In the test results, they demonstrated that Z-width can be enlarged by using hybrid system coupled with MR-brake and DC motor. In other words, the achievable virtual stiffness of the haptic interface was increased by adapting MR break. They performed comparative tests by activating only DC motors, only MR-brakes, and both of them in a virtual reality application. Their

results declare that hybrid haptic device provides more realistic and transparent haptic interface with higher stability than the others.

The haptic joystick that consists of spherical MR-brake (Senkal & Gurocak, 2009) was advanced by adding air muscles to the actuation system by Senkal and Gurocak (2011). Developed hybrid actuator system includes a spherical MR-brake and three air muscles (Figure 2.21.). Achievable total force of the hybrid haptic joystick at the tip point is up to 16 N. According to their work, the device has 170 ms time constant due to MR-brake. They demonstrated that, a hybrid device can create frictionless virtual wall surface, what is considered by another researcher as impossible to achieve with a passive haptic device.

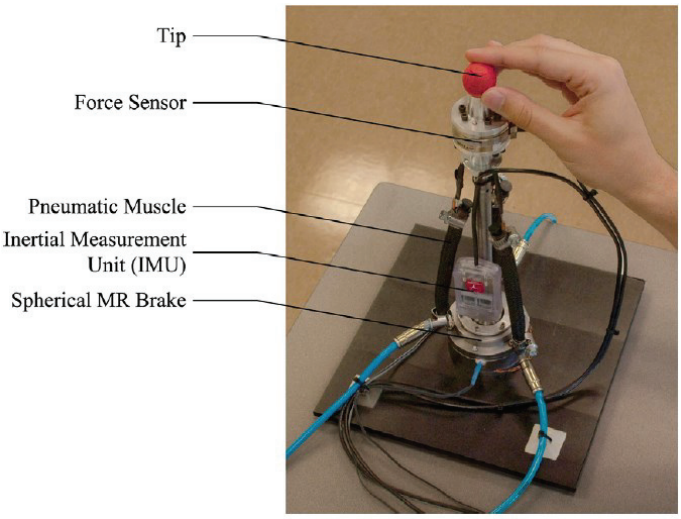

Figure 2.21. Prototype of hybrid haptic joystick
(Source: Senkal & Gurocak, 2011).

Song, Oh, and Choi (2014) presented a new type of 4-DOF haptic master using bi-directional MR-fluid clutches that is developed for a robot-assisted minimally invasive surgery system. The actuation and transmission system of the proposed haptic master device includes DC motor, planetary gear system and bi-directional MR-fluid clutches that can generate active torque around 2.7 Nm along 4-DOF directions as shown in Figure 2.22. (a). The schematic configuration of bi-directional MR-fluid clutch is shown in Figure 2.22. (b). In the design process, ANSYS was used to find optimal dimensions for the MR-fluid clutch design.

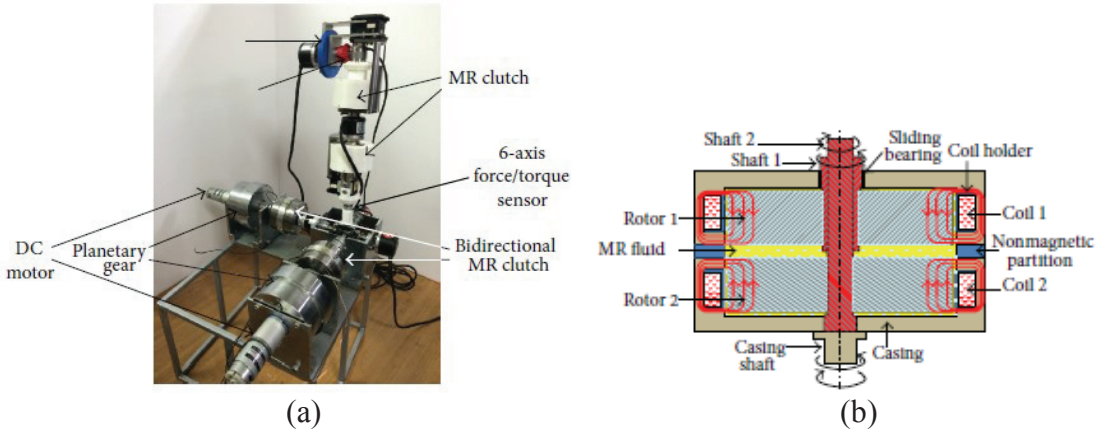

Figure 2.22. (a) MR-fluid based 4-DOF haptic master, (b) Schematic view of bi-directional MR clutch (Source: Song et al., 2014).

Similarly, a hybrid actuation system consisting two uni-directional MR-brakes and a DC motor was designed and developed for haptic devices by Rossa et al. (2014). The proposed hybrid design was highly effective for solving sticky wall effect which occurs while using semi-active actuators in the system. The hybrid actuator had a torque range between 0.03 to 5.5 Nm with $17.75\ \mathrm{kNm^{-2}}$ torque density. The cross-sectional view of the CAD model of hybrid actuator is shown in Figure 2.23..

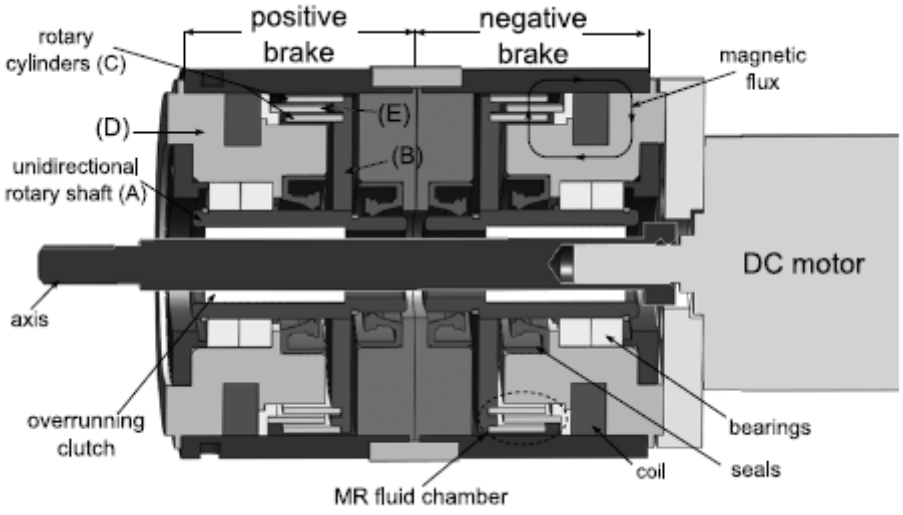

Figure 2.23. Cross sectional view of the hybrid actuator (Source: Rossa et al., 2014).

2.5. Conclusion

In this chapter, different types of MR-fluid brake designs and examples of integration into haptic devices are investigated. The common problems according to semi-active actuation systems are determined. For instance, the joystick type haptic device successfully created the realistic contact feeling with the virtual surfaces (WH Li et al., 2007). However, it caused difficulties when the user moves inside the virtual wall or slides on the virtual wall surface. This problem can be explained by the hysteresis behavior of the ferromagnetic elements used in MR break design. Moreover, An and Kwon (2008) emphasize that the participants of tests mention "stuck in the wall" feeling while using only MR actuators. This experience was formerly called as 'sticky wall' in the literature (Rosenberg & Adelstein, 1993), which is another common problem for the passive haptic devices. This situation occurs after the initial contact with the virtual wall that makes the motion hard for the user inside the wall. When the user once penetrates the virtual wall, the MR actuators become activated which restricts motion of the user in all directions.

Hysteresis effects can be lessened by considering the material selection or applying the control methods. For instance, Spencer et al. (1997) introduced a new method based on Bouc-Wen hysteresis model which was successful in predicting the mechanical behavior of magnetorheological fluid considering the hysteresis behavior as well. Additionally, WH Li et al. (2007) proposed sub-hysteresis model for the haptic interface which suffers from hysteresis effects.

As a solution to the 'sticky wall', the developer of the haptic device using MR-fluid brake may consider adapting a force sensor in addition to DC motor (Kwon and Song, 2006; An and Kwon, 2008). However, the force sensor is considerably expensive equipment and complex to use. Also, in the work of (Rossa et al., 2014), two uni-directional MR-brakes were coupled with an DC motor in order to eliminate sticking effect. To the best of our knowledge, only one reported study proposed as a solution for sticky wall problem without using additional equipment besides MR-brakes. In this work, two MR-fluid brakes for each degrees of freedom, working opposite direction to each other, were used for the passive 1-DOF haptic paddle device. When one of the brakes was activated, the motion would be restricted in the direction of the motion of the user.

Nevertheless, the user would be free to move opposite direction thanks to the mechanical configuration (Karabulut et al., 2015).

After investigating the possible designs for the passive haptic interaction in literature, it is considered that the best choose as a passive actuation system for haptic device would be to use two MR-fluid brake for each degree of freedom of the system with a Bouc-Wen model based hysteresis control. Even though the proposed actuation system is passive, it can overcome both sticking and hysteresis problems as well as achieving the high resistive torque in a limited space. Additionally, the proposed actuator can fulfill the requirements to achieve advanced haptic interface with high transparency and low inertia. With this system, it is also possible that ensuring the safety of the user, high force feedback with a short response time (in a few milliseconds) can be developed.

CHAPTER 3

METHODOLOGY

The work of this thesis consist of two main part as design and development of an MR brake and experimental validation. Therefore, the methodology related to this study is presented in two section. In the MR brake design methodology, several types of MR brake design are investigated and design parameters of MR brake are introduced. The method, which is used for the design optimization, including FEA simulation and analytical formulae is also described. In the experimental methodology, the equipment used for experimental work and test setup are explained.

3.1. MR-Brake Design Methodology

The performance of the MR-brake relies on some design criteria such as the placement of the coil, the disc shape and the material selection. Those selections directly affect the magnetic field strength applied on the MR-fluid in the device. In order to achieve a high quality device within a limited envelope, it is important to understand the effects of the selection in terms of the magneto-static analysis. Therefore, in this chapter all design criteria are comparatively investigated with FEA simulation support besides analytical approach and the results are validated with the experimental study.

3.1.1. Magnetic Field

Magnetic fields can be generated by applying electric current through a wire. The magnetic field occurs around the wire and the direction of magnetic field lines are defined by the right-hand rule. The strength of the magnetic field *H* designates the density of the magnetic field lines and the quantity of the magnetic field is calculated by the law of Lorentz force. The quantity of the magnetic field lines in the perpendicular area defines

the magnetic flux. The magnetic flux of a current carrying wire can be calculated with the given formula below.

$$B = \frac{\mu_0 I}{2\pi r} \tag{3.1}$$

The magnetic flux density B is directly proportional to the permeability μ_0 of the surrounding space and the current I in amperes of the current carrying wire and inversely proportional to the radial distance r to the wire.

In order to get a uniform magnetic field similar to the solid magnets, solenoids are used for practical applications. The magnetic field strength of a solenoid can be controlled by the level of electrical current. In short, a solenoid is a coil of wire that can create a uniform magnetic field at the center as shown in Figure 3.1.. Magnetic field can be even strengthened with the use of ferromagnetic material such as iron at the core. However, magnetic field around the solenoid is divergent and weak.

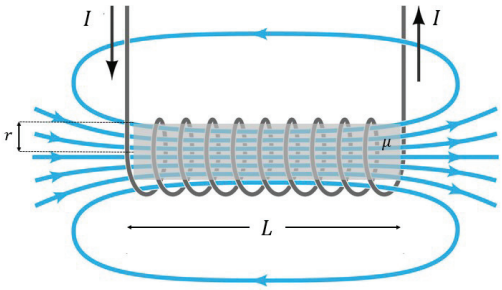

Figure 3.1. Magnetic field lines of the solenoid.

The magnetic field B inside the solenoid is uniform and proportional to the applied electric current I and the number of turns N per unit length L. Magnetic field strength is also proportional to the permeability μ of the core. For instance, relative permeability of iron is around 200,000 while the relative permeability of air is 1. Therefore, the material selection effects the magnetic field directly as much as the applied electric current and the turn density of the enameled wire.

$$B = \frac{\mu N I}{L} \tag{3.2}$$

3.1.2. Material Selection

The performance of an MR-brake relies on MR-fluid behavior under the magnetic field effect. In order to generate torque, MR-brake device benefits from the rheological properties of MR-fluid. The MR-fluid is situated between moving parts as a thin layer. When magnetic field is orthogonal to the MR-fluid layer, the iron particles align with the magnetic field lines. Inside the carrier fluid, those column type structure increase the yield stress of the material. Therefore, it is important how MR-fluid is exposed to the magnetic field. Otherwise, MR-fluid will not give a good response to the magnetic field even if the strength is high. Because of that, the magnetic flux path must be controlled in the process of structural design of brake and material selection.

Material selection for all parts in the MR-brake are modeled in the Finite Element Analysis (FEA) simulation in order to see the effects of the magnetic flux. If the material shows a non-linear characteristic in magnetic property, a B-H curve which is defined, describes the relationship between magnetic flux density B and magnetic field strength H. In the previous chapter, the properties of an MR-fluid available in the market are shown in a table. In order to have an MR-brake with a minimal friction force at zero electric current, the MRF-122EG, which has the lowest viscosity, is chosen. Figure 3.2. shows the magnetic properties of MRF-122EG.

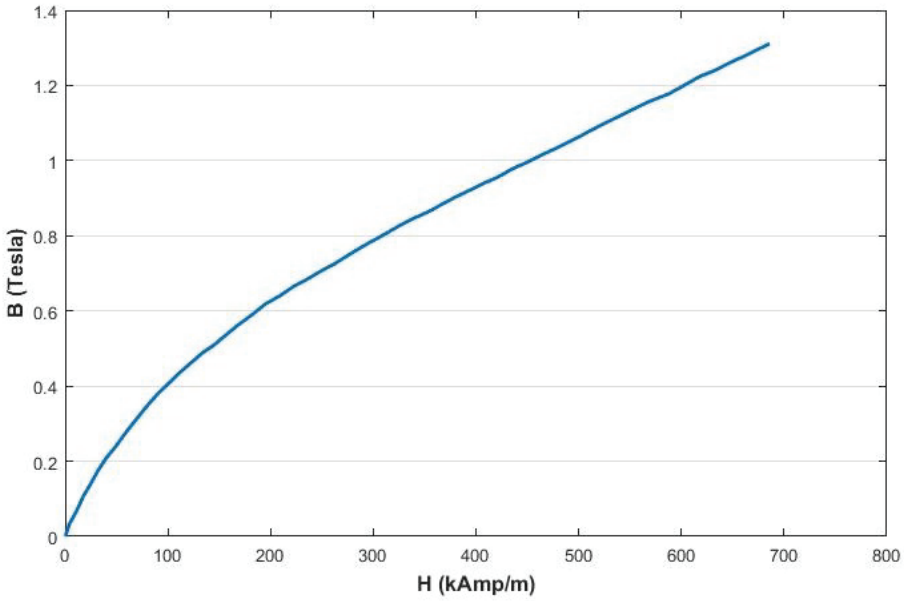

Figure 3.2. Magnetic properties (B-H curve) of MRF-122EG.

Using magnetic properties shown in Figure 3.2. and Figure 3.3., the yield stress of MR-fluid (MRF-122EG) in relation to magnetic field can be obtained. As it can be noticed in Figure 3.3., the yield stress curve exhibits linear relation to the magnetic field up to 24 kPa which is around 0.46 T. That means, solidification of MR-fluid can be controlled linearly with electrical current up to that point. During the development of the MR-brake design, magnetic flux density on the MR-fluid at the max current rate can be targeted to be 0.46 T. Nevertheless, the curve of yield stress approaches to 35 kPa which is the upper limit for the MRF-122EG.

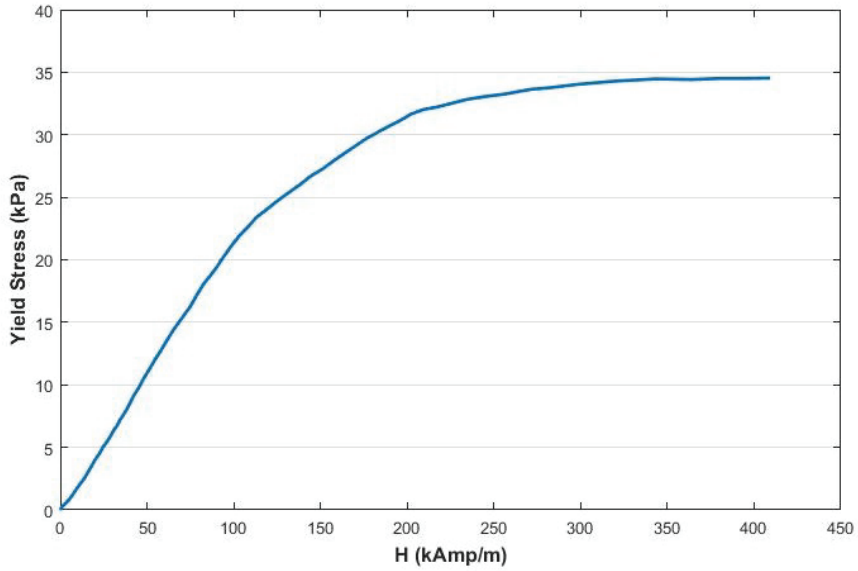

Figure 3.3. Yield stress vs. magnetic field strength of MRF-122EG.

For other materials that have linear magnetic property, the permeability defines the magnetic characteristic of the material. For instance, ferromagnetic materials such as iron has high relative permeability constant that enhance the magnetic field strength. In order to define a path for magnetic field lines, all the parts must be chosen among the ferromagnetic materials. Additionally, the parts that block magnetic flux must be chosen among non-ferromagnetic materials such as aluminum or plastic. The relative permeabilities of common materials are shown in Table 3.1.

Table 3.1. Relative permeability of materials.

Material	**Relative permeability (μ/μ_0)**
Metglas	1,000,000
Iron	200,000
Structural steel	10,000
Aluminum	1
Air	1
Copper	0.999

3.1.3. Types of MR-Brakes

Magneto-rheological fluid is the smart material which can exhibit different rheological characteristic if the fluid is exposed to the magnetic field. With the effects of magnetic field, the magnetic particles inside the carrier fluid align through the magnetic flux direction. These column shape particles increase the viscosity of the MR-fluid and changes the phase of the fluid to semi-solid. Because of the feature of the fluid, it is possible to generate the yield stress by applying certain amount of current. That makes the MR-fluid unique part of the device that generates resistive force such as clutch, brake or damper.

Several factors affect the output torque of the device. In the following section, the effects of the coil placement, disc types, material selection, MR-fluid gap and disc thickness are examined by using magneto-static analysis program.

a. Single-Disc MR-Brake

The most common configuration considering the disc types is single-disc MR-brake. The structure of the single-disc is simple than the multi-disc and the drum type MR-brakes in terms of design and manufacturing. Additionally, the performance of the device can be estimated with FEA simulation and analytical calculations.

MR-brake includes input parts where the motion is applied, and the static parts that dissipate the energy from the system. The motion is applied to the input parts of MR-

brake which are a single-disc and a shaft. They are fixed to each other, so the rotational motion is transmitted from the shaft to the disc. The gap between the disc and the case is filled with MR-fluid. The enameled wire is wound to the case in order to create a magnetic flux vertical to the MR-fluid. When the electric current is run through the coil, magnetic field lines follow a path as shown with red dashed line in the Figure 3.4.. With the existence of magnetic field, material structure of MR-fluid changes from liquid to semi-solid form. That increase the yield stress of the MR-fluid and generates a resistive force between disc and the static case.

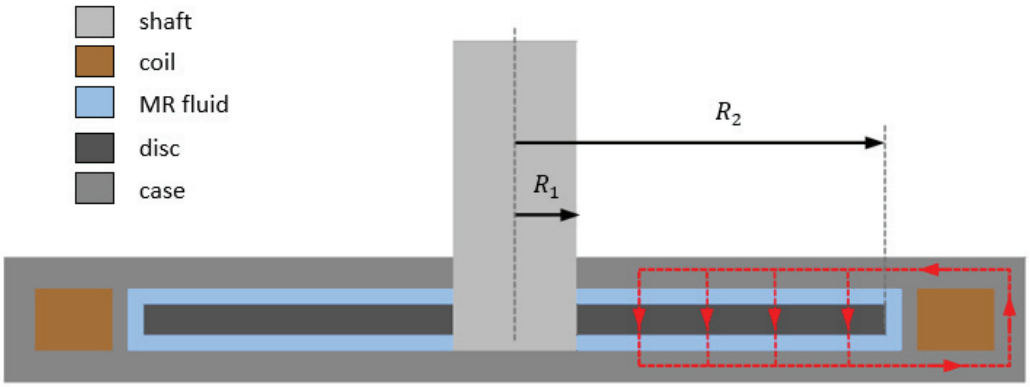

Figure 3.4. Section view of single-disc MR-brake.

MR-fluid behavior under the effect of magnetic field can be modelled by using Bingham plastic formula (3.3). In this model, shear stress τ, is proportional to the yield stress τ_y of the MR-fluid which depends on the magnetic field strength H. Shear stress can be calculated as follows;

$$\tau = \tau_y(H) + \eta(\frac{dv}{dz}) \tag{3.3}$$

where η is the Newtonian viscosity and $\frac{dv}{dz}$ is the velocity gradient in the direction of the field when Bingham plastic model is applied to the MR systems. The following formula can be derived, in where, ω is the angular velocity between input and static parts, r is the radius from the rotational axis, and g is the gap thickness which is filled with MR-fluid.

$$\tau = \tau_y(H) + \eta(\omega r/g) \tag{3.4}$$

Considering the relation between the shear stress and the resistive torque, the output torque of an MR-brake can be calculated as following;

$$dT = r\tau\, dA \tag{3.5}$$

where r is the radius, τ is the shear stress, and A is the active area of MR-fluid inside the brake. Combining formula (3.4) and (3.5), the following formula can be obtained for the resistive torque of a single-disc MR-brake.

$$T_{sd} = 2\int_{R_1}^{R_2} 2\pi(\,\tau_y(H)r^2 + \eta\left(\frac{\omega r^3}{g}\right))dr \tag{3.6}$$

As the angular velocity is getting closer to the zero when the MR-fluid becomes semi-solid, the effects of the right side of the formula becomes relatively small than the effects of the field dependent yield stress. Therefore, the right side of the formula can be neglected to simplify the formula. After this assumption, the shear stress can be expressed with the field dependent yield stress. Then, the formula for the calculation of MR-brake torque T_{sd} for single-disc design, becomes;

$$T_{sd} \approx \frac{4\pi\tau_y(H)(R_2^3 - R_1^3)}{3} \tag{3.7}$$

where R_1 and R_2 are inner and outer radius of the disc, respectively. As it can be noticed in the formula, the surface area of the disc where MR-fluid contacts, mostly affects the magnitude of the MR-brake torque. B-H curve of MR-fluid that defines the viscosity characteristics of the fluid depending on the applied magnetic field. Yield stress of the MR-fluid reaches its maximum value at 0.65 T magnetic flux density. It means that there is an upper limit for the contribution of the MR-fluid yield stress to the output torque. Regardless of the MR-fluid yield stress limitation, desired torque can be achieved by increasing the contact area between the MR-fluid and the disc.

b. Multi-Disc MR-Brake

The limitation of the B-H curve of the MR-fluid creates a need to seek diverse types of design as multi-disc or drum-type. As it can be noticed in the formula (3.7), the torque capacity is proportional to the disc surface area that is in contact with the MR-fluid. Therefore, by increasing number of the discs, it is possible to achieve high resistive torque within the same outer radius of case. In other words, n number of discs increase

the torque n times by enlarging the contact surface. Figure 3.5. shows the design named in the literature as multi-disc MR device. In this design, n number of inner discs are fixed to the shaft and rotating synchronously. There are counterparts of inner discs, which are called outer discs. Since the outer discs are fixed to the case, shear stress occurs between the inner and outer discs as the MR-fluid takes semi-solid form.

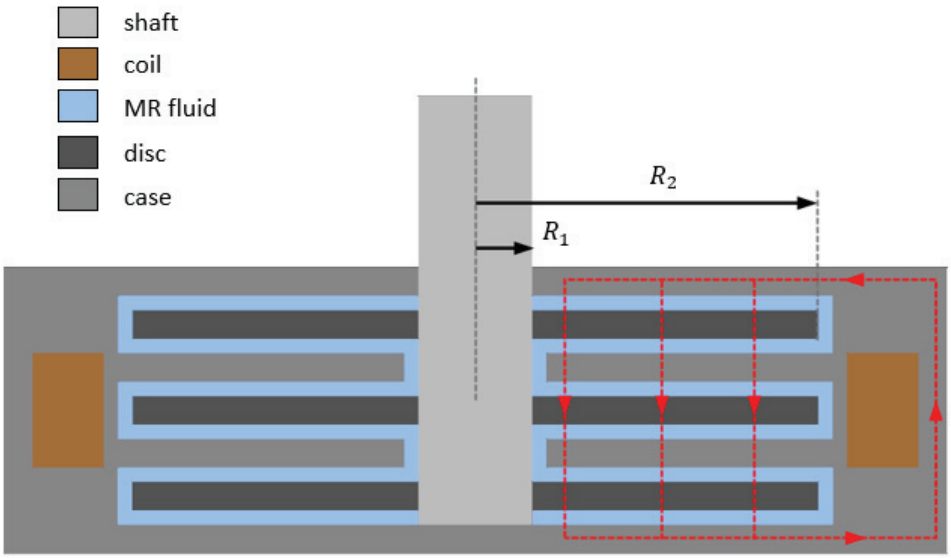

Figure 3.5. Cross sectional view of a multi-disc MR-brake.

The formula of multi-disc MR-brake with *n* number of inner discs can be derived from the single-disc MR-brake formula (3.7),

$$T_{md} \approx \frac{4n\pi\tau_y(H)(R_2^3 - R_1^3)}{3} \tag{3.8}$$

where all parameters are defined previously. The formula clearly shows that the output torque of the MR-brake is increased proportional to the number of discs. However, yield stress τ_y is a parameter that depends on magnetic field strength H, and increasing the number of discs can decrease the magnetic field effect on MR-fluid.

c. Drum Type MR-Brake

A drum-type MR clutch is one of the easiest design in terms of production and shows a satisfactory performance. The mechanical structure of drum type MR-brake consists of moving and static parts. The moving part includes a cylindrical disc mounted to the rotary shaft and the yield stress is created by the yield stress of MR-fluid filling the gap between the cylindrical disc and the static case.

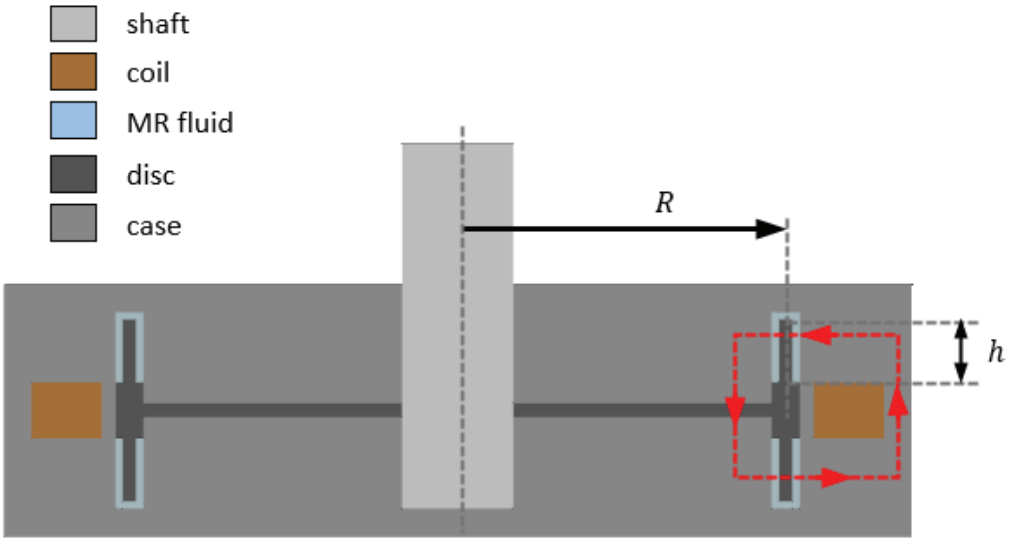

Figure 3.6. Cross sectional view of a drum type MR-brake.

Similar to the previous two designs, Bingham plastic model can be applied for the calculation of drum type MR-brake torque T_D. Then, the formula can be written as,

$$T_D \approx 4\pi\tau_y(H)R^2h \tag{3.9}$$

where R is the radial distance from the rotational axis, h is the height of the cylindrical disc, and τ_y is the magnetic field H dependent yield stress.

In this section, formulae of resistance torque for single-disc, multi-disc and drum type MR-brake configurations are discussed. In order to define the behavior of MR-fluid, Bingham plastic model is used. Using the given formulae for each configuration, torque calculation depending on disc configuration can be done. In the following section, all the

configurations are compared using FEA simulation. Besides magnetic properties, mechanical properties such as weight, volume, and sizes of parts are considered and results are shown in table. This knowledge will lead us to design a device with a superior performance with optimized mechanical properties.

3.1.4. Coil Position

The magnetic field strength depends on the permeability, applied electrical current and the density of the enameled wire. In other words, coil placement, number of turns and the material permeability directly affect to the performance of MR-brake device. Therefore, in this section coil placement is chosen as design criteria and investigated in terms of magnetic field effects. Besides the common two types design, to demonstrate the effects of the coil position, three types of coil positioning are introduced. As a result, the effects of placement are shown in a table and discussed.

In general, there are two types of coil placement inside the MR devices. It is called inner coil, when the coil located around the shaft, and outer coil, when it is located around the case. In inner coil type, copper wire which is the part where electric current is applied to create magnetic field, is wound around the shaft to get a solenoid shape. Another possible positioning is two-sided coil positioning in which coil is placed both side of the disc. It is not a common design that was encountered in literature survey.

When the electric current runs through the coil, magnetic field lines follow a path as shown in Figure 3.7. and pass through the MR-fluid vertically. A strong magnetic field arises at the center of the shaft. The magnitude of the flux density is directly proportional to the material permeability and the electric current. However, the magnetic field weakens as it gets further away from the center of the coil.

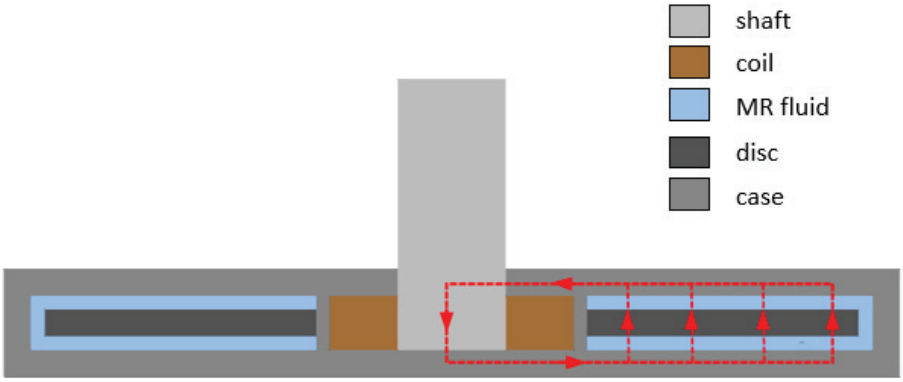

Figure 3.7. A single-disc MR-brake with inner coil.

In the other design, coil is located at the outer side of the MR-fluid wrapping around the case as seen in Figure 3.8.. Electric current in a circular loop of enameled wire creates a magnetic field around the wire. As the inner diameter of the loop is too wide, magnetic field is weaker at the center of the circular loop and it is stronger near the enameled wire.

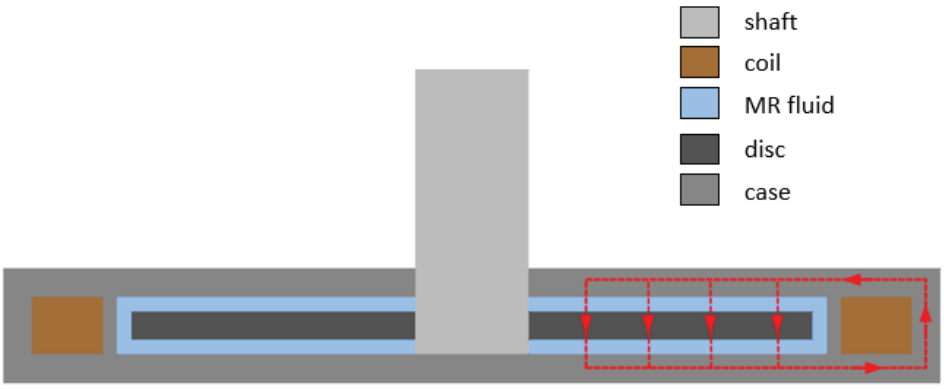

Figure 3.8. A single-disc MR-brake with outer coil.

In the last design, two-sided coil design is introduced in Figure 3.9. where the coil is positioned on two sides of the disc and MR-fluid. By using two coils, it is feasible to increase the magnetic field effect on MR-fluid. Inner and outer coils generate two

different magnetic fields separately and the magnetic field lines are in the same direction as shown in Figure 3.9.. There are two ways to sum up the magnetic field strength of both coils. Either the coils are wired in different direction, e.g. when inner coil wired in clockwise, the outer coil must be wired in anti-clockwise direction, or if the coils are wired in the same direction, the applied current must be in opposite direction. For instance, when applying 1 A electrical current on inner coil, the magnitude of applied current on outer coil must be equal to -1 A.

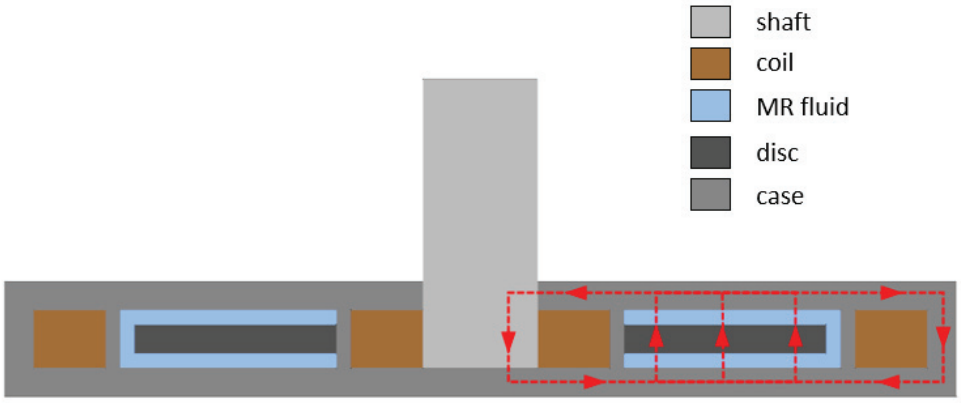

Figure 3.9. A single-disc MR-brake with two-sided coil.

3.1.5. FEA Simulation

In this section performance of the MR-brake configurations are discussed. Performance describes the output torque capacity of the device with the similar mechanical properties. In order to validate the results under the same conditions, some of the properties such as the outer case diameter, coil volume, electric current is chosen identical for all different configuration of designs. Other than disc configurations, disc thickness and fluid gap size are examined to see how magnetic field changes.

Figure 3.10. Torque calculation using FEA simulation.

Figure 3.10. shows the steps of how the output torque is calculated by using design, simulation, and analysis program. First, 3D designs are created for each configuration using Siemens NX. In order to simplify the design process, different configurations are created as a part family by attaining parameters. Parameters and material selections are shown in Figure 3.11.. R_1 and R_2 are inner and outer radius of the disc, n is the number of disc, g is the MR-fluid gap thickness, and d is the disc thickness.

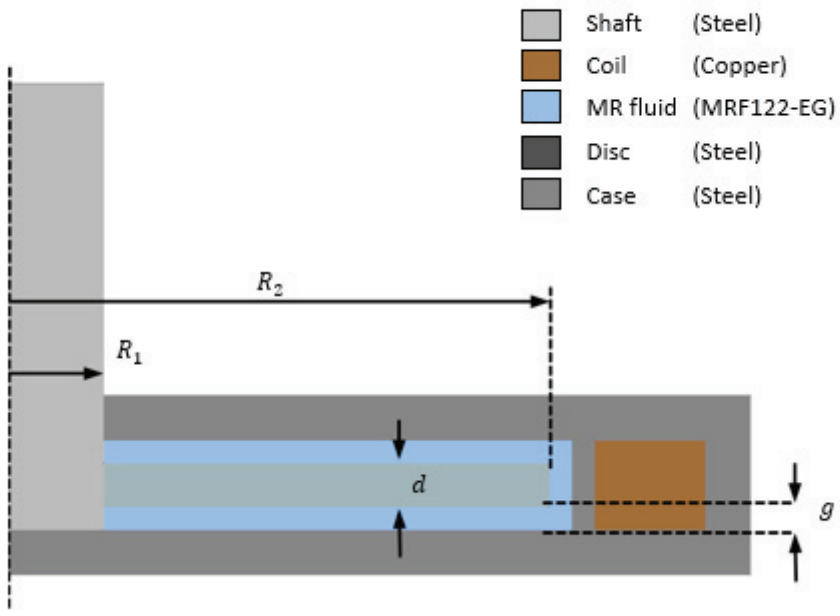

Figure 3.11. Cross sectional view of a single-disc MR-brake.

In simulation, magneto-static package of ANSYS is used to simulate the magnetic field. At first, magnetic properties of the materials must be selected in the program. As mentioned in the material selection section, if the material exhibits non-linear magnetic properties, it must be defined by using B-H curve. If it is linear magnetic material, magnetic properties can be defined by relative permeability constant. For the simulations, the materials are defined as shown in Figure 3.11.. MRF-122EG is selected as MR-fluid, copper is chosen for coil material, and the rest (shaft, disc and case) are defined as structural steel which is a ferro-magnetic material. The material selection affects the magnetic field strength and magnetic field lines directly.

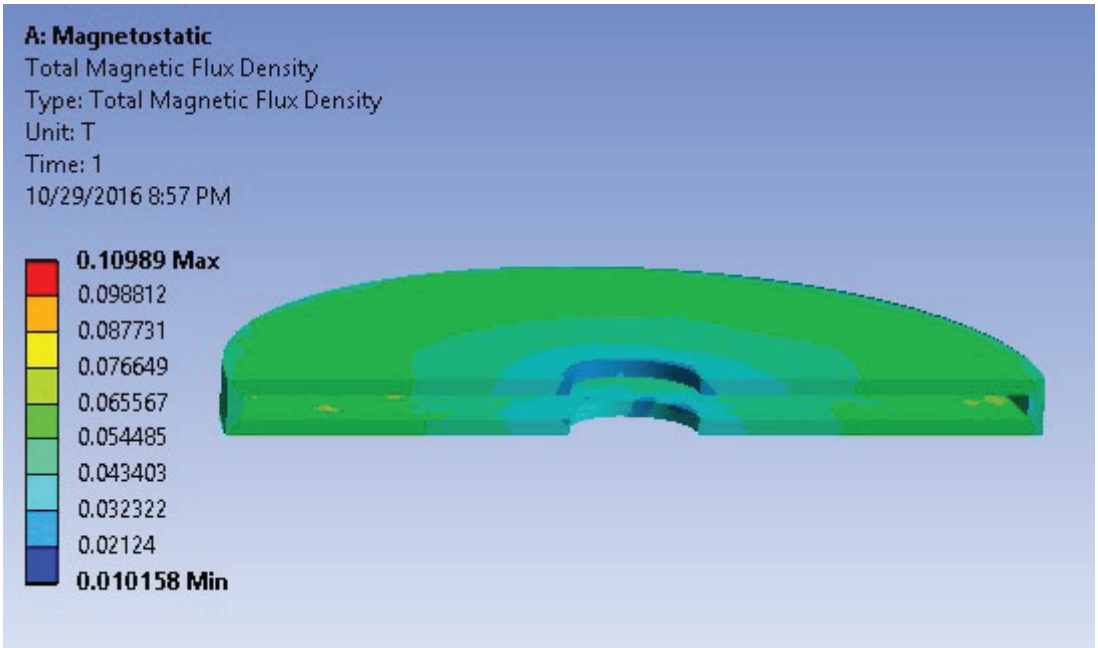

Figure 3.12. Magnetic flux density of MR-fluid in a single-disc configuration.

As a result of magneto-static simulation, magnetic flux density and magnetic field strength are obtained. The focus of the simulation is to see the magnetic field that affects the MR-fluid. For instance, Figure 3.12. shows the magneto-static simulation result for single-disc MR-brake configuration. The results can be obtained for each node that occurs by meshing. By taking the average of the magnetic field value corresponding to all nodes, the mean values for each simulation are calculated. These values describe the mean

magnitude of magnetic field strength and magnetic flux density that affects the MR-fluid. The magnetic properties of the chosen MR-fluid (MRF-122EG) are calculated in MATLAB by using the data in Figure 3.2. and Figure 3.3.. As a result of that, yield stress can be calculated by using the mean values of magnetic field strength or magnetic flux density from the simulation. Using that magnetic field dependent yield stress as an input in formulae in (3.7), (3.8) or (3.9) for single-disc, multi-disc or drum type disc configuration, the torques are calculated in MATLAB. These steps are repeated for all disc configurations.

3.2. Experimental Methodology

MR-brake prototype is tested in a test rig that includes a torque sensor, a dc motor with timing belt and pulleys aside from the MR-brake prototype. The differential torque between the MR-brake and the generated torque is measured with the rotary type torque sensor. Experimental setup consists of the MR-brake prototype mounted to the test rig, and hardware and software for data acquisition.

3.2.1. Test Rig

The main purposes of the test setup are to validate the torque characteristic of the MR-brake, investigate the response time of the braking and perform tests for the bidirectional braking function.

To determine the relation between the braking torque and the applied current, FUTEK's TRS300 series rotary torque sensor is employed. This shaft-to-shaft type rotary torque sensor measures the torque difference between the input and the output shafts within the 10 Nm capacity range. One of the output shafts of the rotary torque sensor is attached to the MR-brake's shaft. The other output shaft is mounted to the shaft that transmits the torque generated by the 24V DC motor which has 1 Nm torque capacity. Since the torque capacity of the DC motor is relatively small compared to the MR-brake, timing pulleys and a belt with 6:1 ratio are used. The AEDA-3300 series three-channel

optical incremental encoder provides maximum 80000 counts per revolution resolution after quadrature (4X) decoding. It is mounted to the output shaft of the MR-brake to sense the rotary motion of the MR-brake.

Sigma profile is used for test stand to achieve a rigid structure. Assembled test rig is shown in Figure 3.13..

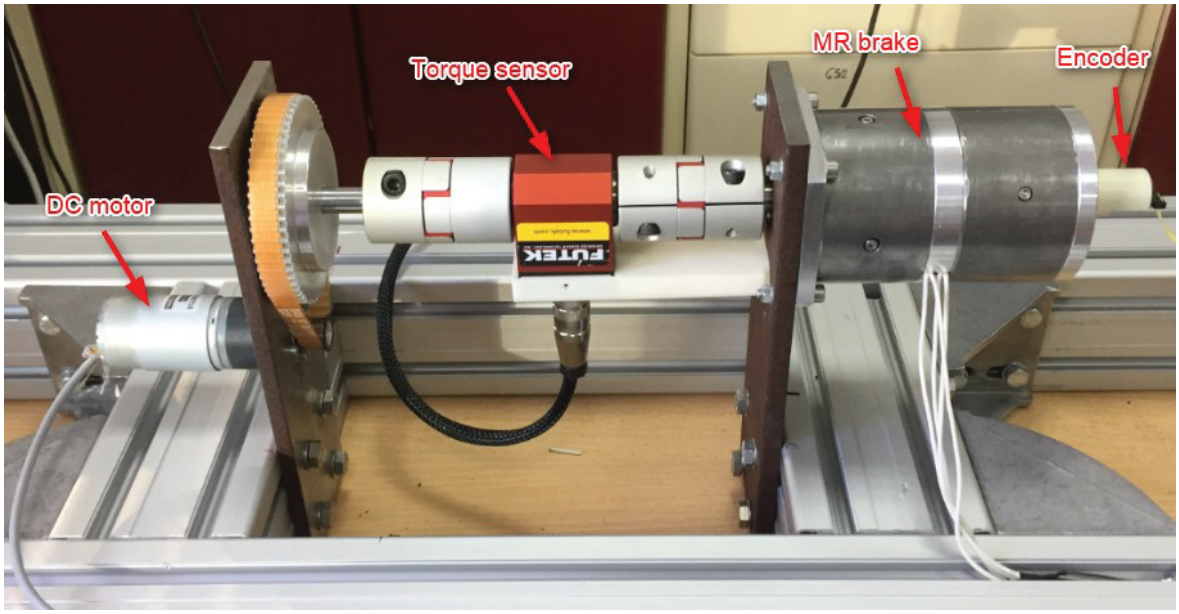

Figure 3.13. Experimental test setup.

3.2.2. Data-Acquisition and Control System

Data-acquisition (DAQ) system consists of sensors, DAQ hardware and the computer that runs the software for data-acquisition process. There is a shaft-to-shaft rotary torque sensor and two encoders, one of them is connected to the shaft of MR-brake and the other is connected to the rear end of the shaft of DC motor. Test setup requires control of the MR-brake and the DC motor. Therefore, Quanser Linear Current Amplifier Module (LCAM) and Maxon servo-amplifier drivers are employed. An illustrative diagram of test setup shows the system including 3D model of the test rig with DAQ is shown in Figure 3.14..

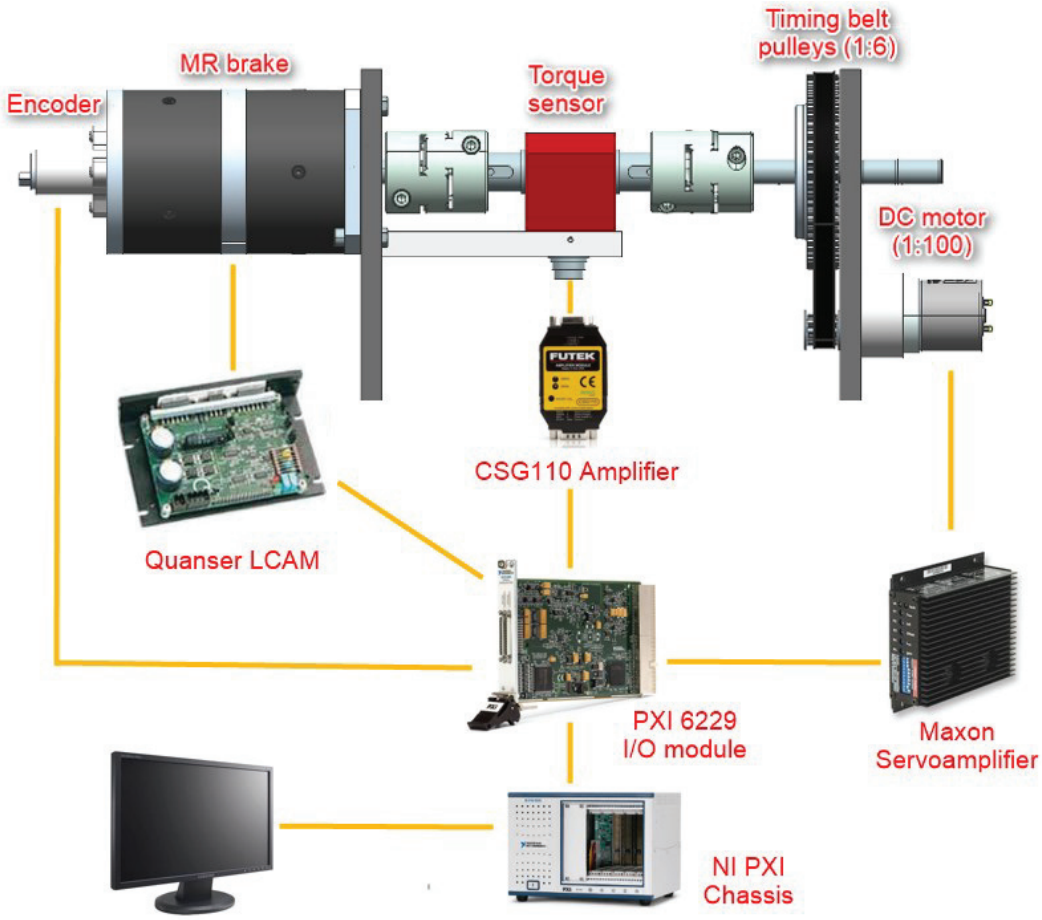

Figure 3.14. The experimental test diagram.

In order to test the MR-brake design prototype, torque, position and current signals must be monitored while controlling the MR-brake and the DC motor. The signal received from the sensors must be processed and converted from analog to digital signals before they are monitored or manipulated. CSG110 module amplifies the signal coming from the torque sensor to the voltage level which is proper for the DAQ device (for specifications see Appendix A). For signal processing and analog-to-digital converting (ADC), PXI-6229 I/O module and the chassis from National Instruments is employed as a DAQ hardware (for specifications see Appendix B). PXI chassis runs with windows operating system and communicates with PXI-6229 I/O module using BUS. In this way, the analog signals of sensors and drivers can be monitored and controlled with Simulink Desktop Real-Time™ in external mode running under windows.

If the current-torque relation is known, this data can be used in a look-up table to control the MR-brake. Therefore, the current-torque relation is obtained by driving electrical current to the MR-brake as a ramp signal from 0 A to 2 A (max limit). The control is done with linear amplifier module from Quanser which also gives the opportunity to monitor applied electrical current. On the other side, the DC motor is driven with the servo-amplifier by Maxon Motors with a full capacity. Then the differential torque between the generated torque and the braking torque is measured along with the applied electrical current and the rotary position.

The experimental test equipment for DAQ, and control hardware and software are listed in the Table 3.2.

Table 3.2. The list of hardware and software used in test setup.

Hardware	**Software**
MR-brake	MATLAB® Simulink
PXI-1071, PXI Chassis (National Instruments)	
PXI-6229, I/O module (National Instruments)	
Servoamplifier, LSC 30/2 series (Maxon motor)	
Linear current amplifier module (Quanser)	
Torque sensor, TRS300 series (FUTEK)	
CSG110 Amplifier (FUTEK)	
24 V DC Motor	

3.3. Conclusion

The performance of the MR-brake represents the ratio between the generated torque capacity and the volume. In this chapter, it is aimed to develop an improved performance MR-brake. Therefore, the criteria that effects the performance must be studied. First, the system is modeled by using Bingham plastic formula and FEA simulation in order to see the effects of changes in the system configuration.

It is known that the output torque capacity strongly depends on the solidification of the MR-fluid which is controlled by the magnetic field strength. When the analytical model is used in the simulations, the output torque of the MR device can be estimated. This method is used to compare the different design configurations such as drum, single-disc and multi-disc type MR-fluid brakes. Besides that, other design parameters as MR-fluid gap width, disc thickness and coil location are discussed in terms of performance. As a result, an optimized multi-disc MR-brake design is proposed.

The design is developed by taking into consideration the manufacturing facilities. Structural steel is utilized as a ferromagnetic material and aluminum is used as a non-ferromagnetic material. Plastic can also be suitable candidate for a non-ferromagnetic material considering the 3D manufacturing possibilities. With the proposed design, requirements regarding the performance and the optimization are fulfilled by achieving 5 Nm torque capacity within a 32 mm outer case radius.

CHAPTER 4

DESIGN OF THE MR-BRAKE

In the previous chapter, existing MR-brake designs are investigated and compared to develop an optimal design. It is observed from this comparison that the multi-disc MR-brake design shows a better performance than the single-disc and drum type MR-brake.

Even though the multi-disc MR-brake has many advantages, as a final design, drum type MR-brake is chosen as considering the bi-directional functionality. Since the focus of this thesis is to design an MR-brake to be used in haptic applications, developed MR-brake should be able to work in two directions independently. Then, the MR-brake can overcome the sticking problem which is mentioned in detail in the literature review chapter.

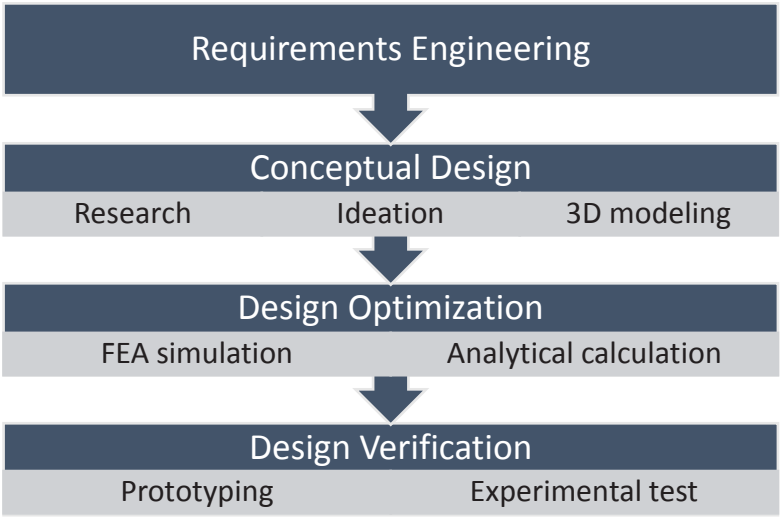

Figure 4.1. Design process of the MR-brake.

In this chapter, final design of the developed MR-brake is introduced with the design considerations such as sealing, material selection and the mechanism design. The design process starts with the conceptual work which includes research, requirements determination, ideation and 3D modeling. After achieving an operational model, it is

optimized with FEA simulation and analytical calculations. Design optimization aims to obtain an optimal volume while maximizing the torque capacity of the design. By carrying out experimental tests, the final product is characterized. Detail of the experimental test procedure and the results are given in the following chapter.

4.1. Requirements of the Design

The final product is planned to be used in a new version of HIPHAD. The first version of HIPHAD shown in the Figure 4.2. is designed and developed in IZTECH robotics lab (Bilgincan et al., 2010). The HIPHAD v1.0 has hybrid mechanism that is composed of a 3-DoF parallel R-Cube structure and a 3-DoF serial wrist mechanism. Thanks to the parallel R-Cube mechanism, the haptic device can generate only forces at the end-effector. Even though the parallel structure provides great mechanical stiffness, the capacity of the electrical motors does not satisfy to simulate high stiff walls, because some of the power of the motors are consumed during the gravity compensation.

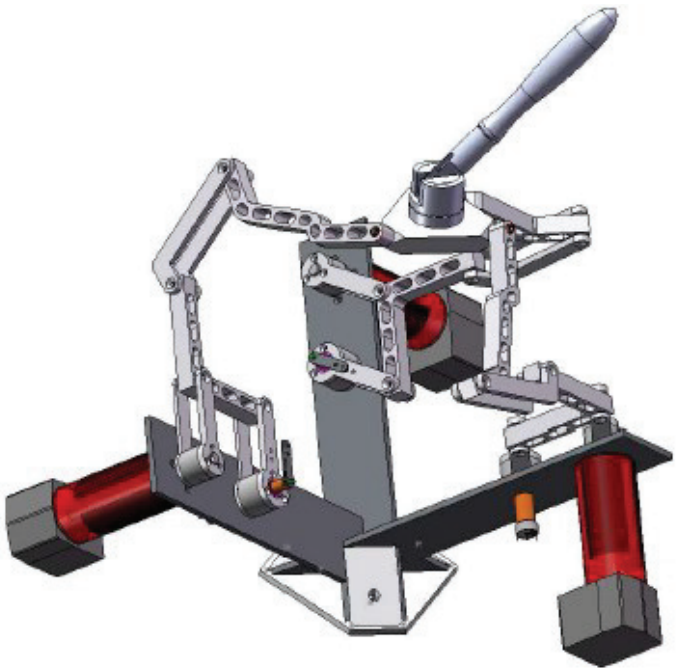

Figure 4.2. 3D model of HIPHAD v1.0
(Source: Bilgincan et al., 2010).

By keeping the friction of the system at minimum, we can lower the minimum impedance in free motion but it also restricts to achieve high impedance which means maximum displayable stiffness. The use of variable dampers such as MR-brake damper can increase the maximum impedance while keeping the lower impedance at minimum which means a better Z-width because of its unique feature.

The requirements of the MR-brake design are defined by considering the future place of use. As being a semi-active actuator, the final product should exhibit high torque with an optimal volume and inertia. Considering the structural mechanism of the HIPHAD, the output torque is targeted as 3 Nm which is 10 times stronger than the previous actuation system. In order to minimize the lower impedance, the moment of inertia must be minimum which means the design should be compact. Operational maximum current is defined 2.0 A to avoid any heating problem. More details about dimensioning and the design is given in the following sections.

4.2. Conceptual Design

In the previous chapter, all existing design types are examined considering the performance which represents the ratio between the generated torque capacity and the volume. The types of MR-brake design can be listed as single-disc, multi-disc and drum. FEA simulation results show that the best performance is achieved with multi-disc MR-brake. However, placing coil around the shaft requires commutator as an additional part to transmit the electrical current from static part to rotary part. Placing coil around the case which is static part, decrease the magnetic field effect on the MR-fluid. According to the previous experience, it is considered that multi-drum type MR-brake is more suitable in terms of manufacturability and performance with respect to multi-disc MR-brake.

4.2.1. Design Parameters

In the previous section, different disc configurations (drum, single- and multi-disc) are defined for MR-brake design. To obtain an optimized design with a good torque performance, different design configurations are compared in terms of magneto-static effects. In order to simulate the magnetic field effects, magneto-static analysis tool of ANSYS is used. The focus of the simulation is to determine the strength of the magnetic field, especially the field acting on MR-fluid. After the simulation result is obtained, the output torque is calculated by using analytical methods as mentioned in the previous section.

Before comparing different disc type configurations, MR-fluid gap and disc thickness are investigated in a single-disc configuration. In the simulation, it is aimed to observe the magnetic field effects for the different type of designs so that the magnetic field effect on MR-fluid can be seen for different variation of design variables. For instance, Figure 4.3. shows the magneto-static analysis result for a single-disc MR-brake configuration.

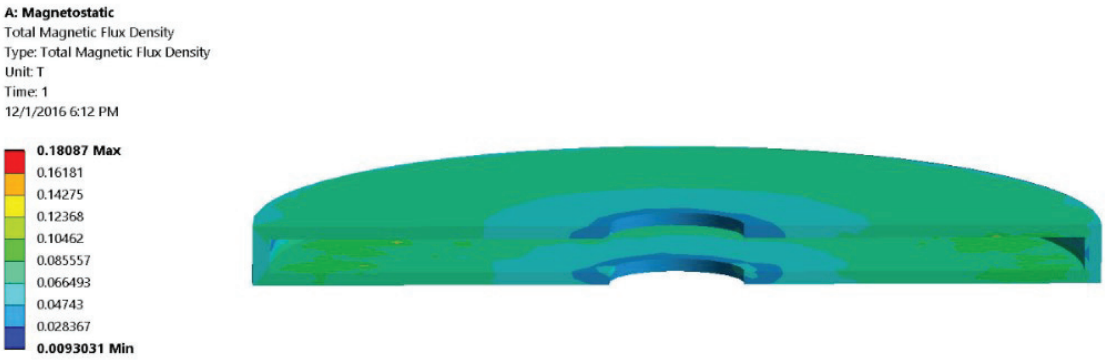

Figure 4.3. Magnetic field density on an MR-fluid of a single-disc.

Disc thickness is an important design variable since MR-fluid is located between disc and case. Therefore, it is investigated in terms of magneto-static effects. Table 4.1 shows the disc thickness comparison results. To make the comparison fair, initial conditions are defined identical and same input value as electrical current (2 A) is set.

Three different disc thickness as 1, 1.5 and 2 mm are chosen due to the manufacturability from the sheet metal. From the result, it can be noticed that the disc thickness has small effect on magnetic field density B. Therefore, the output torques T are similar for three different disc thicknesses.

Table 4.1. Disc thickness comparison chart.

d (mm)	$\boldsymbol{B}$ (T)	$\boldsymbol{\tau_y(H)}$	$\boldsymbol{T}$ (Nm)
1	0.0565	1.4773	0.09
1.5	0.0590	1.6166	0.09
2	0.0604	1.6924	0.10

Since the MR-fluid is a non-linear ferromagnetic fluid, the fluid gap should be investigated in terms of magneto-static effects, as a design criterion. MR-fluid gap widths g are chosen as 0.5, 0.75, and 1 mm depending on the manufacturing facility's capability. In order to make a fair comparison, all of the different gap sizes are adapted in a single-disc MR-brake configuration. The simulation results of different gap widths are compared in Table 4.2. From the given result, it can be observed that decreasing the gap width where MR-fluid filled in, increase the magnetic flux density that effects B on MR-fluid and the yield stress of the fluid $\tau_y(H)$. Consequently, that makes the output torque T proportionally larger.

Table 4.2. MR-fluid gap width comparison chart.

g (mm)	$\boldsymbol{B}$ (T)	$\boldsymbol{\tau_y(H)}$	$\boldsymbol{T}$ (Nm)
1	0.0604	1.6924	0.10
0.75	0.0749	2.2559	0.13
0.5	0.0866	2.6457	0.15

Apart from the disc thickness and the MR-fluid gap width, coil placement is another important parameter for the magnetic field effect. The coil location is named as inner when it is wound on the shaft, and it is named as outer when it is placed inside the

case. The section-views of 3D models for both inner and outer coil placements are shown in Figure 3.7. and Figure 3.8.. Two-sided means when the coil is positioned on two sides of the discs and MR-brakes which is shown in Figure 3.9.. Using the identical initial conditions, the magneto-static effects and torque capacity are examined for the coil placement and the result is given in Table 4.3. From the result, it can be observed that the outer coil placement (Figure 3.8.) enhances the magnetic flux density *B*, consequently, doubles the output torque *T* compared to the inner type coil design. Even though the magnetic field strength is expected to be greater than the inner or outer coil positioning, the results show that by using two-sided coil, the magnitude of the magnetic flux density is closer to outer type design. Eventually, the output torque of two-sided coil design is the same with the outer coil type design. Comparing the manufacturability of two sided and outer type of coil design, it is wiser to choose the outer coil type design.

Table 4.3. Coil location comparison chart.

Coil location	$\boldsymbol{R_1}$ (mm)	$\boldsymbol{R_2}$ (mm)	$\boldsymbol{B}$ (T)	$\boldsymbol{\tau_y(H)}$ (kPa)	$\boldsymbol{T}$ (Nm)
inner	10	30	0.0156	0.4394	0.05
outer	4	24	0.0604	1.6924	0.10
two sided	10	24	0.0646	1.8924	0.10

After clarifying the magneto-static effects of the disc thickness considering the MR-fluid gap width and the coil positioning, the magneto-static effects for the given design configurations are fully evaluated. In order to compare different design configurations according to the dynamics of the system, two different methods of evaluation can be employed. First, using the same input conditions that is the electrical current for this case, the generated torque as system output capacity can be compared. Second, defining the output capacity of the system identical, the required input, in other terms, electrical power of the system can be identified. However, in this chapter, we only examine the output capacity of the system by taking the input and design variables identical. Accordingly, electrical current input is set as 1 A, inner and outer radius of discs are 4 and 24 mm, respectively. As a result, for the same input electrical power, the magnetic field effects and output torque capacity are observed.

Evaluation results for different design configurations of MR-brakes are shown in Table 4.4. Magnetic flux density B is observed by using magneto-static analysis. Corresponding yield stress $\tau_y(H)$ value to the magnetic field strength and the output torque T are calculated by ANSYS program analytically using B-H curve of the MRF 122-EG and the formulae (3.7), (3.8) and (3.9).

Table 4.4. MR-brake design configurations comparison chart

Configurations	$\boldsymbol{B}\ (T)$	$\boldsymbol{\tau_y(H)}$	$\boldsymbol{T}\ (Nm)$
Drum	0.1100	3.5517	0.25
Single-disc	0.1475	5.3654	0.31
Multi 3 disc	0.1535	5.5918	0.97
Multi 5 disc	0.1692	6.3388	1.83
Multi 7 disc	0.1679	6.2785	2.53

As it is expected, the number of disc does not affect the magnetic field strength. However, formula (3.8) declares that the output torque of the system is proportional to the number of discs since the generated torque depends on the surface area of the disc interacting with the MR-fluid. If the performance is considered as a ratio between torque capacity and the volume, drum type MR-brake exhibit a poor performance. In conclusion, multi-disc design configuration with 1 mm disc and 0.5 mm MR-fluid gap is a good choice to achieve a strong output capacity with an optimized size.

4.2.2. Design Optimization Methodology

In this section, an optimized design is proposed. During the design process, the outcomes of simulations are used. All MR-brake types, are evaluated and as a result of that the device that fulfills the requirements is conceptually designed. In short, for the output torque it is desired to achieve 5 Nm with at least 0.46 T magnetic flux density. Due

to the limitations of space, outer diameter of the device must be less than 35 mm. All requirements are discussed in detail in the following chapter.

The aim of the optimized design is to achieve high resistive torque within a limited diameter and to optimize the volume for minimizing the inertial force. Figure 4.4. shows the parameters in a sketch drawing for cross sectional view of an MR-brake design. Disc represents the place where multi-discs and MR-fluid are located. Defining the materials for shaft, flux part and discs as ferromagnetic and the rest as non-magnetic, the magnetic field lines will follow red dashed line and pass through discs vertically as shown in Figure 4.4..

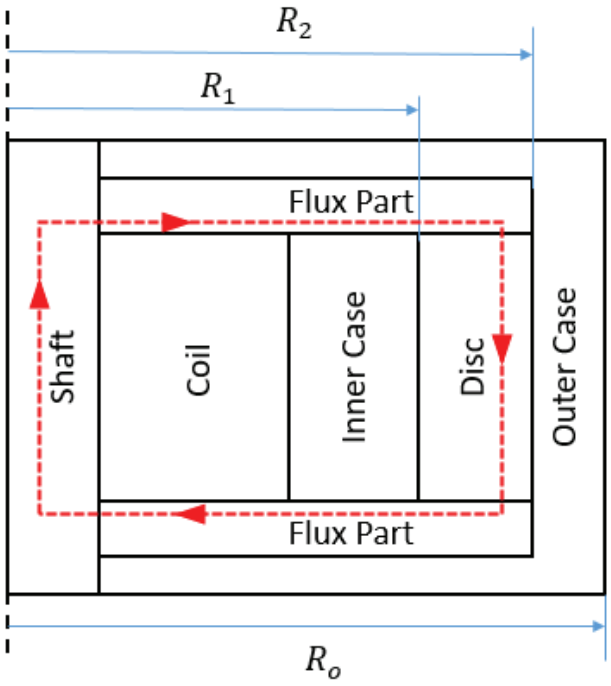

Figure 4.4. Conceptual design of MR-brake.

Table 4.5 shows the parameters and the values for the width dimensions of parts used MR-brake. The diameter of shaft is chosen 10 mm by considering the applied torque. The inner case thickness can be minimum 7 mm. The unknown parameters for design are R_0, the outer case radius, R_1 and R_2 the inner and outer disc radii. Since there is only one formula for the torque calculation, there must be also only one unknown parameter. Outer case radius can be defined as a constant and R_1 is the parameter that depends on

shaft coil and inner case dimensions. Shaft and inner case have been already defined and after defining the coil volume, R_1 can be calculated.

Table 4.5. Dimensional parameters and variables for optimized design.

Part	**Width (mm)**
Shaft	5
Coil	C_w
Inner case	7
Disc + MR-fluid	$R_2 - R_1$
Outer case	$R_0 - R_2$

Due to given conditions and the American wire gauge (AWG) table which is used for determining the current carrying capacity, 24 AWG copper wire is selected. As seen in Table 4.6, the diameter of 24 AWG is 0.511 mm and allowable ampacity is equal to 2.1 A for 75 ℃ conductor temperature.

Table 4.6. American Wire Gauge (AWG) sizes and properties.

AWG	**Diameter (mm)**	**Area (mm^2)**	**Resistance/length ($m\Omega/m$)**	**Current ratings (A)**
20	0.812	0.518	33.31	7.5
21	0.723	0.410	42.00	6.3
22	0.644	0.326	52.96	5
23	0.573	0.258	66.79	3.5
24	**0.511**	**0.205**	**84.22**	**2.1**
25	0.455	0.162	106.2	1.7
26	0.405	0.129	133.9	1.3

The enameled wire area is selected considering the current carrying capacity and coil resistance. Allowable current density for copper wire can vary from 2.5 A/mm^2 to 6 A/mm^2 depending on isolation from air. The current density J_D can be calculated as:

$$J_D = \frac{I}{\sqrt{3}d^2} \tag{4.1}$$

where I is the applied electrical current, and d is the diameter of the copper wire. Using the formula (4.1) for 2 A electrical current, current density can be found 4.62 A/mm^2, less than allowable current for 24 AWG copper wire.

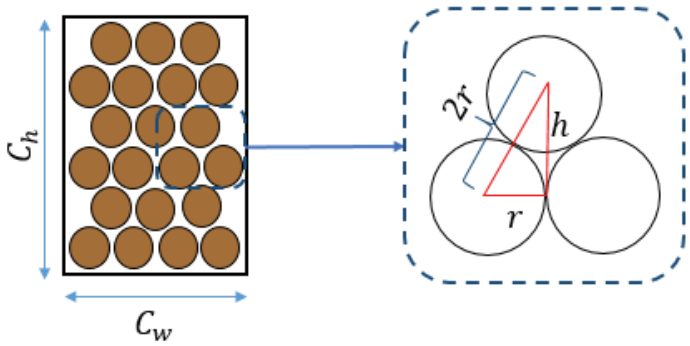

Figure 4.5. Cross sectional view of an enameled wire in coil.

Figure 4.5. shows the cross-sectional view of stranded copper wire in a coil. C_w is the width and C_h is the height of the cross-sectional coil. Those parameters can be determined by considering the heat conditions. For the FEA simulation, the number of turns of wire in the coil must be defined in the program. In order to find the number of turns, the number of turns in column is defined as:

$$i = \frac{C_h - 2r}{\sqrt{3}r}, \qquad i \in Z^+ \tag{4.2}$$

where i is the number of the wire in a column and r is the radius of the wire. Using i in the following formula the number of turns N_c in terms of C_w and C_h can be calculated as:

$$N_c = \frac{C_w}{2r}(i+1) - \frac{i}{2} \tag{4.3}$$

4.2.3. Initial Design of MR-Brake

In the previous chapter, different design configurations for MR-brake are introduced. Besides those design configurations, several design criteria are discussed by

simulating the magnetic field effect with magneto-static analysis. Using identical input conditions and design variables, the output capacities of different variations are compared. As a result of this evaluation, the MR-brake design for the maximum torque performance with an optimize volume is suggested.

Some of the design variables are defined in this chapter. The rest of them are decided by making some assumptions and taking into consideration the desired output torque which is about 3 Nm. One of the mentioned assumptions is to consider that 0.46 T magnetic flux density is reached for the suggested design. For the given condition, magnetic field depended yield stress $\tau_y(H)$ of the MRF-122EG is equal to 24.315. When R_1 and R_2 are chosen as 22.5 and 27.5 for the inner and outer disc radius, the output torque can be found as 0.958 Nm using the formula for a single-disc configuration which is introduced in (3.7). As previously stated, the output torque capacity can be enhanced proportionally by increasing the number of discs that is introduced as multi-disc configuration. The multi-disc MR-brake design with the proposed specifications is shown in Figure 4.6.. Magnetic field lines tend to close the loop through the ferromagnetic materials. By using the magnetic material only for the shaft, flux part and the discs, and non-magnetic for the rest, magnetic field line is forced to follow the path shown in dashed line. Therefore, magnetic field lines pass through the discs and affect the MR-fluid vertically.

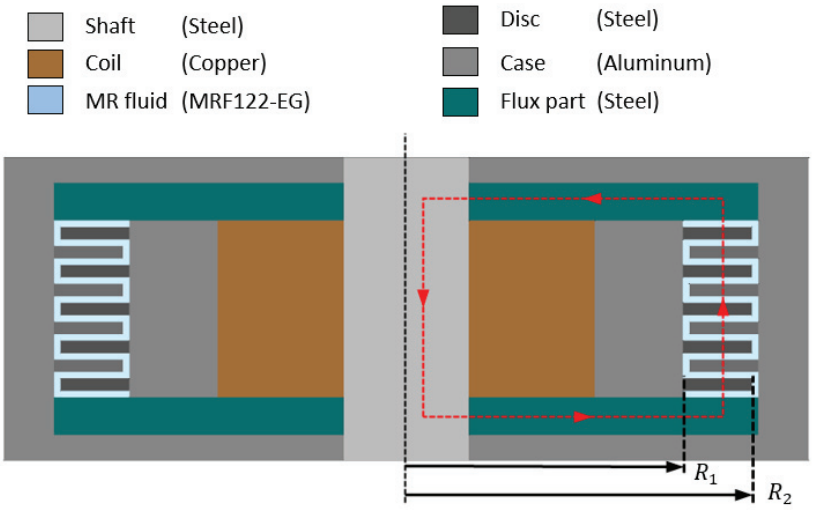

Figure 4.6. Cross sectional view of optimized multi-disc MR-brake.

The magnetic flux density occurring on the MR-fluid for the proposed multi-disc design is shown in Figure 4.7.. It can be seen that magnetic flux is uniform on vertical surfaces. That means the yield stress of the MR-fluid is more predictable. The mean value for the magnetic flux density is equal to 0.4865 T. When it is used in the multi-disc formula given in (3.8), the output torque can be calculated as 5.02 N.

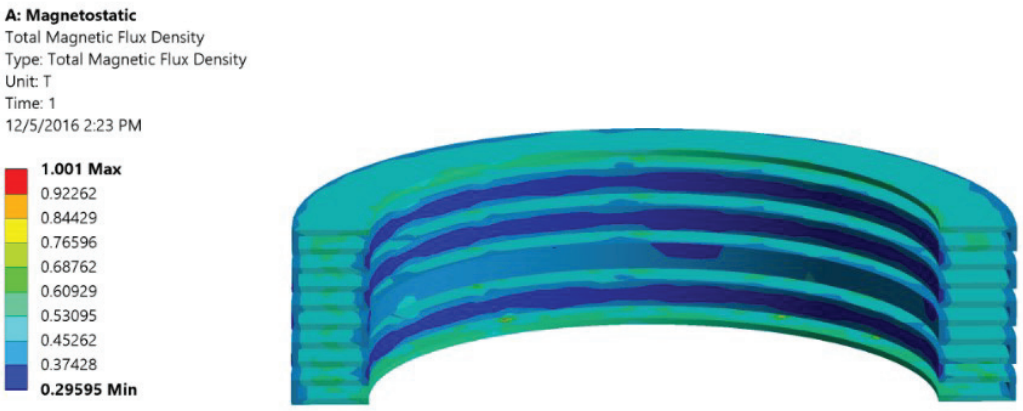

Figure 4.7. Magneto-static simulation result for the proposed multi-disc MR-brake design.

4.3. Final MR-brake Design

The cross section view of the 3D model of final MR-brake design is shown in Figure 4.8.. The MR-brake consist of two identical drum type MR-brakes which are mounted opposite to each other divided by a separator. The only rotating parts in the assembly are rotary cylinders that are fixed to the rotary part. There is MR-fluid between the rotary cylinders and the static cylinders. Rotary part is mounted on to the shaft with a one-way bearing which lets the motion free in one direction. In the reverse direction, even though the magnetic field affects the MR-fluid, the brake torque is not transmitted to the shaft since the rotary part and the shaft are decoupled. However, second MR-brake which is at the bottom side, is assembled with the one-way bearing that engages in the opposite direction.

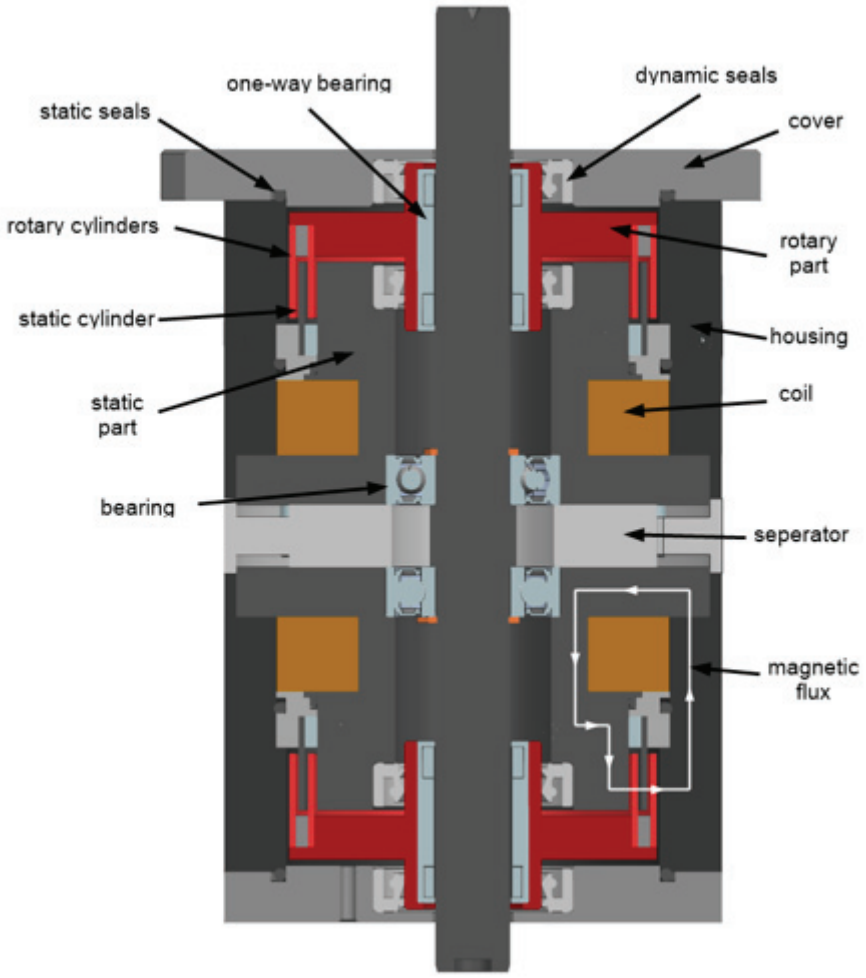

Figure 4.8. 3D model of the final MR-brake design.

First and second MR-brakes have separate coils to control directional brake function independent from each other. For instance, considering the right-hand direction is positive, the first one way-clutch couples with the shaft in positive direction and the second one-way bearing couples in negative direction. That means, when motion is given in the negative direction, braking can be done by stopping the second rotary part motion by supplying current. However, on the second MR-brake, shaft can rotate freely in positive direction, although the negative direction brake is on. The same working principle also is true for the reverse direction. When the semi-active actuator is used in haptic device, bi-directional brakes are essential to overcome the sticking problem.

As an initial work in this thesis, 1-DoF haptic device is developed using two MR-brakes in a four-bar mechanism. Here, the MR-brake is fixed to the ground with one-way

bearing which allows free motion in one direction. That means, when the MR brake is on, the brake function works for one direction due to the one-way bearing. For instance, when the left brake is active, the user feels the resistance torque to the left side. For the reverse direction, even though the left MR-brake is on, the user can move the handle to the right direction (Karabulut et al., 2015).

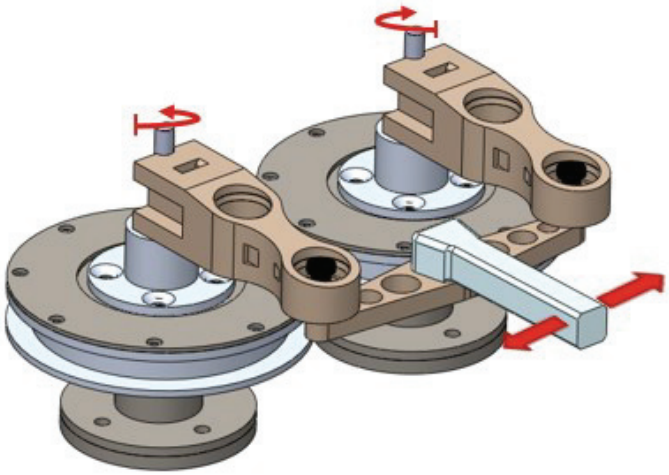

Figure 4.9. 3D model of the haptic paddle with directional MR-brake (Source: Karabulut et al., 2015).

In order to adapt final design to HIPHAD, it is required to minimize the space of the haptic paddle design. While developing the final design of MR brake, same working principle is retained. Two brakes are contained in a device in the final design to reduce input shaft number from two to one. As a result, envelope of the haptic paddle is reduced three times with the final design. As shown in Figure 4.10, MR brake final design can be replaced by the encoder on HIPHAD and it can be used with DC motor as a hybrid actuation system.

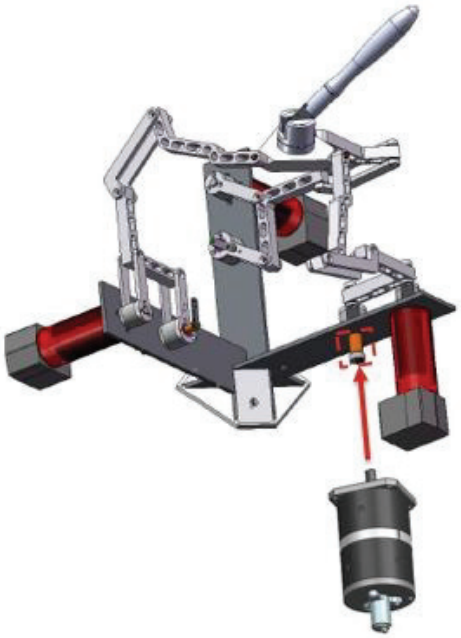

Figure 4.10. MR brake assembly on HIPHAD.

In the final MR-brake design, one-way bearing is situated between the shaft and the rotary part to transfer the motion of the shaft in one direction (Figure 4.11.). Because of the single-directional coupling feature, the motion in the reverse direction is not transferred from the shaft to the rotary part. Rotary cylinders are fixed to the rotary part with the set screws.

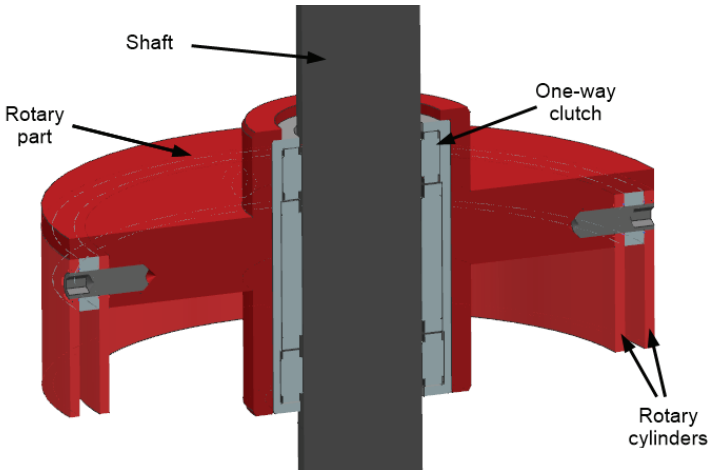

Figure 4.11. 3D assembly model of the rotary part and the shaft with one-way bearing.

As seen in Figure 4.8., there are two rotary parts in the MR-brake, namely each MR-brake module has a rotary part fastened to the shaft with one-way bearing positioned opposite to each other. For clockwise braking, upper rotary part is coupled to the shaft and for the counter-clockwise braking, bottom rotary part is coupled to the shaft. In other words, for each direction, only one rotary part rotates. That specifies the moment of inertia of the device in the free motion, which is about 54.8 kg.mm^2.

By placing one-way bearing into the MR-brake, a more compact design is obtained. This compactness gives the opportunity that, two identical brakes are coupled to each other in opposite directions to construct a bi-directional brake system.

4.3.1. Material Selection

The material selection is crucial factor in the success of MR-brake design process. Magnetic characteristic of the materials used in the MR-brake determines the magnetic flux and the performance of the MR-brake relies on the magnetic field effect on the magneto-rheological fluid. In the previous chapter, all details related to the magnetic characteristics of the common materials are given.

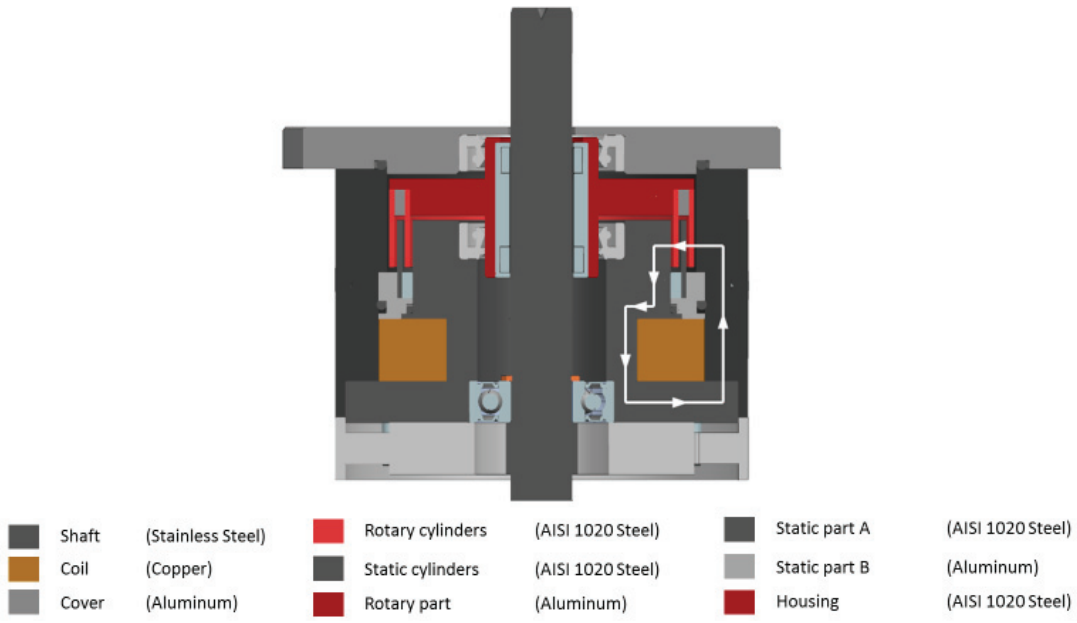

Figure 4.12. Materials used in MR-brake.

Basically, materials used in this thesis can be divided into two as magnetic and non-magnetic in terms of magnetic properties. Magnetic flux passes through the magnetic materials. To use MR-fluid effectively, magnetic flux should pass through MR-fluid in the vertical direction relative to its required shear force direction. Therefore, the path of magnetic flux should be designed by considering how the magnetic flux affects the MR-fluid. Figure 4.12. shows the magnetic flux path and the materials used in the MR-brake design. As it can be noticed in Figure 4.12., the materials on the path of magnetic flux are chosen AISI 1020 steel which is a low carbon structural steel. For the parts where the magnetic flux should not pass the material is chosen as aluminum. As mentioned in the previous chapter, the MRF-122EG is chosen as MR-fluid which has the lowest viscosity in the market. That means, MR-brake will have the minimal friction force when zero electric current is applied to the system. It is important to keep the minimum impedance as low as possible to achieve a better feeling in free motion.

4.3.2. Sealing Selection

Sealing of the MR-brake is one of the important design criteria. Since the MR-brake device contains MR-fluid, the sealing should be done properly. Otherwise, any problem with the sealing could cause a leakage problem. Between the rotary parts and the static parts, dynamic seals are used. The selection of the dynamic seals is important because the MR-fluid contains iron particles that can abrade the sealing material. To minimize the failure risk of the dynamic seals, they are kept away from the magnetic flux. For the sealing of the static parts, nitrile rubber (NBR) O-rings are used. Figure 4.13. shows the dynamic and the static seals location on the 3D model. The quality of sealing function depends on the surface finishing and the dimensioning. Therefore, the housing and the shaft of the dynamic seals are designed with necessary tolerances considering the supplier requirements (Kastas Sealing Technologies, 2017). For the groove design of static sealing, O-ring design tool from ERIKS is used (ERIKS, 2017).

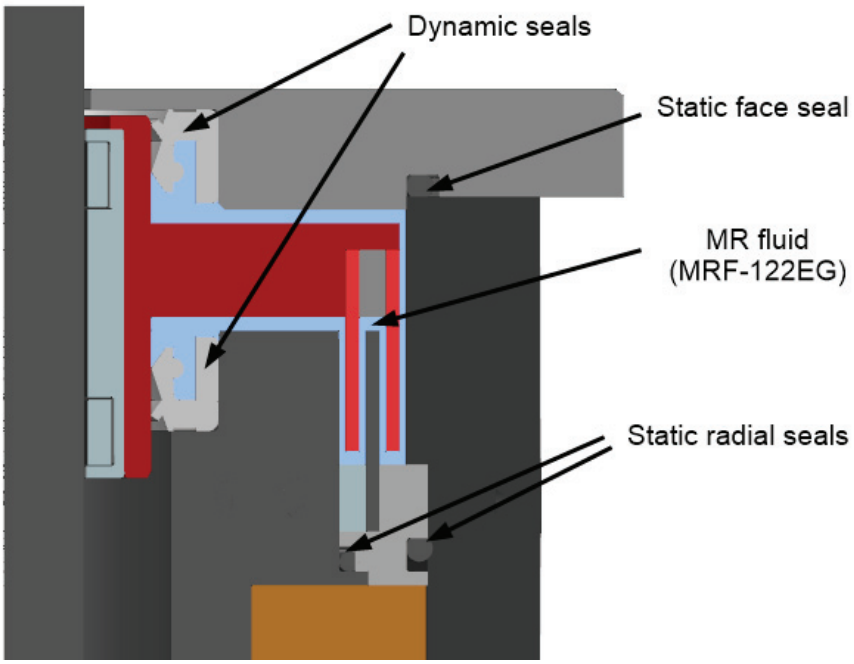

Figure 4.13. Seals used in the MR-brake design.

4.4. Design Optimization of Final Design

Using the analytical calculation and the simulation, the output torque of the 3D model of the MR-brake can be calculated. That means, the performance of the MR-brake can be evaluated during the design process. Once the practical design of MR-brake is created, the design is optimized to fulfill the requirements. Design optimization process includes two main steps as analytical calculation and magneto-static simulation. Using those steps, design volume can be minimized keeping the output torque within the requirement limits.

4.4.1. FEA Simulation

As introduced in the formula (3.9), $\tau_y(H)$ represents the magnetic field dependent yield stress. In other terms, $\tau_y(H)$ determines the MR-fluid characterization regarding to the applied magnetic flux density which depends on the applied current through the coil

wires. Using the magneto-static analysis, it is possible to simulate the magnetic flux on the 3D model. As an output of FEA simulation, we can obtain the yield stress value $\tau_y(H)$ according to 3D model, material selections and the applied electrical current.

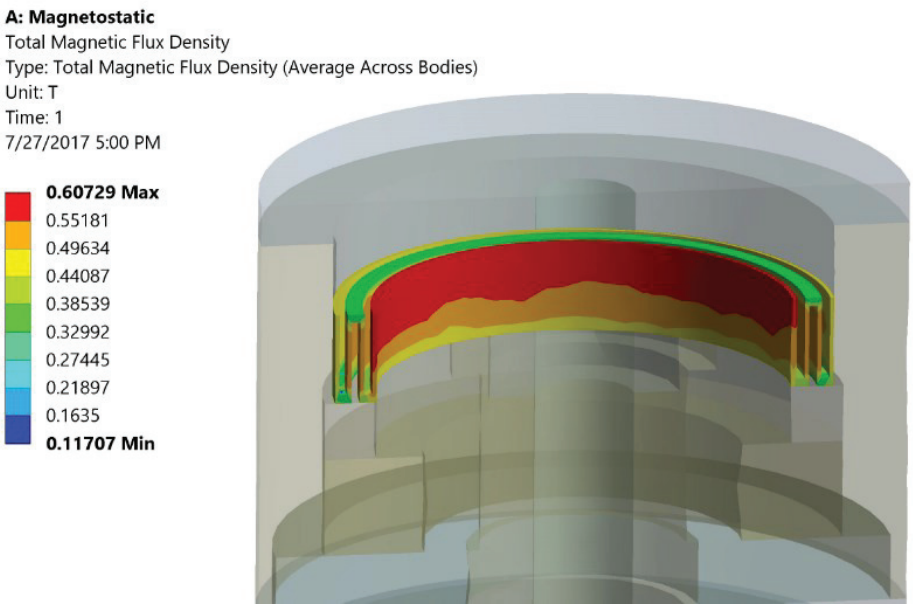

Figure 4.14. Magneto-static simulation result.

For the simulation, simplified 3D model is used ensuring that the important parameters are kept the same. The result of the magneto-static simulation is given in the Figure 4.14. that shows the magnetic flux density passing through the MR-fluid. The average result of magnetic flux density is obtained by calculating the mean value of the magnetic flux density that affects on the MR-fluid and it is found to be 0.492 T. For this simulation, 2 A continuous electrical current is applied through the 0.5 mm diameter coil wire. Using the simulation result and the B-H curve given in Figure 3.2., the magnetic field strength H can be determined. Additionally, Figure 3.3. gives the relation between the yield stress τ_y value as a function of magnetic field strength H. For 0.49 T magnetic flux, MR-fluid exhibits 25.67 kPa yield stress.

Using the initial concept design, several simulation works are performed. Some of the design parameters are varied such as; the height of the drum is changed from 5 mm to 10 mm and the coil volume was increased from 60 mm^2 to 144 mm^2 to increase the magnetic flux density, and consequently achieve high torque ratio.

4.4.2. Mathematical Model

The output torque T_D of the MR-brake can be calculated by modeling the MR-fluid behavior with the Bingham plastic model. The derivation of the formula (3.9) used for drum type MR-brakes is explained in detail in the previous chapter. Here, this formula is modified to be used in multi-drum MR-brakes.

$$T_D \approx 2h\pi\tau_y(H)\sum_{k=0}^{n} R_n^2 \tag{4.4}$$

where h is the height of the cylindrical disc, and τ_y is the magnetic field H dependent yield stress. Additionally, R_n represents the outer radius of the cylinders from the rotational axis, n is the number of the cylinder and it is calculated as follows;

$$R_n = R_{n-1} + d + g \tag{4.5}$$

where d is the thickness of the cylinders and g is the MR-fluid gap thickness.

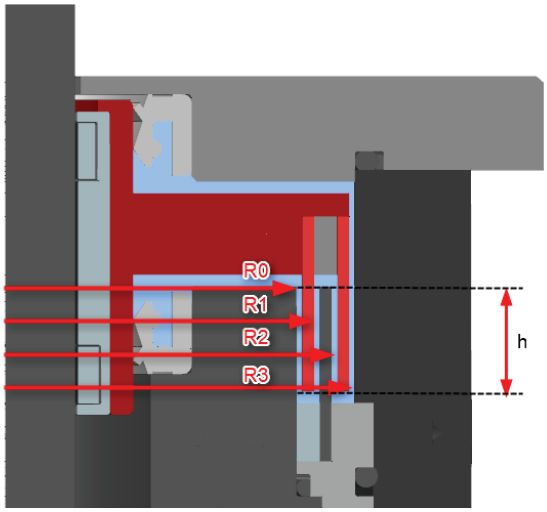

Figure 4.15. Parameters related with the torque calculation.

The parameters related to the radius and the height of the cylinders are defined in Figure 4.15.. In the final design, R_0 equals to 25 mm, h is 9 mm, d is 1 mm and g is 0,5 mm. As the dimensioning parameters used in (4.4) and the yield stress value $\tau_y(H)$ calculated with FEA simulation are known, the output torque is calculated as 4.33 Nm.

4.5. Conclusion

In this chapter, the design process of the MR-brake is explained in detail. As a first step, the requirements are determined according to the place of use, HIPHAD v2.0, which is a new version of HIPHAD. Since the design is developed for a haptic application, the multi-directional brake feature becomes essential to overcome the sticking problem. Besides that, the moment of inertia is kept minimal to lower the minimum impedance which defines the quality of the free motion in haptic applications. Since the damping force can be varied with this design, the developed MR-brake will enlarge the Z-width of the HIPHAD when it is used in its next version.

Table 4.7. Product specifications of proposed 3D model

Product Weight	**Moment of Inertia**	**Rated Torque**	**Maximum Operational Current**
3.5 kg	54.8 kg.mm^2	4.33 Nm	2 A

The product specifications of the final design are given in the Table 4.7. The rated torque calculated as 4.33 Nm which is 1.4 times bigger than the torque values specified in the requirements. The final 3D model of the MR-brake has 80 mm diameter cylinder shape housing and total length of the MR-brake is 124 mm.

The outcomes from the 3D modeling and the design optimization are evaluated with the experimental tests on the prototype model. The simulation results are compared and the final product that will be used in haptic applications is characterized. These studies are presented in the next chapter.

CHAPTER 5

EXPERIMENTAL VALIDATION

In the previous chapter, two directional drum type MR-brake design is introduced. The performance of the MR-brake is determined with the FEA simulation and analytical calculations. During the design process, the proposed MR-brake design is developed as the requirements are fulfilled.

The prototype of the final MR-brake design is manufactured. The prototype of the MR-brake is experimentally tested to validate its performance. The MR-brake is characterized by obtaining the current-torque relation that identifies the range of the MR-brake torque. Besides that, some of the design concerns are investigated such as the response time and the performance of the bi-directional brake function.

MR-brake system includes two brakes which are controlled separately and each of them constrains the motion in one direction. Experimental test are performed for each of the brakes and the test results are given as first and second MR-brake. Figure 5.1 demonstrates the direction of the braking torque regarding the active brake.

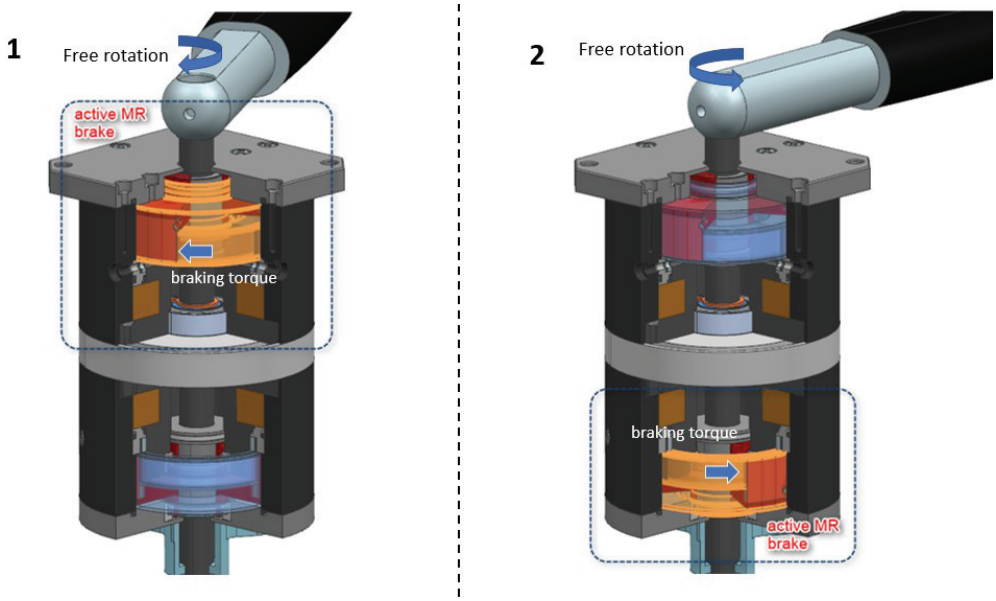

Figure 5.1. Braking torque direction with respect to first and second MR-brake activation.

5.1. MR-Brake Prototype

MR-brake design is developed from concept to final design considering the requirements that are specified related to the targeted area of usage. The model of the MR-brake is revised to ease the manufacturing process and the final 3D model before the manufacturing is shown in Figure 5.2.. Sketch drawings for the manufacturing are prepared and especially for the tolerances of bearing and sealing surfaces, design and safety guidelines are followed. The performance and the durability of the seals and the bearings depend on the quality of the surface quality and the tolerances. For instance, the permissible torque of the one-way bearing decreases from 12.2 Nm to 6.1 Nm when the N7 tolerances are used instead of N6 for the housing surface (Schaeffler Technologies, 2017). Generally, clearance fit tolerances are used for the related parts and $\pm$ 0.1 mm is applied as a general tolerance for the rest.

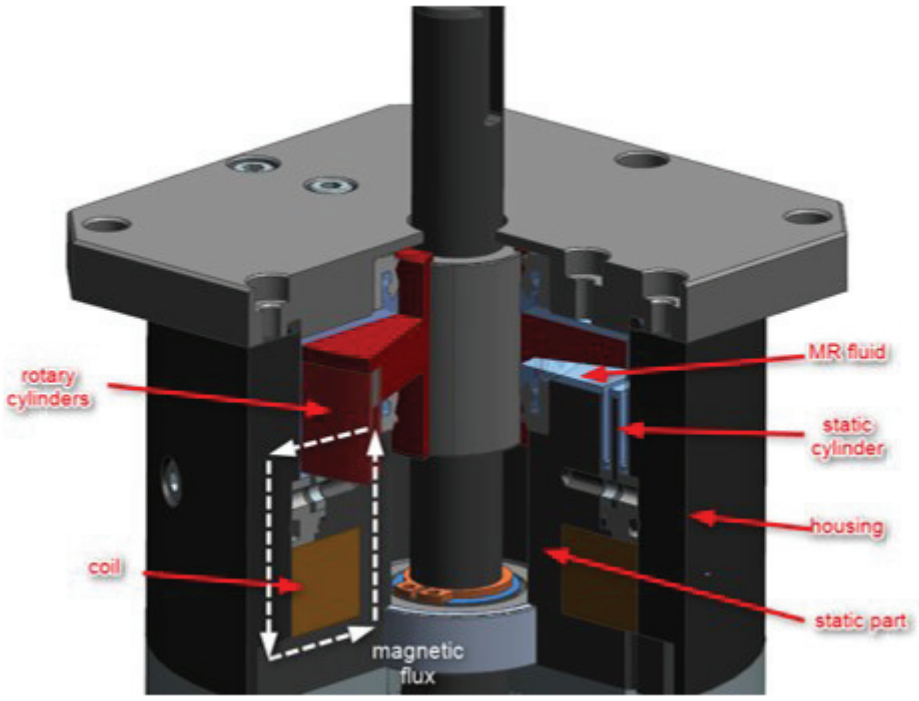

Figure 5.2. The final CAD model of the MR-brake.

Standard off-the-shelf components are used for simplicity of the product, e.g. M3 size bolts and screws are used the all assembly connections. M3 type set screws are used for the assembly of the rotary cylinders that consist of two rotary drums, spacer and rotary part that is also the housing for the one-way bearing. Static cylinders are mounted to the housing with M3 bolts. LOCTITE thread sealant and sealing strip are used to provide seal for those bolts since they interact with the MR-fluid.

The literature survey showed that the material selections play crucial roles on the magnetic field strength, namely the viscous characteristic of the MR-brake. The path of the magnetic flux is determined by choosing the magnetic material. For the parts where magnetic flux should flow through, AISI 1008 steel which is a low carbon steel, also called soft ferro-magnetic material, is used. Advantages of using the soft ferro-magnetic material is that they have narrow hysteresis loops and low carbon steels are suitable for the machining operations. SAE 304 stainless steel is used for the shaft and aluminum alloy material is utilized for the non-magnetic parts.

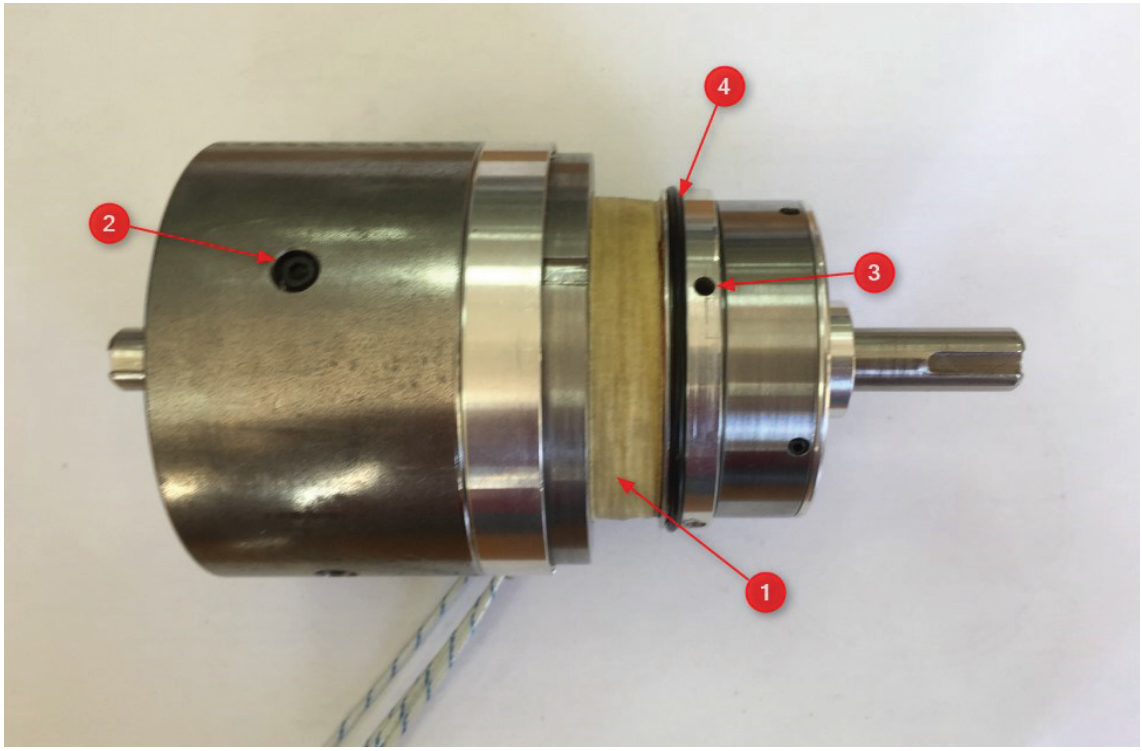

Figure 5.3. The assemble of the MR-brake prototype.

Manufactured and assembled prototype is shown in Figure 5.3.. As a coil, 0.5 mm diameter copper wire is used (1). During the assembly, it is observed that the drilled holes on the curved surfaces (2 and 3) do not match properly since the screw hole sizes are determined for close fits to avoid leakage. Rotary shaft seals are chosen to provide seal between the dynamic part connections. O-rings (4) are used for the sealing of static part connections. After the all parts are mounted, the MR-fluid is filled through the screw hole on the covers to the both side. Two of them being on top cover and three of them being on the bottom cover, a total five screw holes are drilled to fill the MR-fluid while removing the air. The most challenging part of the assembly of the prototype was the filling the MR-fluid. To fill the MR-fluid, the air inside the gap should be removed with negative pressure. After completing the assembly of MR-brake prototype, it is seen that there is no leakage problem. Another observation regarding the assembly of the prototype is that the usage of the rotary shaft seals increases the off-state torque because of the friction between the seals and the rotary part.

5.2. Experimental Test Setup Verification

Experimental tests are performed at relatively low speed. During the experimental tests, DC motor is controlled in voltage mode and it is ensured that the torque generated by the DC motor exceeds the torque rate of the MR-brake prototype. Investigating the frequency response and the transfer function of the DC motor, it is proven that the experimental tests are not affected by the performance of the DC motor, since its bandwidth of operation is much higher than MR brake.

Frequency response of the DC motor is estimated by using sinusoidal voltage signals as input and resulting velocity as output. Data which is used for transfer function estimation is collected when the frequency of the sinusoidal input voltage is 1 rad/s. Velocity output signal is obtained by taking derivative of the position signal from quadrature encoder. In order to achieve a smooth velocity signal, raw signal is fitted to linear mathematical model with 95% confidence bounds. Then filtered signal is used as input signal and the voltage signal is used for output signal for the transfer function estimation. The estimation is fit to actual data with 99.13% of accuracy.

As it can be seen in (5.1) that DC motor has closed-loop second order transfer function with two poles. The corner frequency occurs at 202 rad/s. According to the frequency response result, the bandwidth of the DC motor is sufficient for the MR-brake validation test.

$$\frac{10.35}{2\,10^{-5}\,s^2 + 0.000368\,s + 1} \tag{5.1}$$

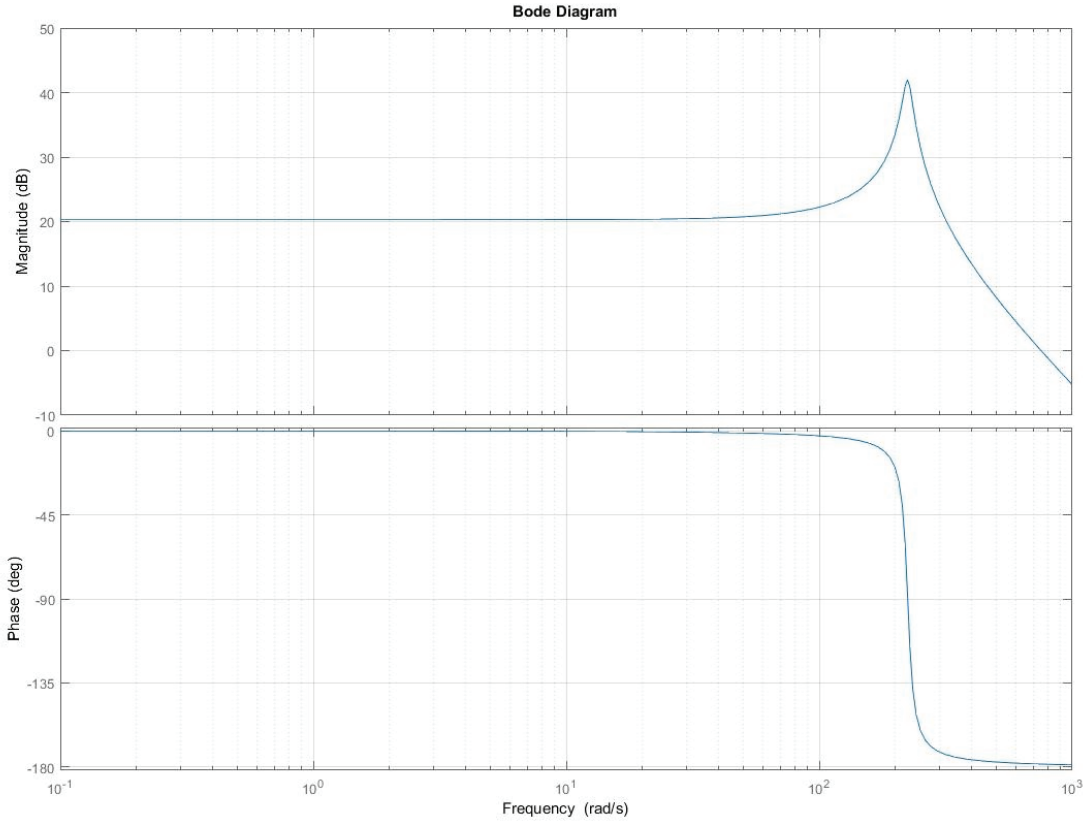

Figure 5.4. Bode diagram of voltage-to-velocity transfer function of DC motor.

5.3. Test Results

The performance of the MR-brake is validated by performing series of experimental tests consisting of characterization and frequency domain tests to find its operational bandwidth. The details of the test rig and the equipment are given in the test methodology section. Test rig consists of a rotary torque sensor, prototype of MR-brake and a geared DC motor which has 1:100 reduction ratio with belt and pulley with 1:6 reduction ratio. In order to define the characteristic of the MR-brake, current-torque relation and bode-plot diagram of the system are obtained.

During the measurements, DC motor is driven with a steady and slow velocity using LSC 30/2 series Servo amplifier from Maxon motor and current signal is controlled with Linear current amplifier module of Quanser that has a feature of measuring applied current with a high range of bandwidth (10 kHz for current mode). The torque difference between DC motor torque and the braking torque, which is equal to MR-brake torque, is measured with TRS300 series shaft-to-shaft rotary torque sensor from FUTEK at 1 kS/s sampling rate.

5.3.1. Characterization

For the characterization, repeated sequence of current signal is applied to the MR-brake to determine the torque response. The current signal of the MR-brake is increased with steps of 1 mA starting from 0 A each 10 ms until it reaches its maximum range at 2 A, and then it is decreased from 2 A following the same pattern to 0 A. To provide a consistent result, after 5 seconds delay for the stabilization of the MR-brake from hysteresis effects, this sequence is repeated for ten times.

Figure 5.5 shows the input current signal and the response torque measurement for both brakes. The current input and torque response data are used for the characterization of the MR-brake.

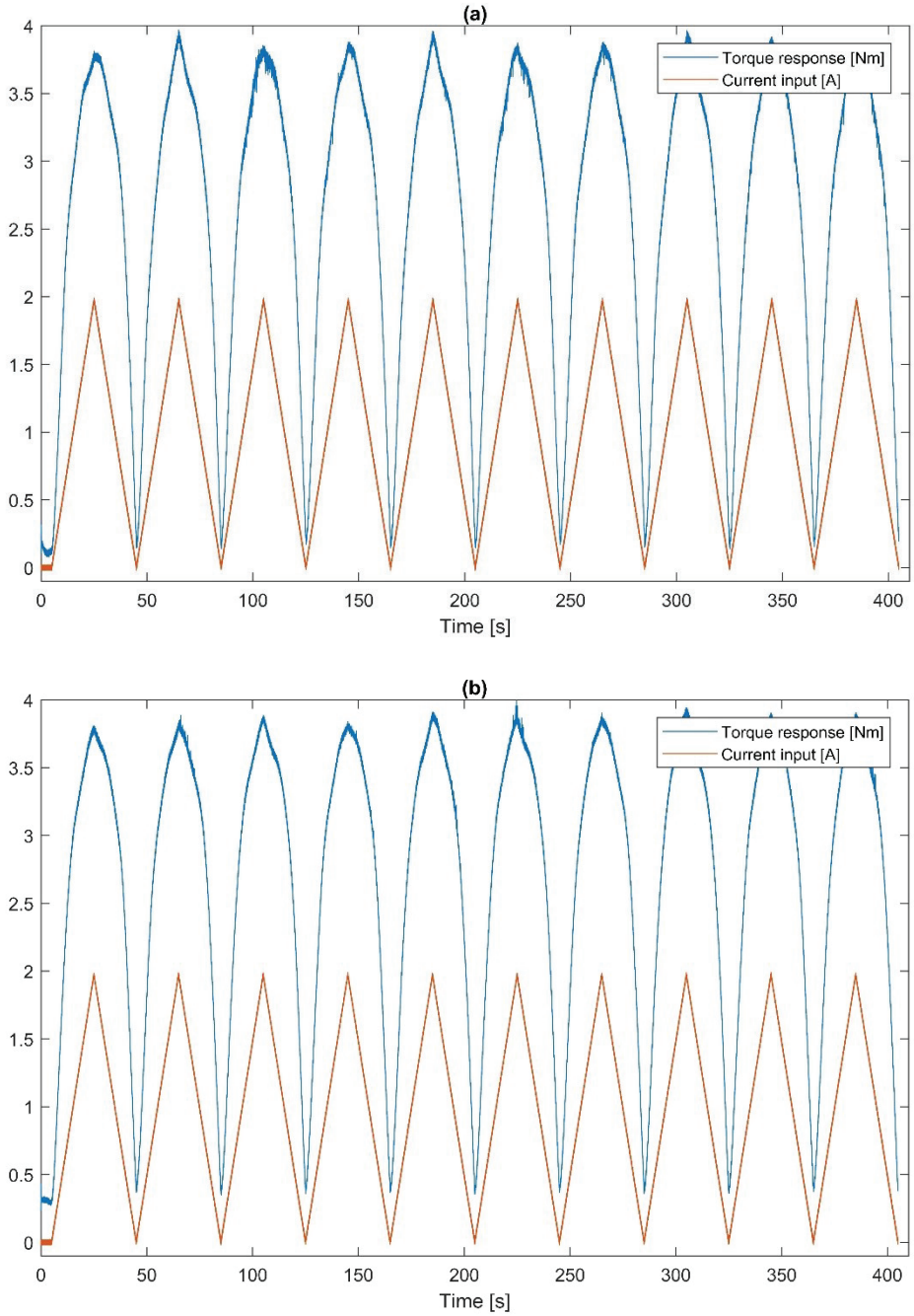

Figure 5.5. Current and torque signals for (a) first MR brake and (b) second MR brake.

During the characterization work, torque signal is measured as a response to the applied current signal. The reason of using repeating sequence signal as an input current signal is to achieve a mean torque signal for deriving current-torque relation. The hysteresis loop can be seen from the current-torque relation in Figure 5.6.. Quintic polynomial curves are fitted to raw torque signal for rising and falling direction in order to model the torque response of the system. This model is used to control the MR-brake device in frequency test.

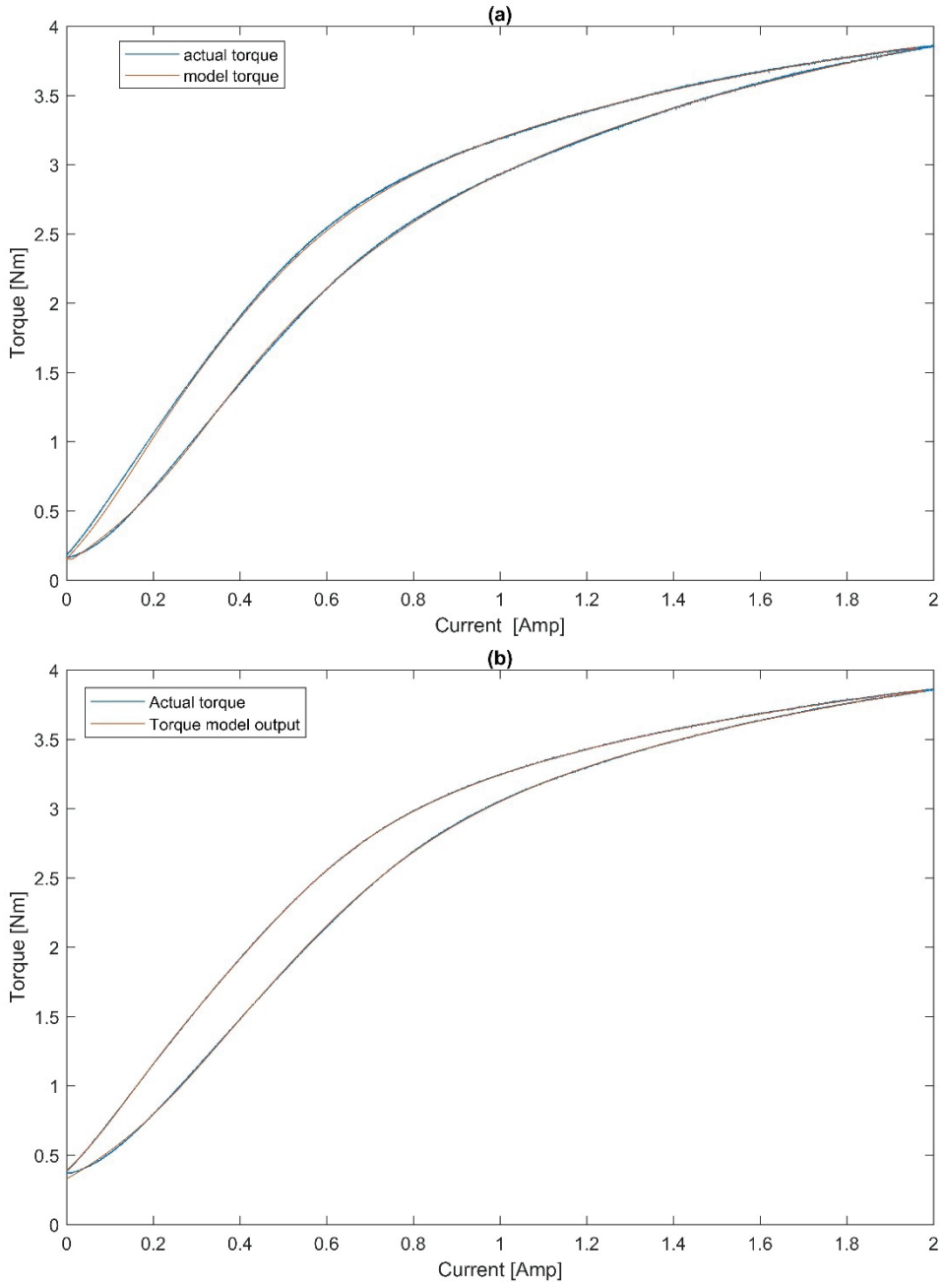

Figure 5.6. Torque-current relation of (a) first MR brake and (b) second MR brake.

The minimum measured braking torque is 0.15 Nm at 0 A, and the maximum measured torque reaches 3.84 Nm at 2 A. The experimental results are consistent with the predicted torque which is calculated by the FEA simulation and the mathematical model with almost 90 % of confidence. However, the results indicate that both MR-brakes could not reach the predicted maximum torque level due to remaining air inside the MR-fluid gap. It can be discussed that if MR-fluid gap were completely filled, then the prototype could have reached the simulated torque range.

5.3.2. Frequency Response

The frequency response of the system is defined as the steady-stade response of the system to a sinusoidal input signal. Since the system has a non-linear characteristic, the current signal is tuned, so that the resulting torque signal becomes sinusoidal signal at steady state. Thus, the desired torque response is used for input signal T_i and actual response of the system is measured by torque sensor and used as output signal T_o for the frequency response calculation. The Matlab sub-model used for current signal generation for sinusoidal torque response as shown in Figure 5.7.. Sine wave up and down blocks generates sinusoidal torque input within the range of applicable torque. In MATLAB functions, there is a quintic polynomial model that use sine wave torque signal as input and in return outputs the calculated current signal. By using derivative of sine wave signal with a swicth block, the MATLAB Functions are chosen for rising and falling direction consistent with the modeled hysteresis effect.

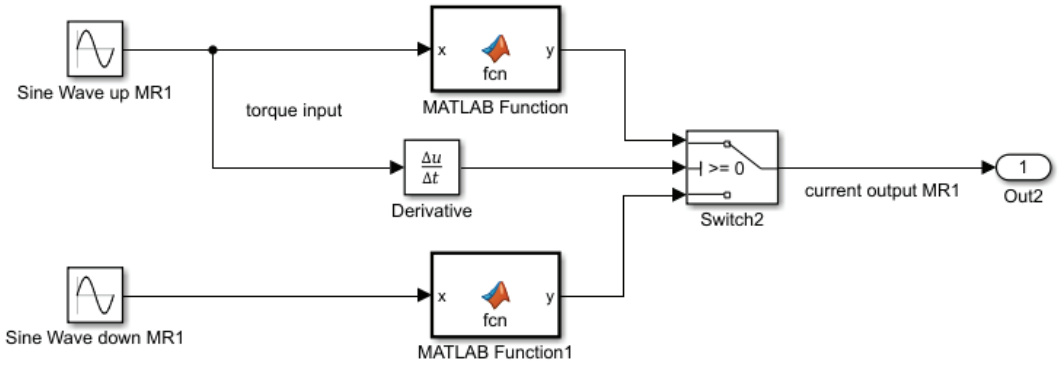

Figure 5.7. Sub-model of the current signal generation for sinusoidal torque output.

In Figure 5.8., desired sinusoidal torque signal and the measured torque signal are compared at 0.1 rad/s frequency. In order to find the percentage of difference between two signals, root-mean square error (RMSE) is used as the given below:

$$RMSE = \sqrt{\frac{\sum_{i=1}^{n}[T_d(i) - T_m(i)]^2}{n}} \tag{5.2}$$

Where T_d and T_m represents the desired torque and the measured torque signal, and n is the total number of samples collected at 1 kHz sampling rate of the signal. According to the result of RMSE, the difference between desired and actual torque signal is 3,54 % for the first MR brake and 3,07 % for the second MR brake (Figure 5.8).

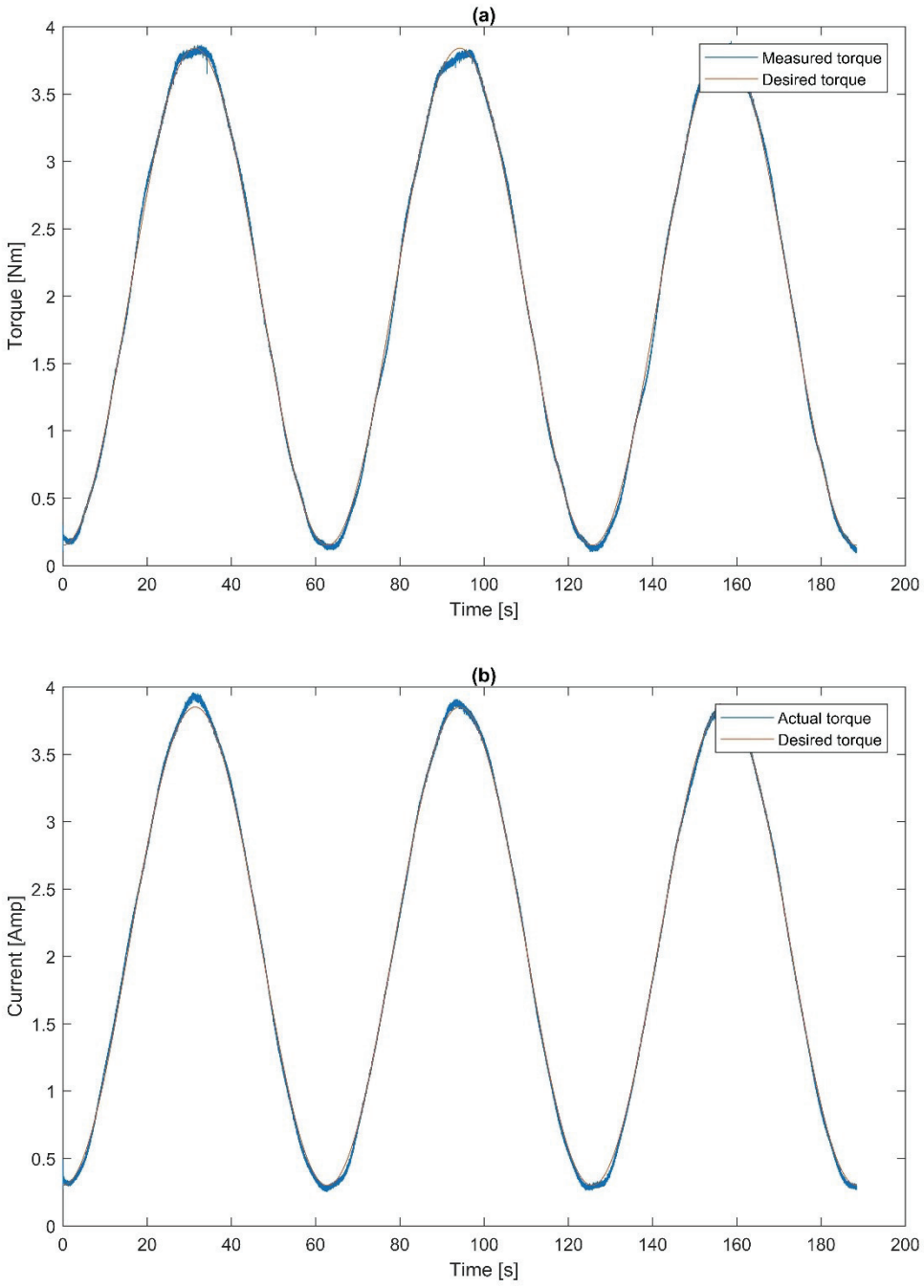

Figure 5.8. Sinusoidal torque input and output torque of (a) first MR brake and (b) second MR brake.

The magnitude ratio of the system $G(\omega)$ is described as:

$$G(\omega) = \frac{T_o}{T_i} \tag{5.3}$$

The logarithmic gain of the system is expressed in terms of logarithm to the base 10 with the following equation:

$$\text{Logaritmic gain} = 20 \log_{10}|G(\omega)| \tag{5.4}$$

Frequency tests are performed for the frequency range between 0.1 to 1000 rad/s with 10 sample points taken within each decade. The logaritmic gain in dB and the phase of the MR-brake system are shown in Figure 5.9. and Figure 5.10.

Experimentally measured logarithmic gain and the phase diagrams are transferred to frequency-response model (idfrd) and then it is estimated by using System Identification Toolbox™ in MATLAB® software. Estimation data fits 75.91% with the experimental data and mean square error equals to 0.013 for the first MR-brake. The transfer function of the estimated model is as follows:

$$\frac{1}{1.791\ 10^{-5}\ s^2 + 0.01702\ s + 1} \tag{5.5}$$

Logarithmic gain and phase plot of the estimated transfer function of first MR-brake are shown in Figure 5.9. which is compared with the experimental results. According to the frequency response of estimated transfer function, the system of first MR-brake has a second order transfer function with two real poles. First corner frequency, which defines the bandwidth of the system, occurs at 62.92 rad/s. At the first corner frequency, experimental logarithmic gain equals to -4.65 dB and the phase is -39 deg. Second corner frequency occurs at 887.23 rad/s and experimental logarithmic gain and phase are -25 dB and -250 degrees for that frequency.

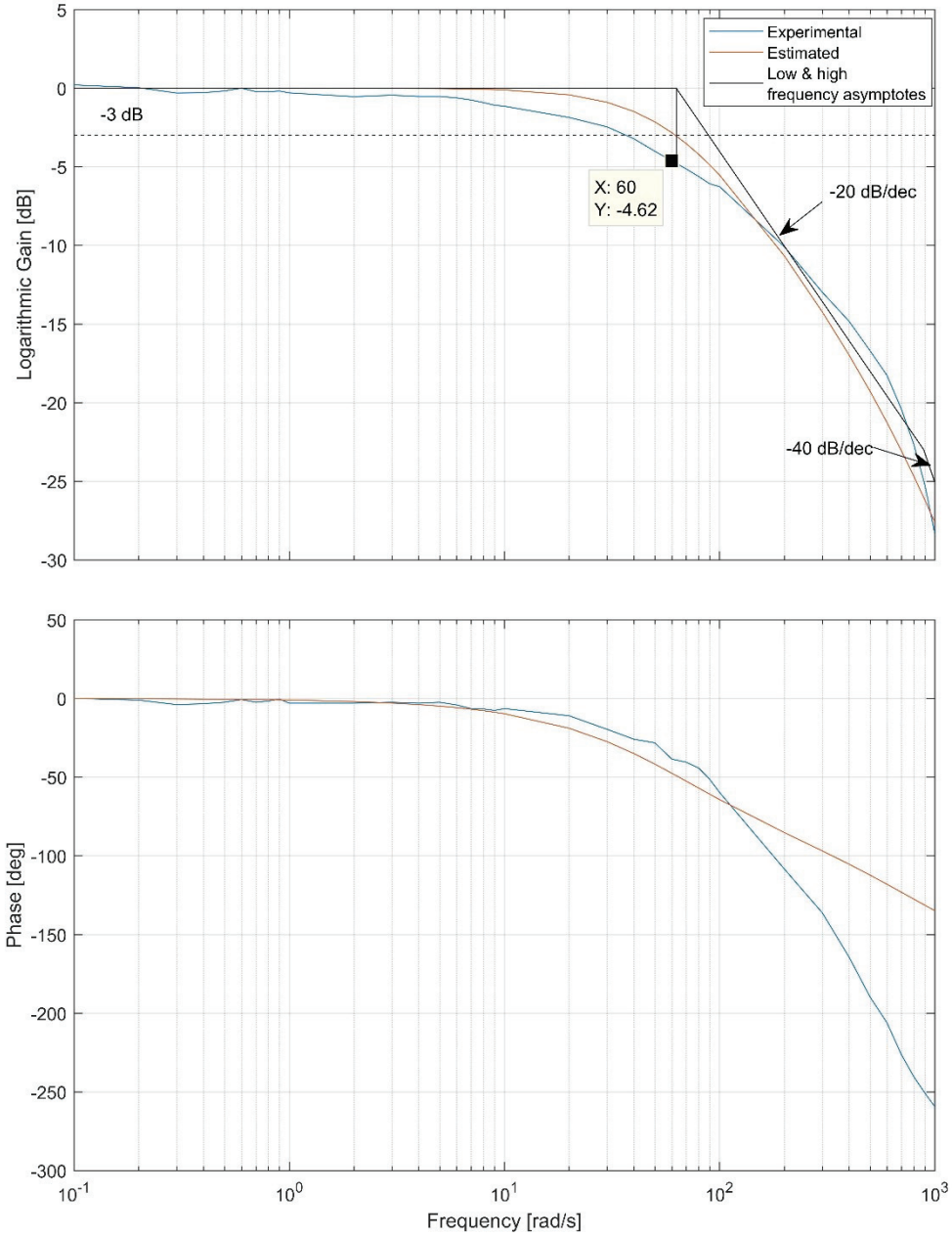

Figure 5.9. Bode diagram of the first MR-brake.

Same estimation method is used to calculate the transfer function of the second MR-brake. Estimation data fits 83.24% with the experimental data and mean square error is 0.007. The transfer function of the second MR-brake is estimated as follows:

$$\frac{0.9818}{2.309\ 10^{-5}\ s^2 + 0.01726\ s + 1} \tag{5.6}$$

Figure 5.10 shows the comparison of the logarithmic gain and phase plot between the estimated transfer function and the experimental result for the second MR-brake. Similarly to the first MR-brake, the second MR-brake has a second order transfer function with two real poles. The bandwidth of the second MR brake is 63.3 rad/s. At the first corner frequency, experimental logarithmic gain equals to -4.2 dB and the phase is -42 deg. Second corner frequency occurs at 684.4 rad/s and experimental logarithmic gain and phase are -20 dB and -215 degrees.

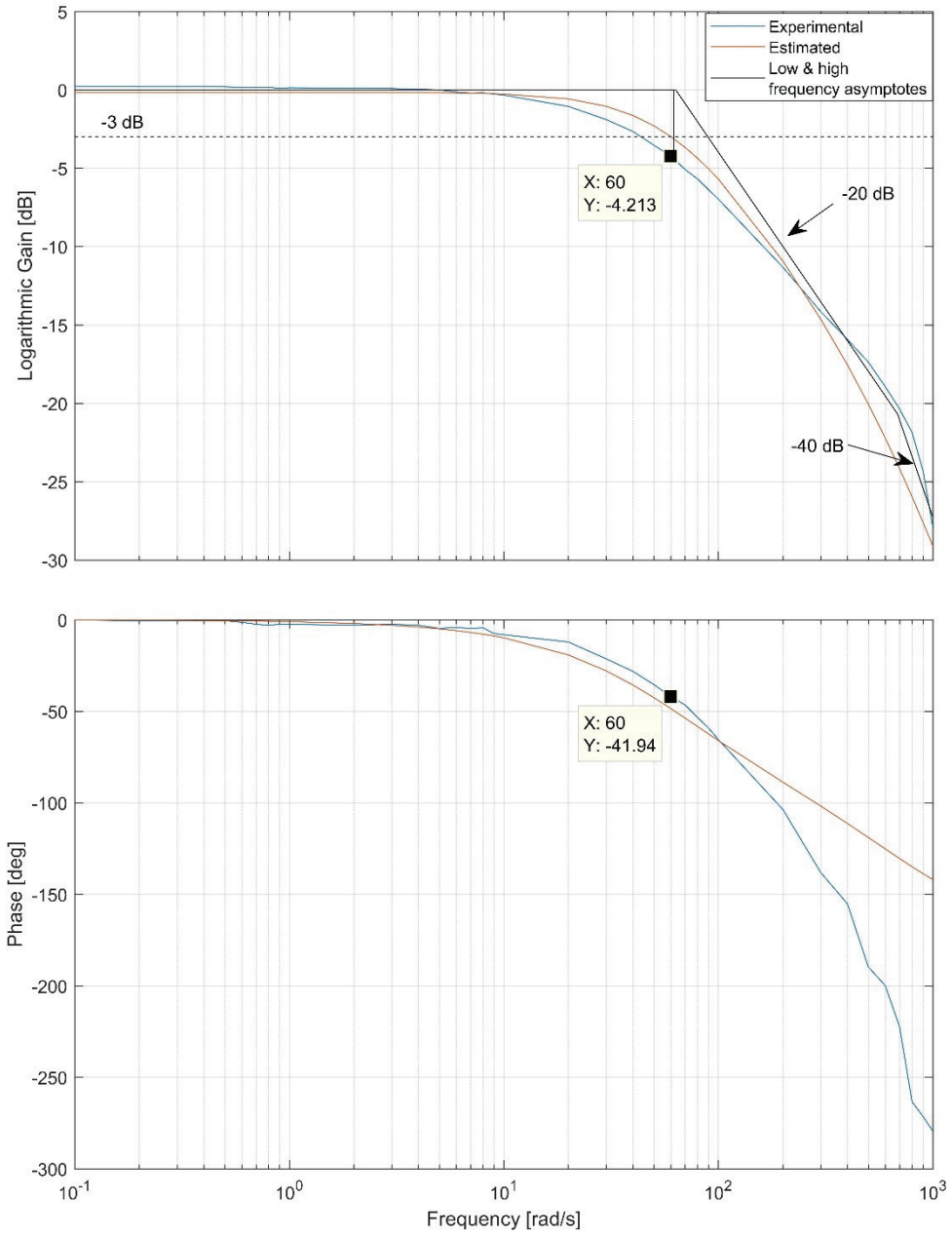

Figure 5.10. Bode diagram of the second MR-brake.

5.4. Prototype Specifications

The performance specifications such as torque rates and the bandwidth of the prototype are given by the results of experimental validation tests. In Table 5.1, the features of the prototype related to the performance and the design are presented.

Table 5.1. MR-brake prototype specifications.

Category	**Specification**
Product weight	3.570 kg
Braking torque @ 2 A	3.84 Nm
Off-state torque	0.15
Bandwidth	62 rad/s
Diameter	80 mm
Length	124 mm
Coil wire Diameter	0.5 mm
Maximum Operational Current	2 A
Number of Turns of Enameled Wire	450
Magneto-Rheological Material	MRF-122EG
Magnetic Materials	AISI 1008 Steel
Non-magnetic Materials	SAE 304 Stainless Steel and Aluminum

CHAPTER 6

CONCLUSION

A haptic device that uses MR-brake suffers from a common problem. This is called the stiction problem in the literature that occurs when the MR-brake is activated. Activation of the MR-brake restricts motion in both directions and the user feels that he/she is stuck in the virtual wall during the simulation in a haptic application. In order to solve this problem, a novel MR-brake system that consists of two MR-brakes and two one-way bearings is introduced with the design of haptic paddle as an initial study of this thesis. Building on this idea, a bidirectional drum type MR-brake is designed and optimized by using FEA simulation and mathematical model of the system. The design requirements are specified to use the system in a haptic device. Design specifications such as disc type, disc and MR-fluid gap thickness, coil positioning, and material selections are investigated in terms of torque-current performance. For this purpose, mathematical model of the MR-brake is derived from the Bingham plastic model, using this model, the output torque can be calculated based on the magnetic flux density. Magnetic flux density is simulated by using Magneto-static package of the ANSYS software. As a result of this simulation, the relation between the input current and the magnetic field density is obtained. Using this model, a design optimization method is introduced and used to develop initial multi-disc MR-brake design. An optimization method is employed to achieve high output torque within a compact volume. Finally, a prototype of the bidirectional MR-brake is manufactured and assembled.

The MR-brake performance is validated with an experimental test setup. The constructed test rig mainly consists of an MR-brake, a torque sensor and a DC motor. Periodic input signal is used to reveal the relation between current input and torque response. Then quantic polynomial curve is fitted to the experimental data to model the hysteresis behavior of the system response. The hysteresis model fits to experimental data with 95% of accuracy. Using this hysteresis model, current input signal is shaped to have a sinusoidal torque signal in return. In the frequency response of the system the magnitude ratio is calculated by comparing the torque output measured from the torque sensor to torque demand. Frequency tests are performed within the range of 0.1 rad/s to

1000 rad/s using 37 different frequencies in between (see test results in Appendix C). Transfer function of the system is estimated after obtaining the experimental logarithmic gain and phase plots of the system. The estimation fits to experimental Bode diagram with 75% accuracy ratio.

Experimental results show that braking torque of prototype reaches 3.84 Nm (13 times higher than the actuator used in the first generation of HIPHAD) at maximum current rate and 0.15 Nm at minimum current rate. The result verifies the simulation predictions with 90% accuracy. The bandwidth of the system is measured to be at 63 rad/s.

6.1. Future Works

In this thesis work, the targeted output torque is chosen higher than requirements to verify the design methods and the simulation clearly. The final design of the MR-brake produces 3.8 Nm with 80 mm diameter and 124 mm length and the weight of the device is 3.57 kg. Decreasing the targeted torque range to 1 Nm which is sufficient for HIPHAD, it is possible to achieve more compact MR-brake design.

One of the reasons that this MR-brake prototype did not reach its full performance is the air that is stuck inside the MR-fluid gap. It turns out that drilling two holes on the cover, as one for filling and one for air outlet, is not sufficient for filling the MR-fluid properly. In the future studies, a new design should target that MR-fluid can be filled completely without leaving air gap inside.

During the design process, the performance of the system is predicted with FEA simulation and analytical model. When the experimental performance result is compared with the predicted performance, it is seen that the actual performance is estimated with 76% accuracy. After the relation between current and the magnetic flux response is simulated, the braking response can be mathematically modeled by fitting polynomial curve to the data obtained from FEA simulation. This relation depends on the 3D design and the magnetic characteristic of materials used in design. Since the B-H curve for MR-fluid and the AISI 1008 steel are non-linear, the FEA simulation becomes more complex. When the relation between the current and magnetic field response is mathematically modelled and used with the analytical model which gives the relation between magnetic

flux density and the brake torque, the performance of the system can be predicted with a higher accuracy. If the parameters of the design process can be separated from each other, the design optimization process can be shortened in the future studies.

Characterization of the MR-brake allows us to model hysteresis behavior of the brake. Using this model, current input is modified so that the hysteresis effect on the torque output is minimized, which is 97% fit to the actual torque output. However, this model is only effective when the desired torque is chosen as characterized torque values, which are minimum and maximum torques. In order to characterize hysteresis behavior of the MR-brake for all torque values within the limits, a new model can be studied.

It is also beneficial to study to performance drop of MR brake in extended usage and also measure the heat it produces over long-term use.

REFERENCES

Adams, R. J., & Hannaford, B. (1999). Stable haptic interaction with virtual environments. *Robotics and Automation, IEEE Transactions on, 15*(3), 465-474.

An, J., & Kwon, D.-S. (2004). *In haptics, the influence of the controllable physical damping on stability and performance.* Paper presented at the Intelligent Robots and Systems, 2004.(IROS 2004). Proceedings. 2004 IEEE/RSJ International Conference on.

An, J., & Kwon, D.-S. (2008). Five-bar linkage haptic device with DC motors and MR brakes. *Journal of Intelligent Material Systems and Structures*.

Bar-Cohen, Y., Mavroidis, C., Bouzit, M., Dolgin, B. P., Harm, D. L., Kopchok, G. E., & White, R. A. (2001). *Virtual reality robotic telesurgery simulations using MEMICA haptic system.* Paper presented at the SPIE's 8th Annual International Symposium on Smart Structures and Materials.

Basdogan, C., De, S., Kim, J., Muniyandi, M., Kim, H., & Srinivasan, M. A. (2004). Haptics in minimally invasive surgical simulation and training. *Computer Graphics and Applications, IEEE, 24*(2), 56-64.

Bedem, v. d. L. (2010). *Realization of a demonstrator slave for robotic minimally invasive surgery.* Technische Universiteit Eindhoven.

Bilgincan, T., Gezgin, E., & Dede, M. (2010). *Integration of the hybrid-structure haptic interface: HIPHAD v1. 0.* Paper presented at the Proceedings of the International Symposium of Mechanism and Machine Theory.

Bouzit, M., Burdea, G., Popescu, G., & Boian, R. (2002). The Rutgers Master II-new design force-feedback glove. *IEEE/ASME Transactions on Mechatronics, 7*(2), 256-263. doi:10.1109/TMECH.2002.1011262

Bwigroup. (2016). MAGNERIDE CONTROLLED SUSPENSION SYSTEM. Retrieved from http://www.bwigroup.com/en/pshow.php?pid=22

Carlson, J. D. (2006). *MR fluid technology-commercial status in 2006.* Paper presented at the Proceedings of the 10th International Conference on ER Fluids and MR Suspensions, 2006.

Chapuis, D., Gassert, R., Burdet, E., & Bleuler, H. (2006, Oct. 2006). *Hybrid Ultrasonic Motor and Electrorheological Clutch System for MR-Compatible Haptic Rendering.* Paper presented at the 2006 IEEE/RSJ International Conference on Intelligent Robots and Systems.

Chapuis, D., Michel, X., Gassert, R., Chew, C. M., Burdet, E., & Bleuler, H. (2007, 22-24 March 2007). *A Haptic Knob with a Hybrid Ultrasonic Motor and Powder Clutch Actuator.* Paper presented at the Second Joint EuroHaptics Conference and Symposium on Haptic Interfaces for Virtual Environment and Teleoperator Systems (WHC'07).

Colgate, J. E., & Brown, J. M. (1994). *Factors affecting the z-width of a haptic display.* Paper presented at the Robotics and Automation, 1994. Proceedings., 1994 IEEE International Conference on.

ERIKS. (2017). ERIKS O-Ring Calculator. Retrieved from https://oringcalculator.eriksgroup.com/

Flueckiger, M., Bullo, M., Chapuis, D., Gassert, R., & Perriard, Y. (2005). *fMRI compatible haptic interface actuated with traveling wave ultrasonic motor.* Paper

presented at the Industry Applications Conference, 2005. Fourtieth IAS Annual Meeting. Conference Record of the 2005.

Force Dimension. (2016). omega.3. Retrieved from http://www.forcedimension.com/products/omega-3/overview

Furusho, J., & Sakaguchi, M. (1999). New actuators using ER fluid and their applications to force display devices in virtual reality and medical treatments. *International Journal of Modern Physics B, 13*(14n16), 2151-2159.

FUTEK. (2017). TRS300 Shaft to Shaft Rotary Torque Sensor: FSH01987. Retrieved from http://www.futek.com/product.aspx?stock=FSH01987

Geomagic. (2016). Geomagic Touch (formerly Geomagic Phantom Omni) Overview. Retrieved from http://www.geomagic.com/en/products/phantom-omni/overview

Giraud, F., Amberg, M., & Lemaire-Semail, B. (2010). *Control of a haptic interface actuated by ultrasonic motors.* Paper presented at the Power Electronics and Motion Control Conference (EPE/PEMC), 2010 14th International.

Gosline, A. H., Campion, G., & Hayward, V. (2006). *On the use of eddy current brakes as tunable, fast turn-on viscous dampers for haptic rendering.* Paper presented at the Proceedings of Eurohaptics.

Han, Y.-M., Kang, P.-S., Sung, K.-G., & Choi, S.-B. (2007). Force feedback control of a medical haptic master using an electrorheological fluid. *Journal of Intelligent Material Systems and Structures, 18*(12), 1149-1154.

Hannaford, B., & Okamura, A. M. (2008). Haptics *Springer Handbook of Robotics* (pp. 719-739): Springer.

Harris Robotic Systems. (2016). RedHawk MPR. Retrieved from http://govcomm.harris.com/solutions/robotics/roboticsystems.aspx

Hayward, V., & Cruz-Hernandez, M. (2000). *Tactile display device using distributed lateral skin stretch.* Paper presented at the Proceedings of the haptic interfaces for virtual environment and teleoperator systems symposium.

Ino, S., Shimizu, S., Odagawa, T., Sato, M., Takahashi, M., Izumi, T., & Ifukube, T. (1993, 3-5 Nov 1993). *A tactile display for presenting quality of materials by changing the temperature of skin surface.* Paper presented at the Robot and Human Communication, 1993. Proceedings., 2nd IEEE International Workshop on.

Intuitive Surgical. (2016). da Vinci Surgical System. Retrieved from http://www.intuitivesurgical.com/products/davinci_surgical_system/

Jinung, A., & Dong-Soo, K. (2004, 28 Sept.-2 Oct. 2004). *In haptics, the influence of the controllable physical damping on stability and performance.* Paper presented at the Intelligent Robots and Systems, 2004. (IROS 2004). Proceedings. 2004 IEEE/RSJ International Conference on.

Jolly, M. R., Bender, J. W., & Carlson, J. D. (1998). *Properties and applications of commercial magnetorheological fluids.* Paper presented at the 5th annual international symposium on smart structures and materials.

Karabulut, M., Taner, B., & Dede, M. (2015). MR Sıvısı ile Çalışan Haptik Kol Tasarımı - Design of MR-fluid based Haptic Paddle. *TOK 2015 Bildiri Kitabı*, 867-872.

Kastas Sealing Technologies. (2017). Sistem Toleransları ve Tasarımları - Kastaş Sızdırmazlık Teknolojileri A.Ş.,.

Kern, T. A. (2009). *Engineering haptic devices: a beginner's guide for engineers*: Springer Science & Business Media.

Kikuchi, S., & Hamamoto, K. (2008). *HAMA device-haptic display for immersive virtual environments.* Paper presented at the Communications and Information Technologies, 2008. ISCIT 2008. International Symposium on.

Koyama, T., Takemura, K., & Maeno, T. (2003). *Development of an ultrasonic clutch for multi-fingered exoskeleton haptic device using passive force feedback for dexterous teleoperation.* Paper presented at the Intelligent Robots and Systems, 2003.(IROS 2003). Proceedings. 2003 IEEE/RSJ International Conference on.

Kwon, T.-B., & Song, J.-B. (2006). Force display using a hybrid haptic device composed of motors and brakes. *Mechatronics, 16*(5), 249-257. doi:http://dx.doi.org/10.1016/j.mechatronics.2005.12.003

Lawrence, D. (1993). Stability and transparency in bilateral teleoperation. *Robotics and Automation, IEEE Transactions on, 9*(5), 624-637.

Li, W. (2014). Design and Development of Magneto-Rheological Actuators with Application in Mobile Robotics.

Li, W., Liu, B., Kosasih, P. B., & Zhang, X. (2007). A 2-DOF MR actuator joystick for virtual reality applications. *Sensors and Actuators A: Physical, 137*(2), 308-320.

Liu, B., Li, W., Kosasih, P. B., & Zhang, X. (2006). Development of an MR-brake-based haptic device. *Smart materials and structures, 15*(6), 1960.

Liu, X., Dodds, G., McCartney, J., & Hinds, B. K. (2004). Virtual DesignWorks—designing 3D CAD models via haptic interaction. *Computer-Aided Design, 36*(12), 1129-1140. doi:http://dx.doi.org/10.1016/j.cad.2003.10.003

LORD Corp. (2016). Magneto-Rheological (MR) Fluid. Retrieved from http://www.lord.com/products-and-solutions/active-vibration-control/industrial-suspension-systems/magneto-rheological-(mr)-fluid

Melli-Huber, J., Weinberg, B., Fisch, A., Nikitczuk, J., Mavroidis, C., & Wampler, C. (2003). *Electro-rheological fluidic actuators for haptic vehicular instrument controls.* Paper presented at the Haptic Interfaces for Virtual Environment and Teleoperator Systems, 2003. HAPTICS 2003. Proceedings. 11th Symposium on.

Nara, T., Takasaki, M., Maeda, T., Higuchi, T., Ando, S., & Tachi, S. (2001, 17-17 March 2001). *Surface Acoustic Wave (SAW) tactile display based on properties of mechanoreceptors.* Paper presented at the Virtual Reality, 2001. Proceedings. IEEE.

National Instruments. (2017). PXI-6229 - National Instruments. Retrieved from http://www.ni.com/en-tr/support/model.pxi-6229.html

Nguyen, P.-B., & Choi, S.-B. (2011). A new approach to magnetic circuit analysis and its application to the optimal design of a bi-directional magnetorheological brake. *Smart Materials and Structures, 20*(12), 125003.

Novint Technologies. (2016). Novint Falcon. Retrieved from http://www.novint.com/index.php/novintfalcon

Parthiban, C., Esser, C., & Zinn, M. R. (2012). *Evaluation of a parallel actuation approach for MR-compatible haptics.* Paper presented at the Haptics Symposium (HAPTICS), 2012 IEEE.

Qi, W., & Hayward, V. (2006, 25-26 March 2006). *Compact, Portable, Modular, High-performance, Distributed Tactile Transducer Device Based on Lateral Skin Deformation.* Paper presented at the 2006 14th Symposium on Haptic Interfaces for Virtual Environment and Teleoperator Systems.

Rabinow, J. (1948). The Magnetic Fluid Clutch. *Transactions of the American Institute of Electrical Engineers, 67*(2), 1308.

Reed, M. R., & Book, W. J. (2004). *Modeling and control of an improved dissipative passive haptic display.* Paper presented at the Robotics and Automation, 2004. Proceedings. ICRA'04. 2004 IEEE International Conference on.

Rosenberg, L. B., & Adelstein, B. D. (1993). *Perceptual decomposition of virtual haptic surfaces.* Paper presented at the Virtual Reality, 1993. Proceedings., IEEE 1993 Symposium on Research Frontiers in.

Rossa, C., Lozada, J., & Micaelli, A. (2014). Design and Control of a Dual Unidirectional Brake Hybrid Actuation System for Haptic Devices. *Haptics, IEEE Transactions on, 7*(4), 442-453.

Samur, E., Flaction, L., Spaelter, U., Bleuler, H., Hellier, D., & Ourselin, S. (2008). *A haptic interface with motor/brake system for colonoscopy simulation.* Paper presented at the Haptic interfaces for virtual environment and teleoperator systems, 2008. haptics 2008. symposium on.

Schaeffler Technologies. (2017). Design and safety guidelines Drawn cup roller clutches HFL.

Senkal, D., & Gurocak, H. (2009). Spherical brake with MR fluid as multi degree of freedom actuator for haptics. *Journal of Intelligent Material Systems and Structures, 20*(18), 2149-2160.

Senkal, D., & Gurocak, H. (2011). Haptic joystick with hybrid actuator using air muscles and spherical MR-brake. *Mechatronics, 21*(6), 951-960.

Song, B.-K., Oh, J.-S., & Choi, S.-B. (2014). Design of a New 4-DOF Haptic Master Featuring Magnetorheological Fluid. *Advances in Mechanical Engineering, 6*, 843498.

Spencer, B., Dyke, S., Sain, M., & Carlson, J. (1997). Phenomenological model for magnetorheological dampers. *Journal of engineering mechanics, 123*(3), 230-238.

Taylor, P. M., Hosseini-Sianaki, A., & Varley, C. J. (1996, 22-28 Apr 1996). *An electrorheological fluid-based tactile array for virtual environments.* Paper presented at the Robotics and Automation, 1996. Proceedings., 1996 IEEE International Conference on.

Van der Linde, R. Q., Lammertse, P., Frederiksen, E., & Ruiter, B. (2002). *The HapticMaster, a new high-performance haptic interface.* Paper presented at the Proc. Eurohaptics.

Yamaguchi, Y., Furusho, J., Kimura, S., & Koyanagi, K. (2005). Development of high-performance MR actuator and its application to 2-D force display. *International Journal of Modern Physics B, 19*(07n09), 1485-1491.

Yang, T. H., Kim, S. Y., Kim, C. H., Kwon, D. S., & Book, W. J. (2009, 18-20 March 2009). *Development of a miniature pin-array tactile module using elastic and electromagnetic force for mobile devices.* Paper presented at the EuroHaptics conference, 2009 and Symposium on Haptic Interfaces for Virtual Environment and Teleoperator Systems. World Haptics 2009. Third Joint.

APPENDIX A

FUTEK TRS300 SERIES TORQUE SENSOR

A.1. Product Specifications

FUTEK's TRS300 is a shaft-to-shaft rotary torque sensor with torque measurement range ± 10 Nm and a torsional stiffness of 955 Nm/rad (Figure A.1). The TRS300 utilizes strain gauge technology and features slip-ring signal transmission allowing the sensor to operate at up to 3000 RPM. The specifications of the product are shown in the Table A.1 (FUTEK, 2017).

Figure A.1. FUTEK shaft-to-shaft torque sensor
(Source: FUTEK, 2017).

Table A.1. Product specifications of FUTEK rotary torque sensor.

SPECIFICATIONS	
PERFORMANCE	
Nonlinearity	±0.2% of RO
Hysteresis	±0.1% of RO
Nonrepeatability	±0.2% of RO
Rotational Speed	3000 Max
ELECTRICAL	
Rated Output (RO)	2 mV/V nom
Excitation (VDC or VAC)	5 to 11
Bridge Resistance	350 Ohm nom
Connection	6 pin Binder Series #581 (09-0323-99-06)
MECHANICAL	
Safe Overload	150% of RO
Material	Aluminum 6061 (Housing) Steel Alloy (Shaft)
IP Rating	IP40
TEMPERATURE	
Operating Temperature	14 to 194°F (–10 to 90°C)
Compensated Temperature	41 to 122°F (5 to 50°C)
Temperature Shift Zero	±0.01% of RO/°F (±0.02% of RO/°C)
Temperature Shift Span	±0.01% of RO/°F (±0.02% of RO/°C)
CALIBRATION	
Calibration Test Excitation	10 VDC
Calibration (standard)	Certificate of Conformance
Calibration (available)	5-pt CW & CCW
Shunt Calibration Value	With sensor fully connected jump pins 1 & 6 to generate 2 mV/V nom output

A.2. CSG110 Strain Gauge Amplifier

CSG110 Strain Gauge Amplifier is used besides torque sensor to convert 2 mv/V signal output to ± 10V analog signal. Then this analog signal can be used for measurement on DAQ device. The amplifier includes low-pass filter and the bandwidth of the amplifier is 1 kHz. The specifications of the product are given in the Table A.2.

Table A.2. Electrical specifications of strain gauge amplifier.

PARAMETER	MIN	TYPICAL	MAX	UNIT
Power Supply[6]	14		26	VDC
Current Draw[7]		30		mA
Output Impedance (voltage)		< 1 Ohms		Ohms
Output Impedance (current)			700	Ohms
Sensor Impedance	100			Ohms
Bandwidth	1000		25000	Hz
Common Mode Rejection Ratio	120			dB
Noise		15		mV p-p
Output Span Range	–10		10	% of Rated Output
Output Zero Range	–10		10	% of Rated Output
Gain Drift with Temperature	–25	X	25	PPM of FSR per degree Celsius
Gain Non-Linearity (Better than)	–0.01	X	0.01	% of FSR
Zero Drift with Temperature	–25	X	25	PPM of FSR per degree Celsius

A.3. Sensor Calibration Using Shunt Resistor

Shunt resistor simulates a load on the load cell and this allows to calibrate the torque sensor without applying a load. Before the calibration, all of the connections and switch configurations must be set up and the amplifier must be connected to the DAQ so that the voltage or the current can be read. The steps of calibration with shunt feature:

1. Determine the value of the shunt resistor.
2. Connect the shunt resistor in the spot labeled ‘RSH’.
3. Press the shunt button.
4. Adjust the span with a screwdriver to the expected output, while the shunt is enable.
5. Remove the shunt button and set the voltage and adjust to zero.

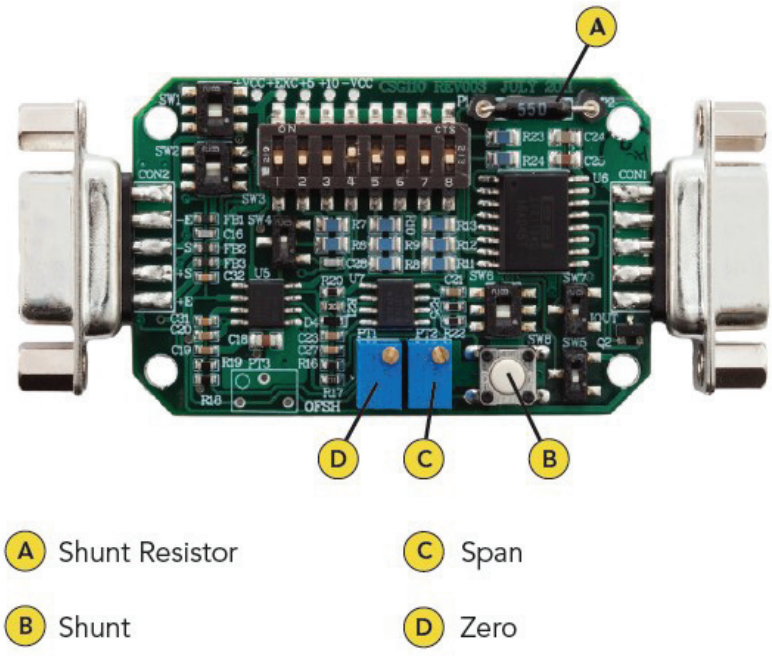

Figure A.2. Shunt resistor button, span and zero pins.

APPENDIX B

National Instruments Data Acquisition Device

B.1. Product Specifications

As a data acquisition device (DAQ), PXI 6229 series I/O module with PXIe-1071 chassis is employed (Figure B.1). PXI analog module has 32 analog input (AI) (16-Bit, 250 kS/s), 4 analog output (AO) and 48 digital input/output (DIO) pins. Also, it has two 32‐bit counter/timers, and digital triggering. The device delivers low-cost, reliable DAQ capabilities in a wide range of applications but particularly for design verification/test, and manufacturing test (National Instruments, 2017).

(a) (b)

Figure B.1. (a) PXIe-1071 chassis, (b) PXI 6229 I/O module
(Source: National Instruments, 2017).

Figure B.2 shows the pinout of the PXI-6229. The I/O signals are available on module with two 68-pin connectors.

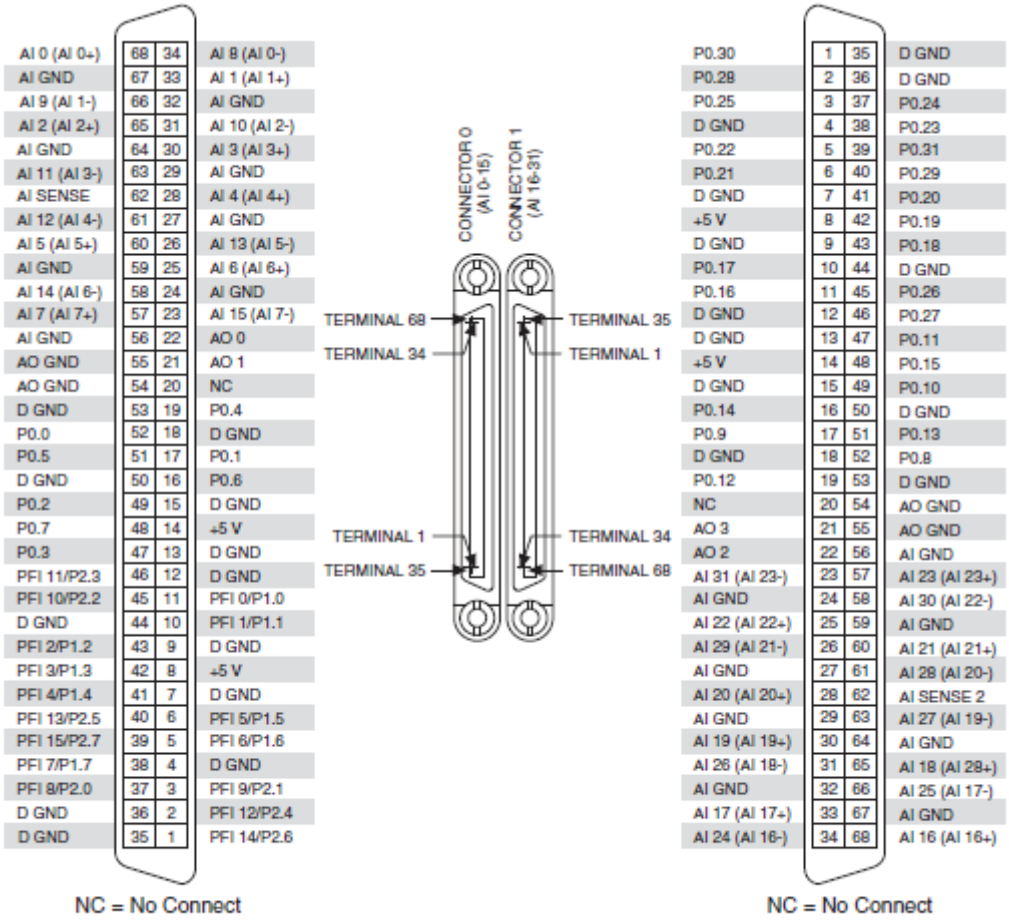

Figure B.2. PXI 6229 Pinout (Source: National Instruments, 2017).

APPENDIX C

FREQUENCY RESPONSE TEST RESULTS

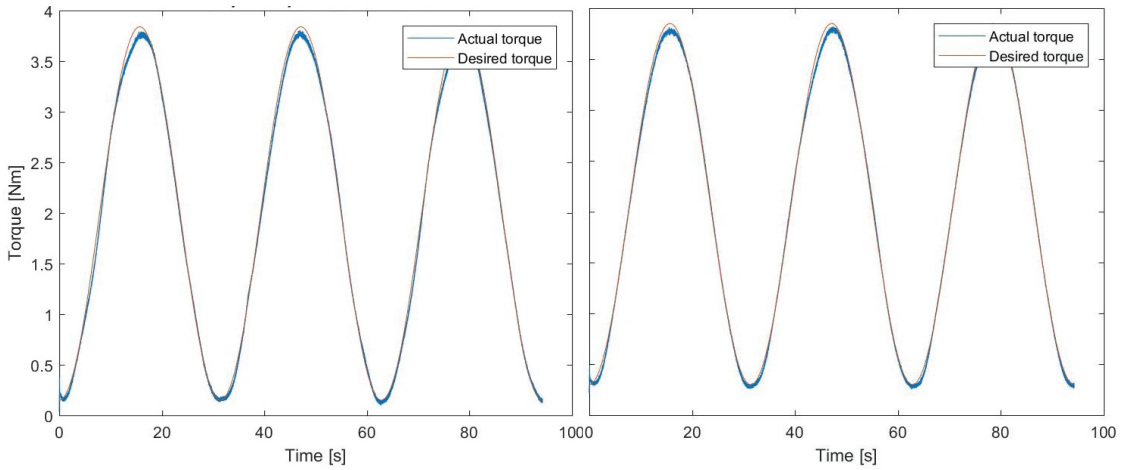

Figure C.1. The frequency of the torque response is 0.2 rad/s; (a) first and (b) second MR brake.

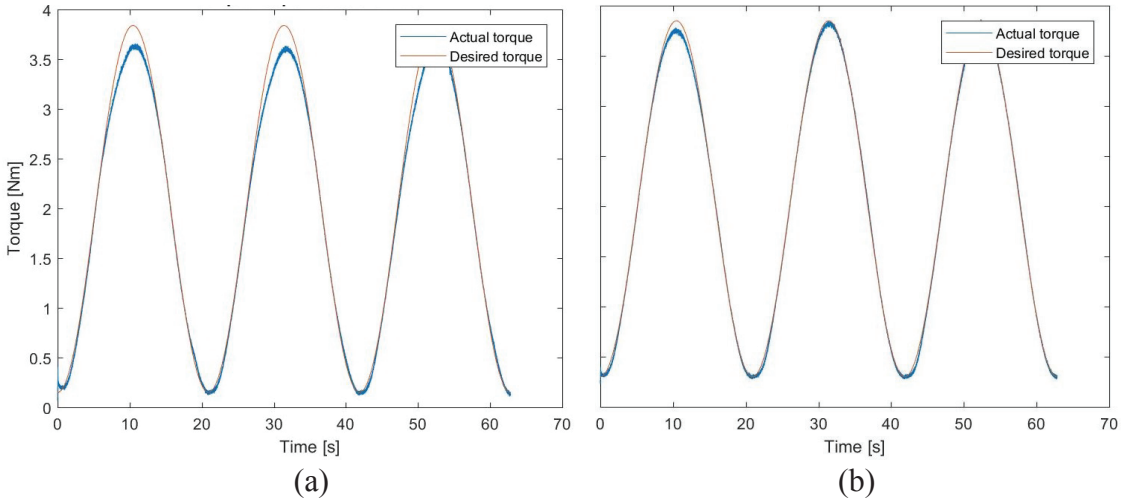

Figure C.2. The frequency of the torque response is 0.3 rad/s; (a) first and (b) second MR brake.

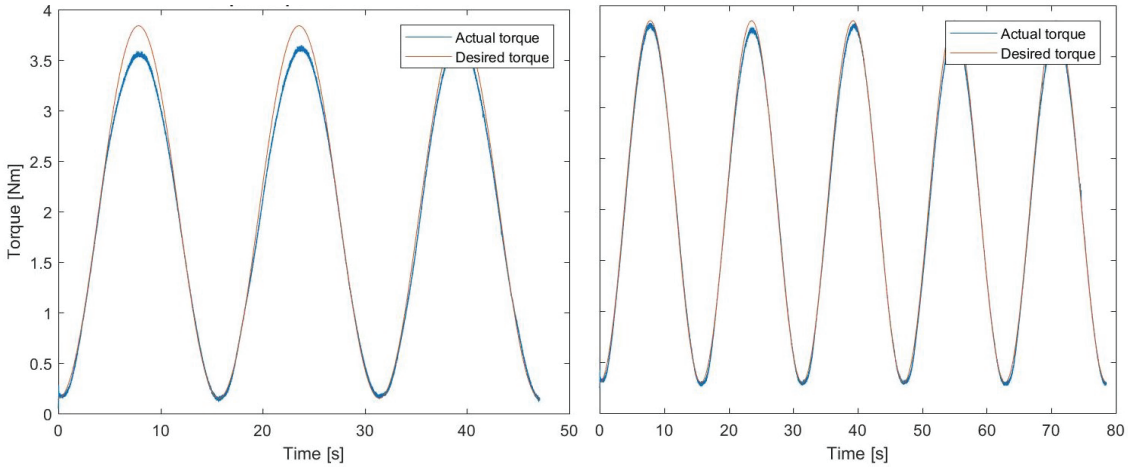

Figure C.3. The frequency of the torque response is 0.4 rad/s; (a) first and (b) second MR brake.

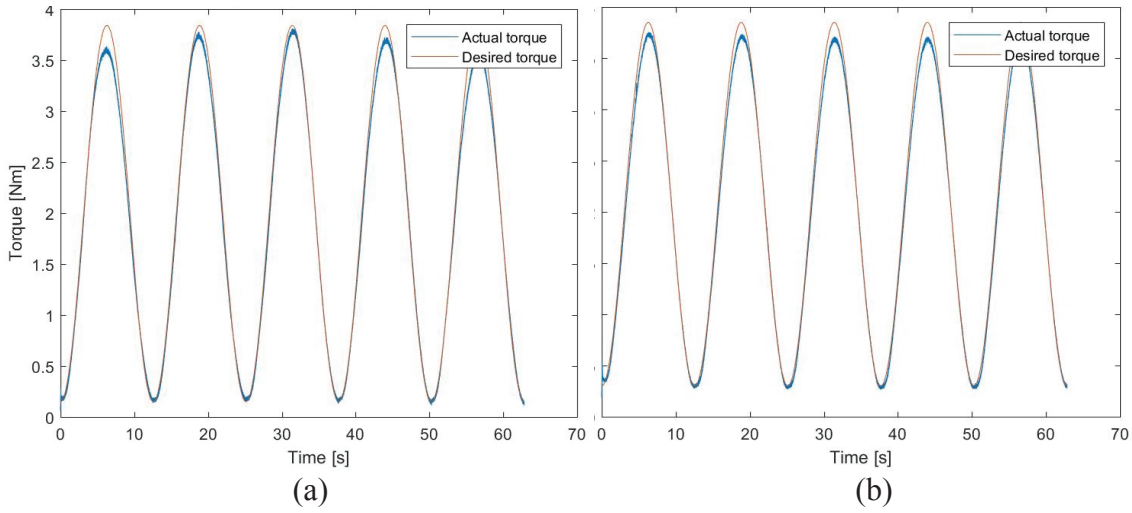

Figure C.4. The frequency of the torque response is 0.5 rad/s; (a) first and (b) second MR brake.

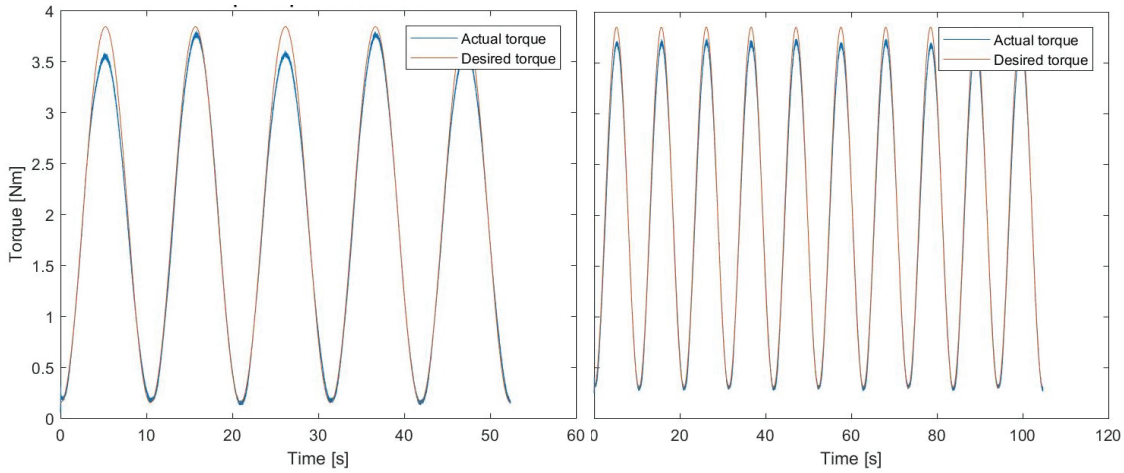

Figure C.5. The frequency of the torque response is 0.6 rad/s; (a) first and (b) second MR brake.

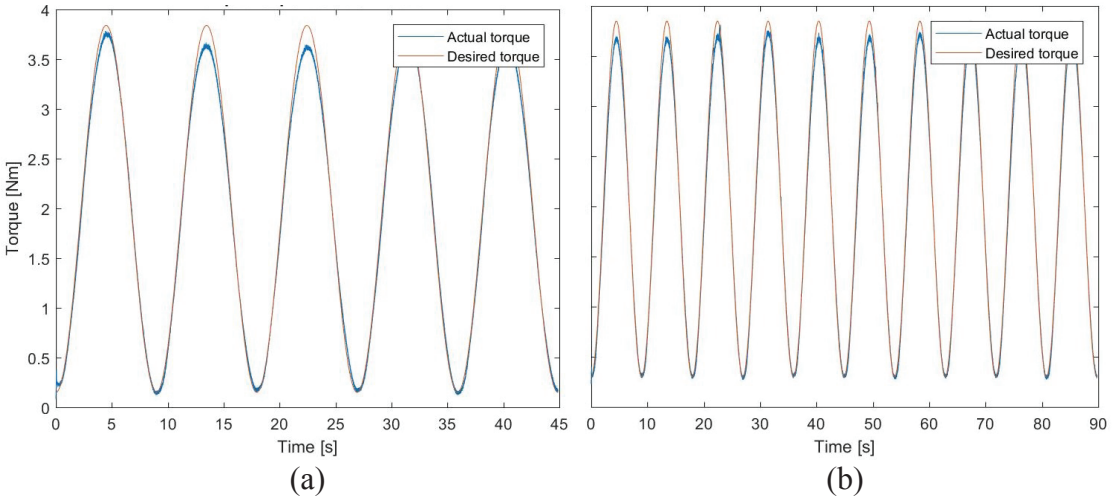

Figure C.6. The frequency of the torque response is 0.7 rad/s; (a) first and (b) second MR brake.

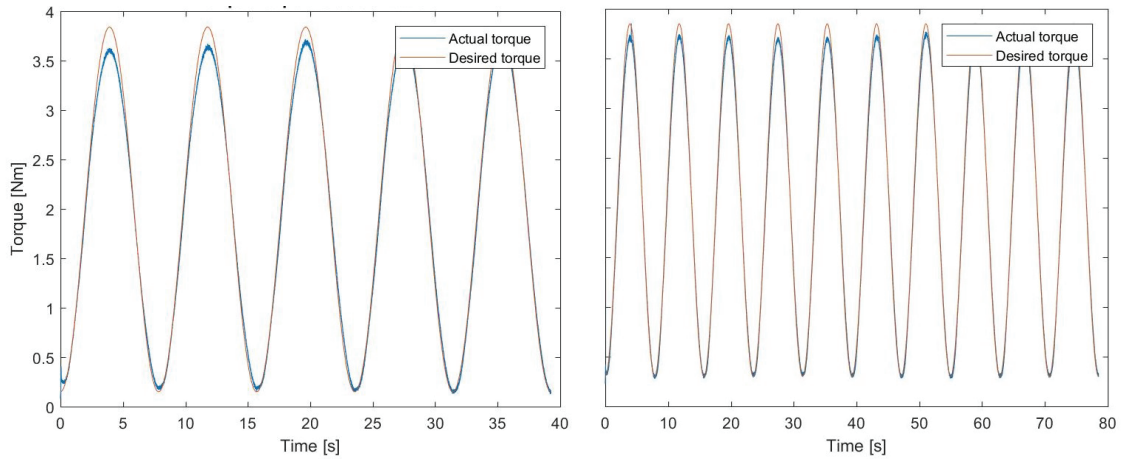

(a) (b)

Figure C.7. The frequency of the torque response is 0.8 rad/s; (a) first and (b) second MR brake.

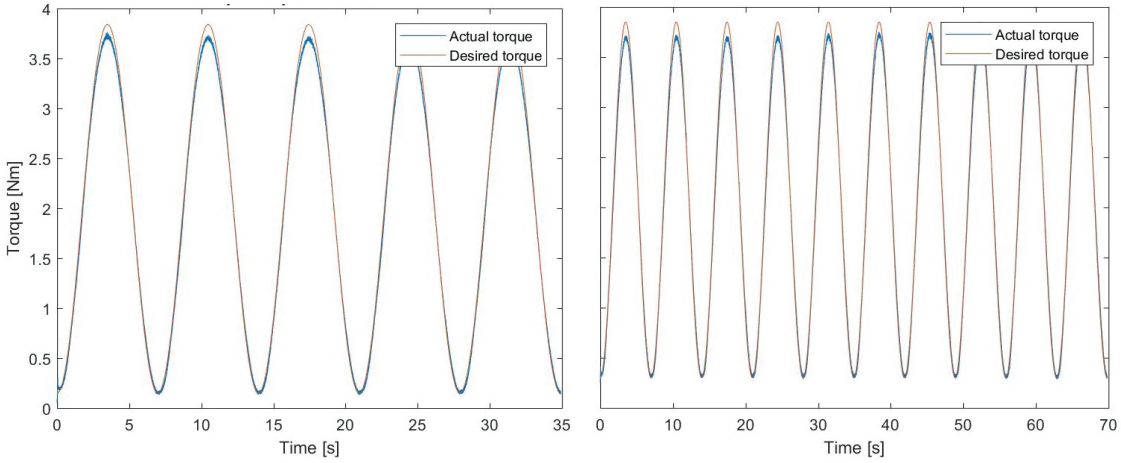

(a) (b)

Figure C.8. The frequency of the torque response is 0.9 rad/s; (a) first and (b) second MR brake.

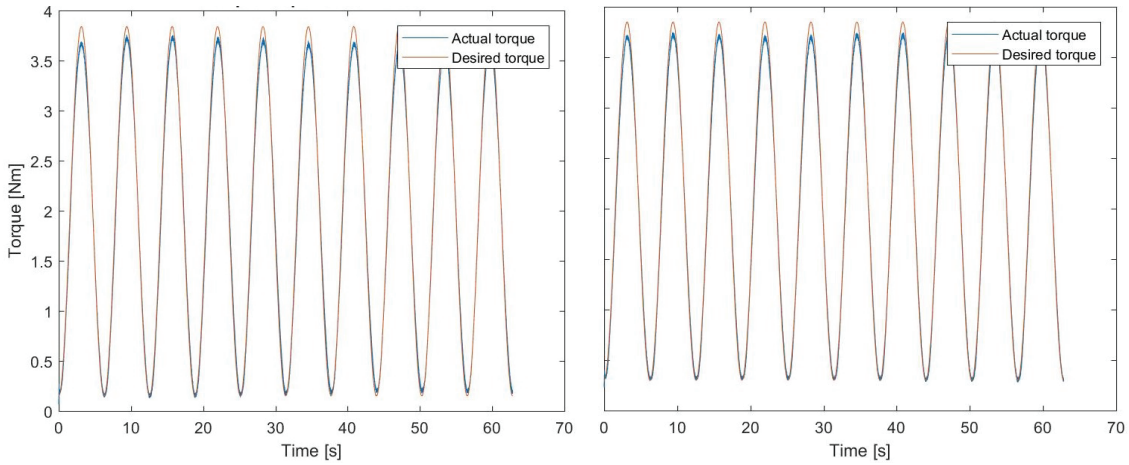

Figure C.9. The frequency of the torque response is 1 rad/s; (a) first and (b) second MR brake.

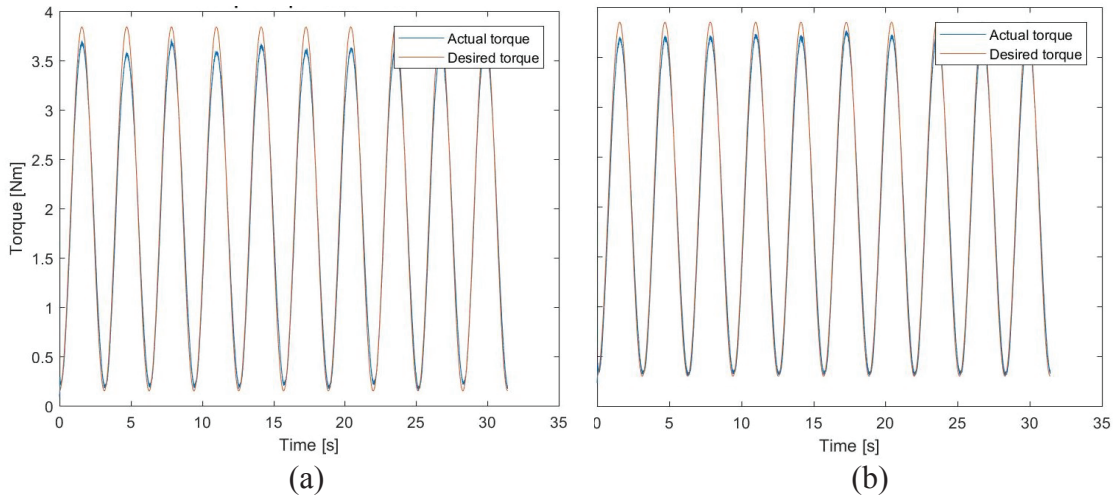

Figure C.10. The frequency of the torque response is 2 rad/s; (a) first and (b) second MR brake.

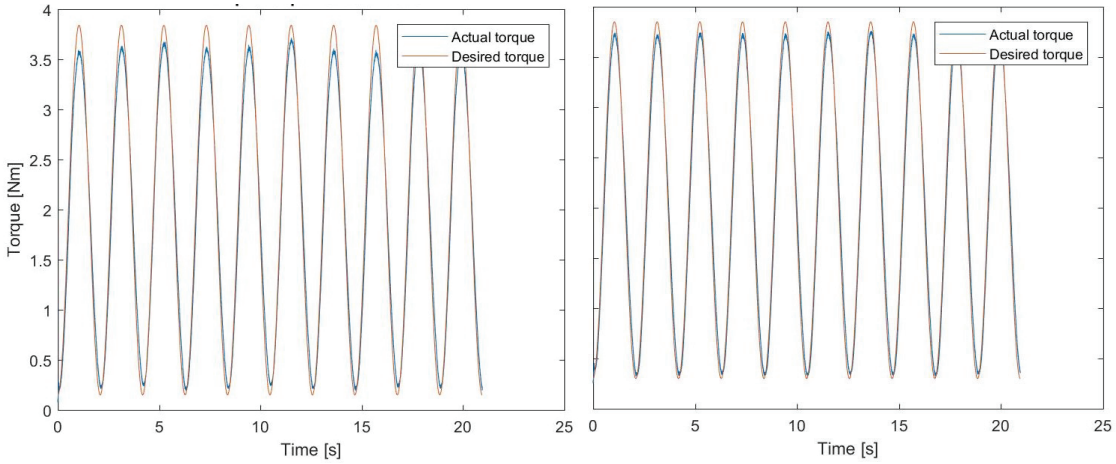

Figure C.11. The frequency of the torque response is 3 rad/s; (a) first and (b) second MR brake.

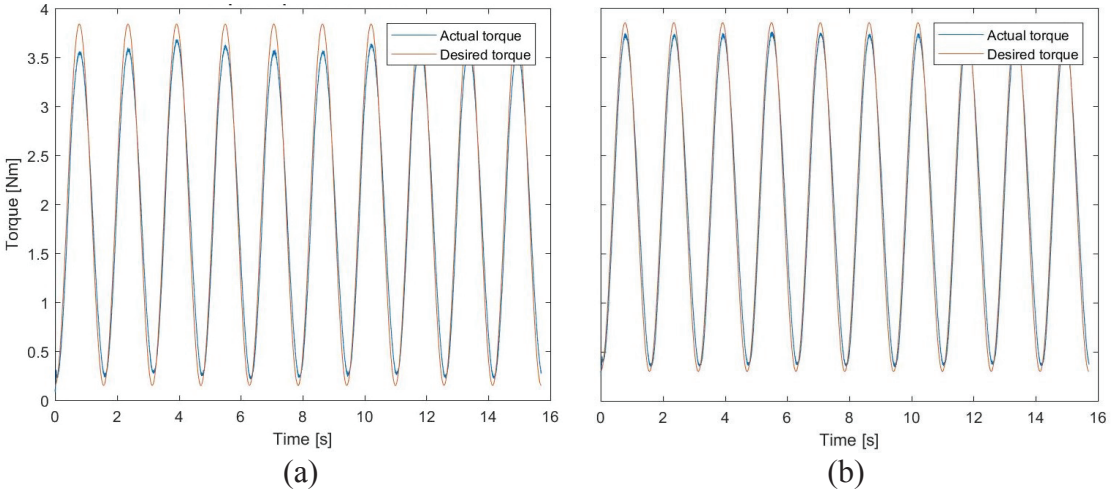

Figure C.12. The frequency of the torque response is 4 rad/s; (a) first and (b) second MR brake.

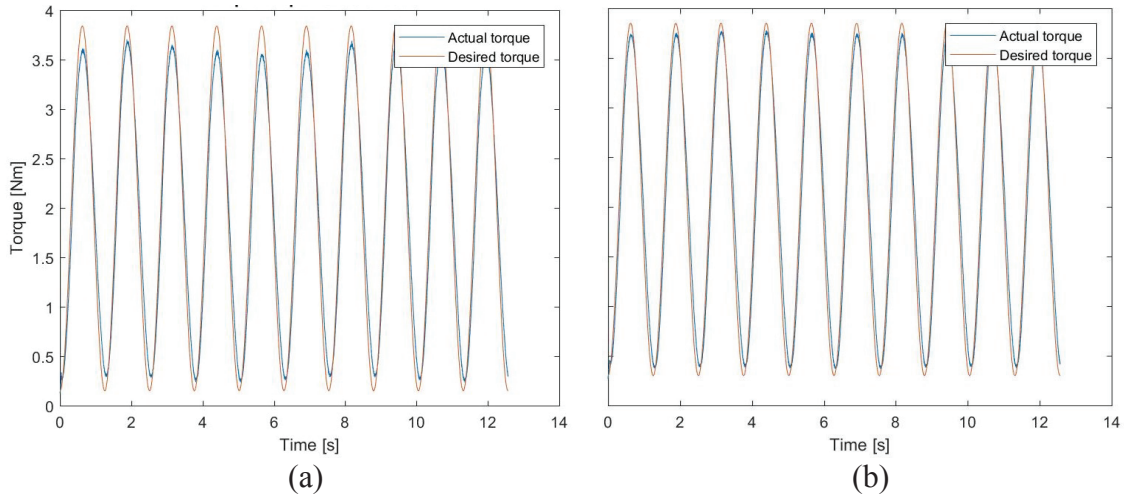

Figure C.13. The frequency of the torque response is 5 rad/s; (a) first and (b) second MR brake.

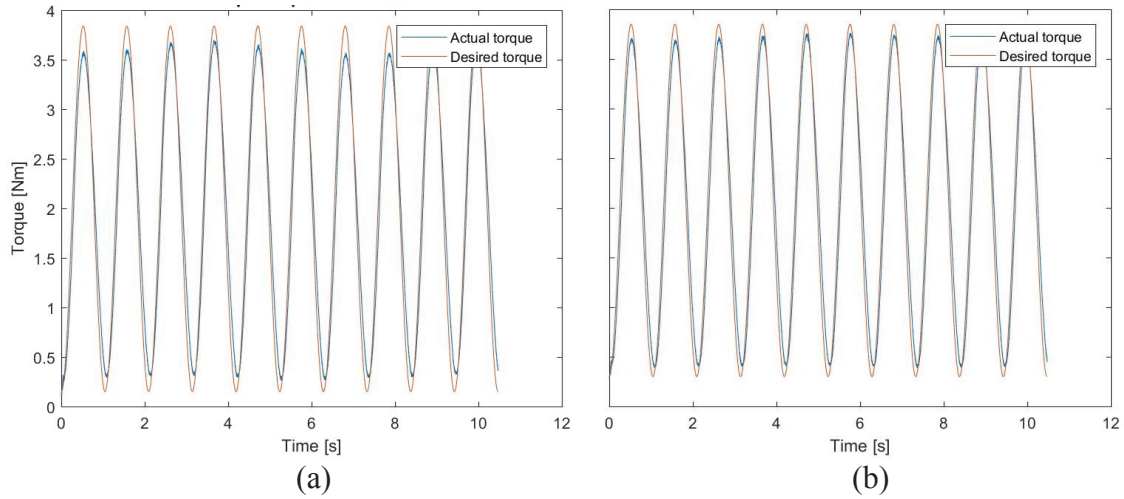

Figure C.14. The frequency of the torque response is 6 rad/s; (a) first and (b) second MR brake.

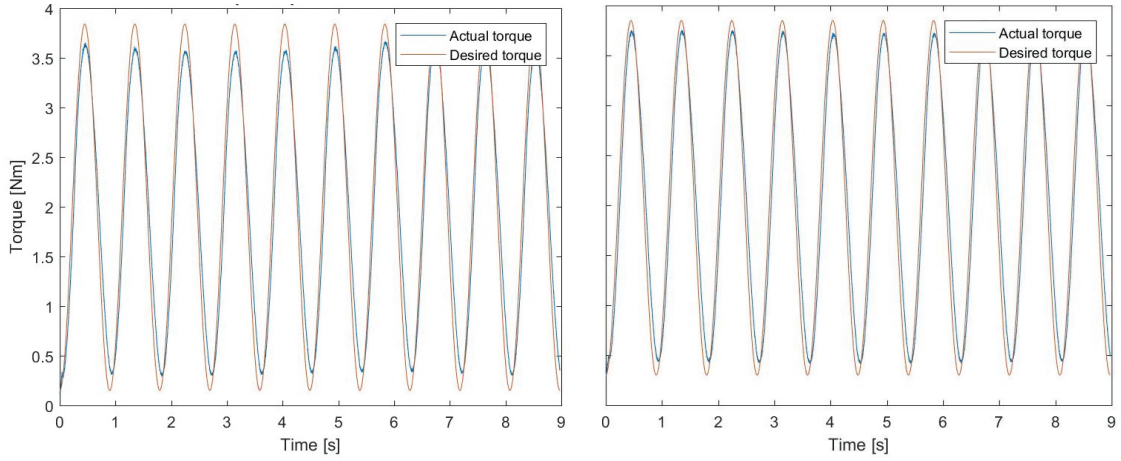

Figure C.15. The frequency of the torque response is 7 rad/s; (a) first and (b) second MR brake.

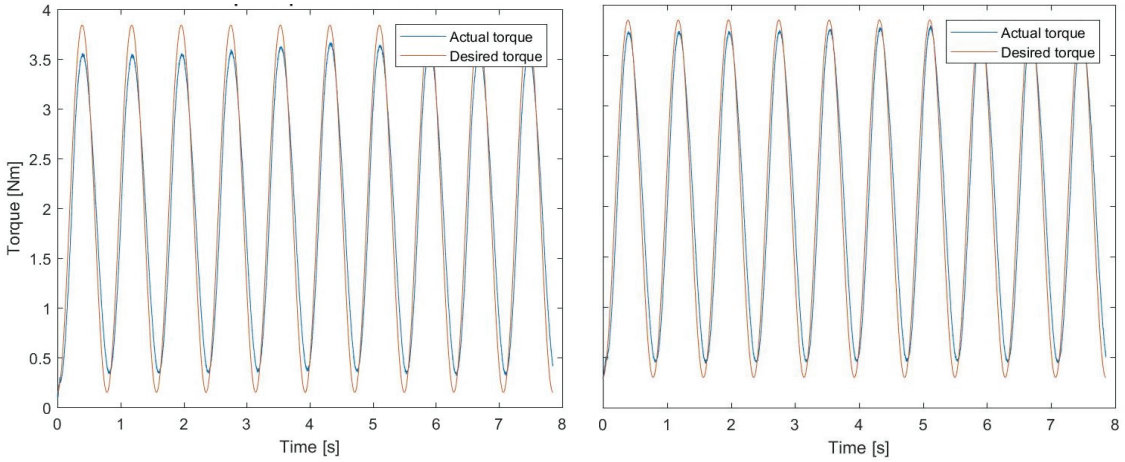

Figure C.16. The frequency of the torque response is 8 rad/s; (a) first and (b) second MR brake.

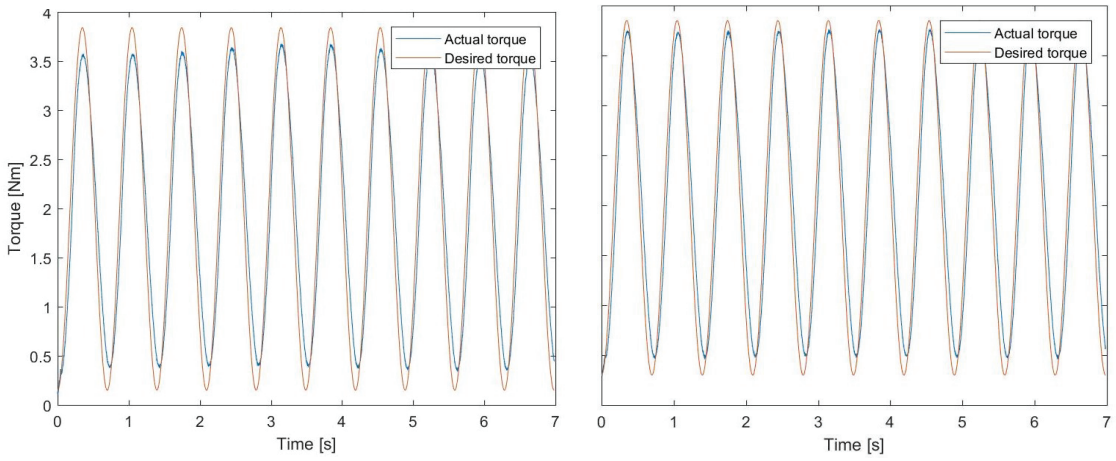

Figure C.17. The frequency of the torque response is 9 rad/s; (a) first and (b) second MR brake.

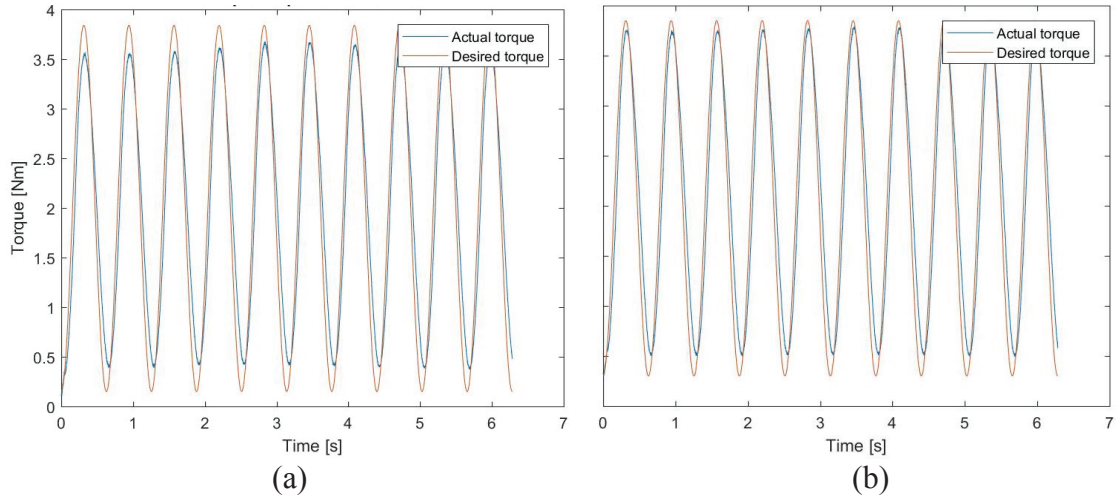

Figure C.18. The frequency of the torque response is 10 rad/s; (a) first and (b) second MR brake.

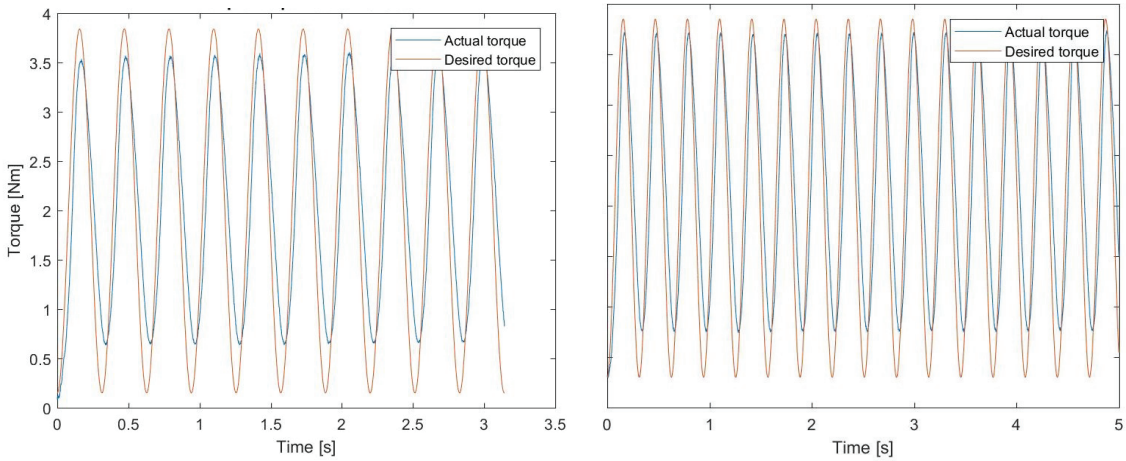

Figure C.19. The frequency of the torque response is 20 rad/s; (a) first and (b) second MR brake.

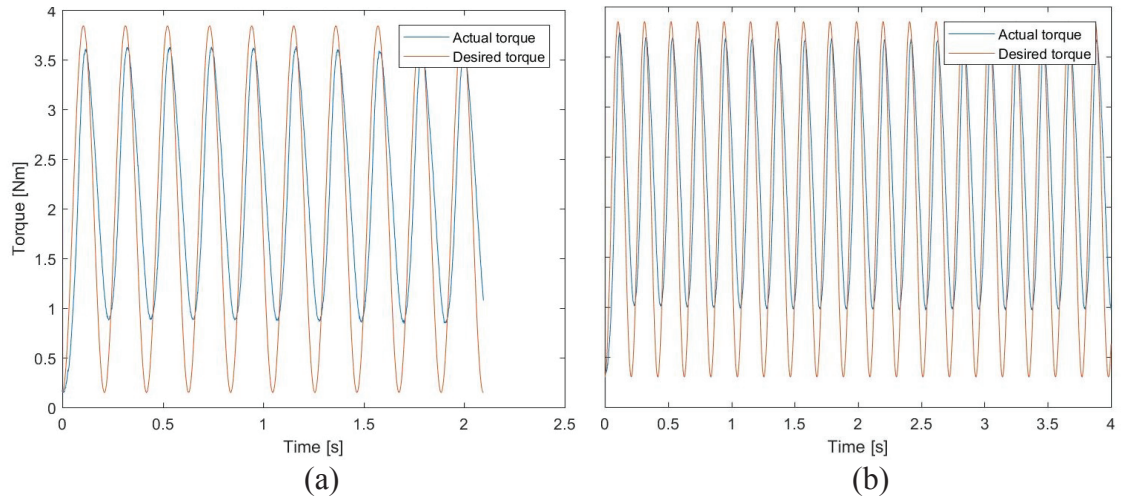

Figure C.20. The frequency of the torque response is 30 rad/s; (a) first and (b) second MR brake.

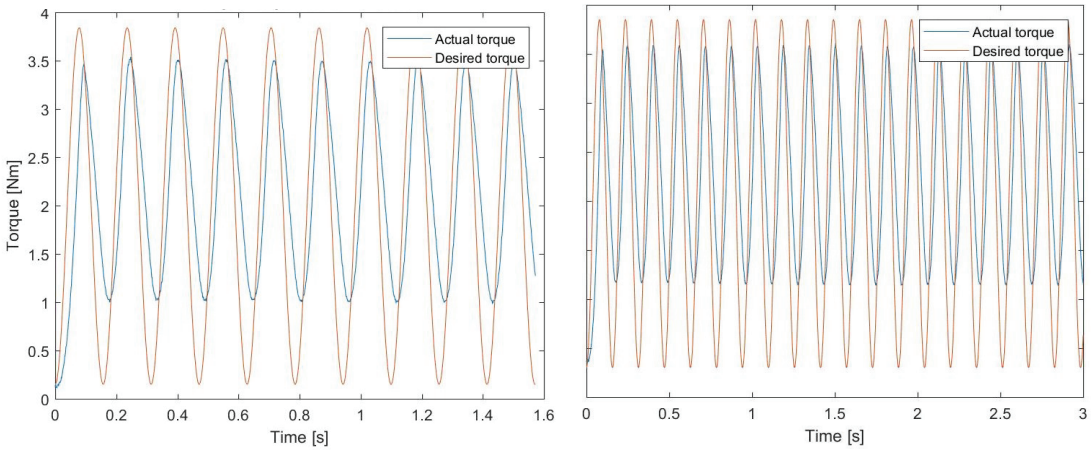

Figure C.21. The frequency of the torque response is 40 rad/s; (a) first and (b) second MR brake.

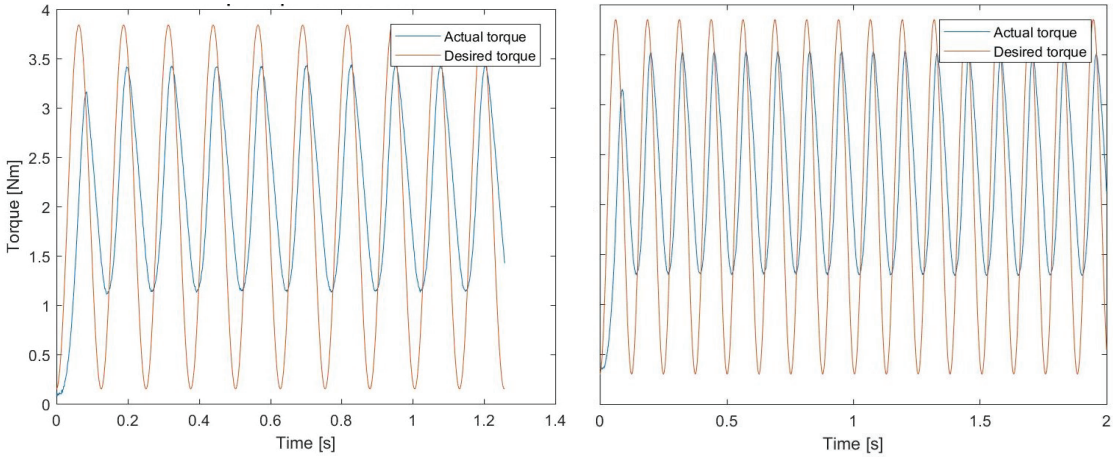

Figure C.22. The frequency of the torque response is 50 rad/s; (a) first and (b) second MR brake.

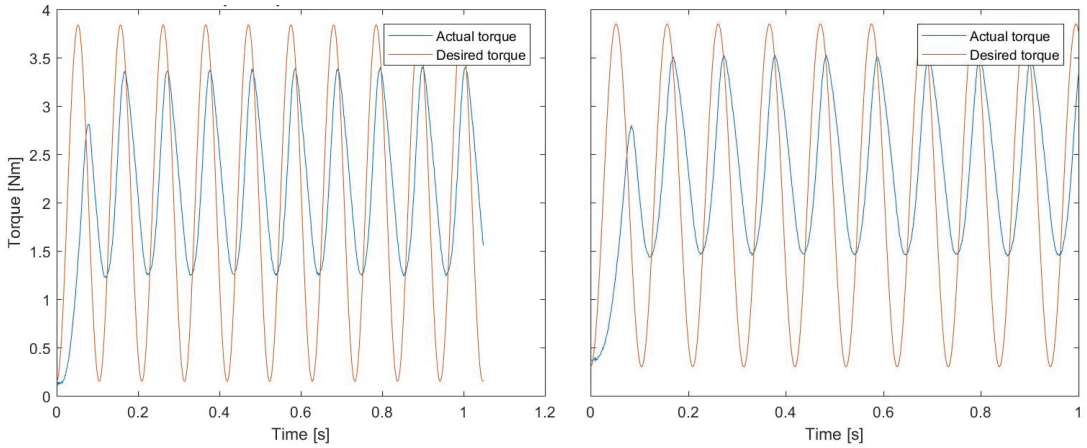

(a) (b)

Figure C.23. The frequency of the torque response is 60 rad/s; (a) first and (b) second MR brake.

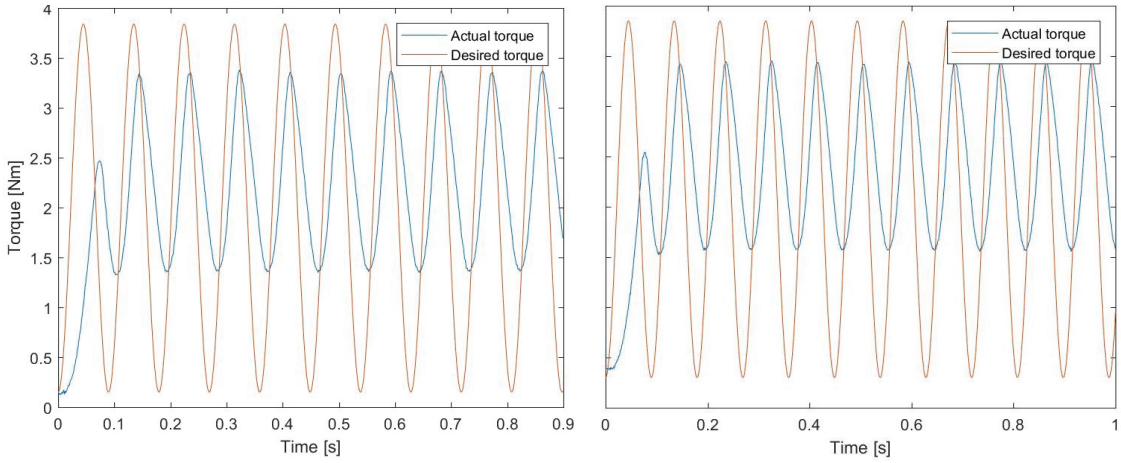

(a) (b)

Figure C.22. The frequency of the torque response is 70 rad/s; (a) first and (b) second MR brake.

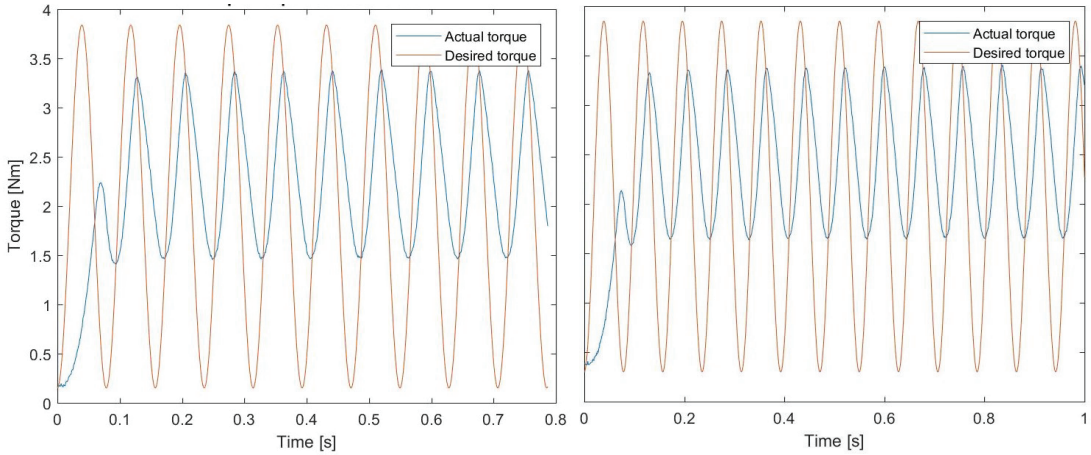

Figure C.23. The frequency of the torque response is 80 rad/s; (a) first and (b) second MR brake.

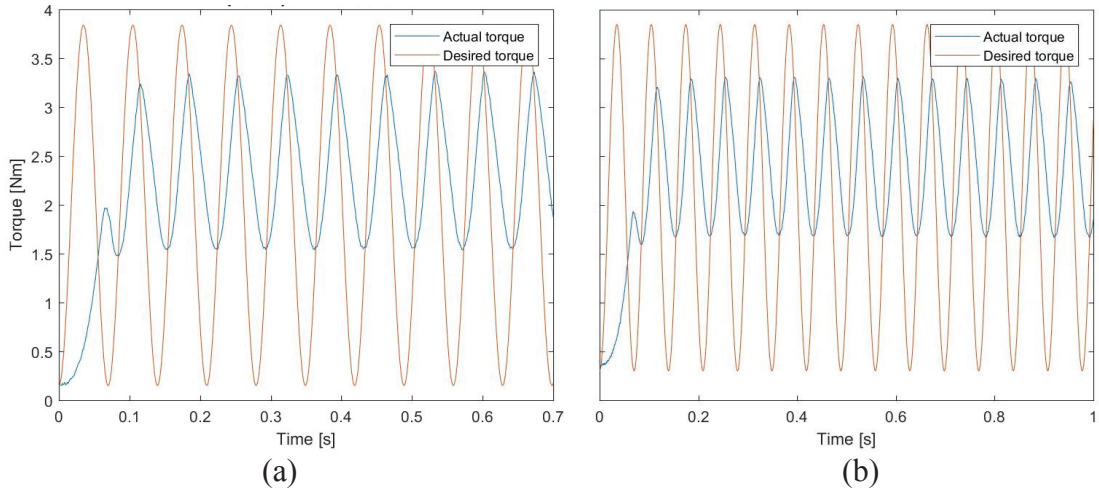

Figure C.24. The frequency of the torque response is 90 rad/s; (a) first and (b) second MR brake.

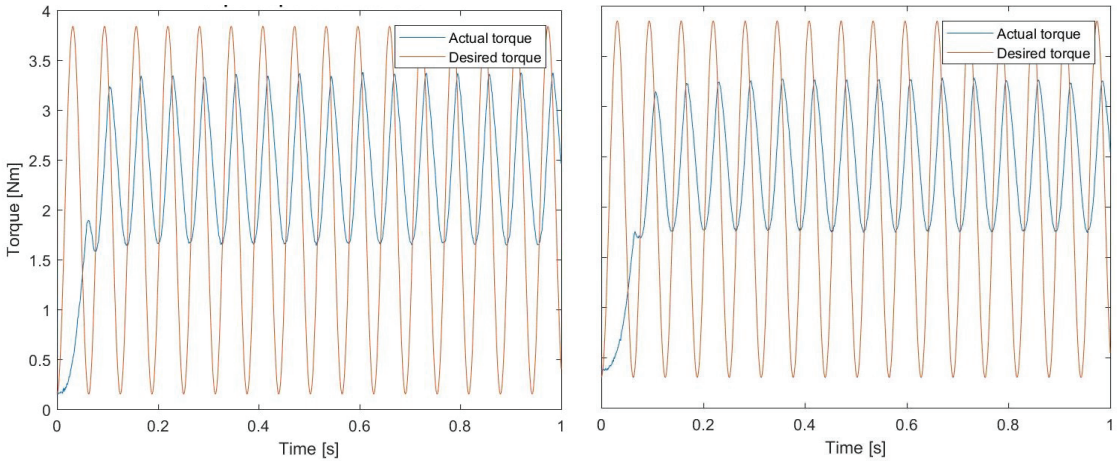

(a) (b)

Figure C.25. The frequency of the torque response is 100 rad/s; (a) first and (b) second MR brake.

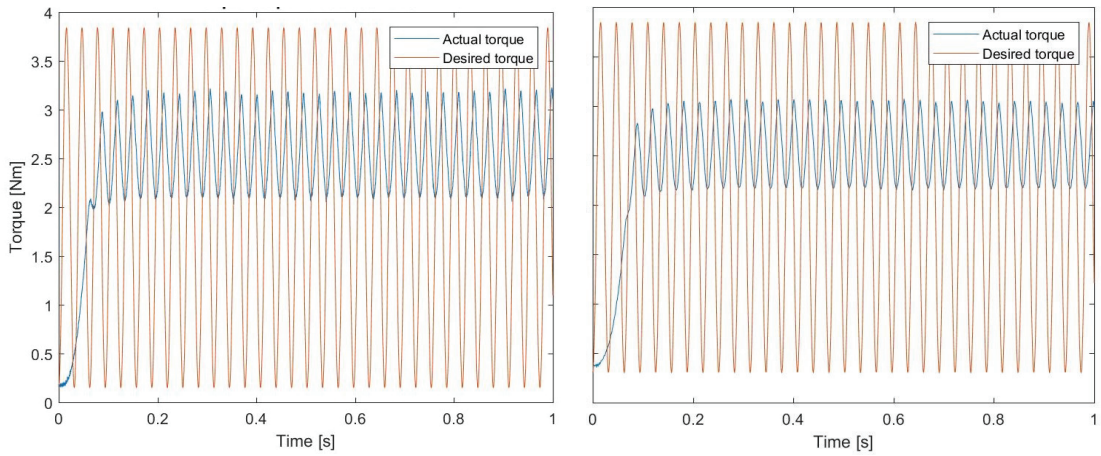

(a) (b)

Figure C.26. The frequency of the torque response is 200 rad/s; (a) first and (b) second MR brake.

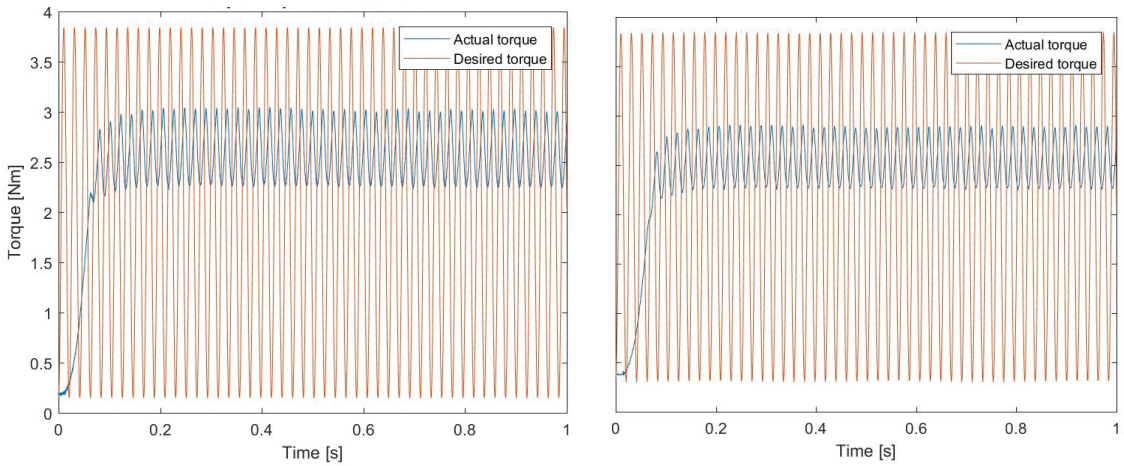

Figure C.27. The frequency of the torque response is 300 rad/s; (a) first and (b) second MR brake.

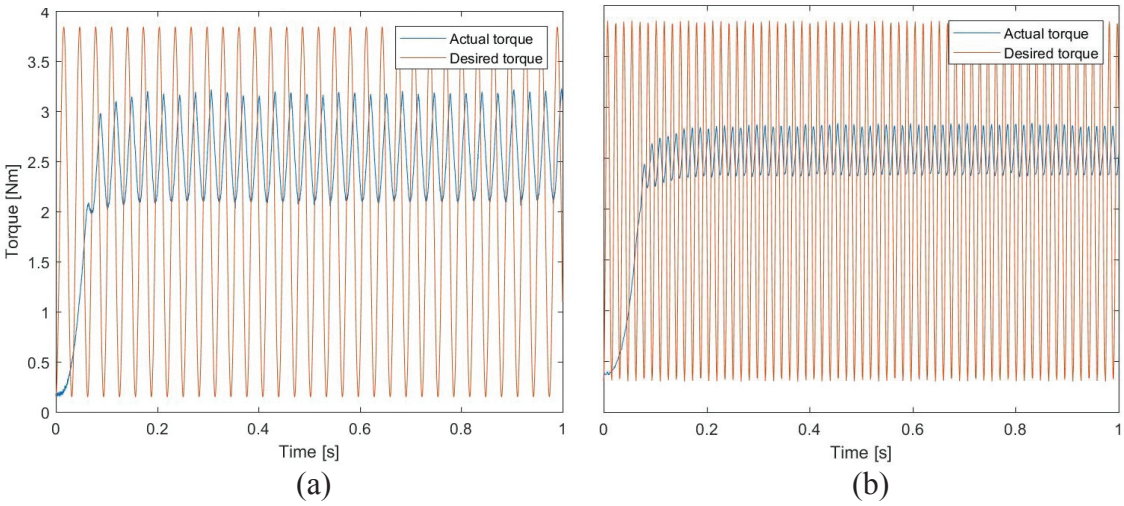

Figure C.28. The frequency of the torque response is 400 rad/s; (a) first and (b) second MR brake.

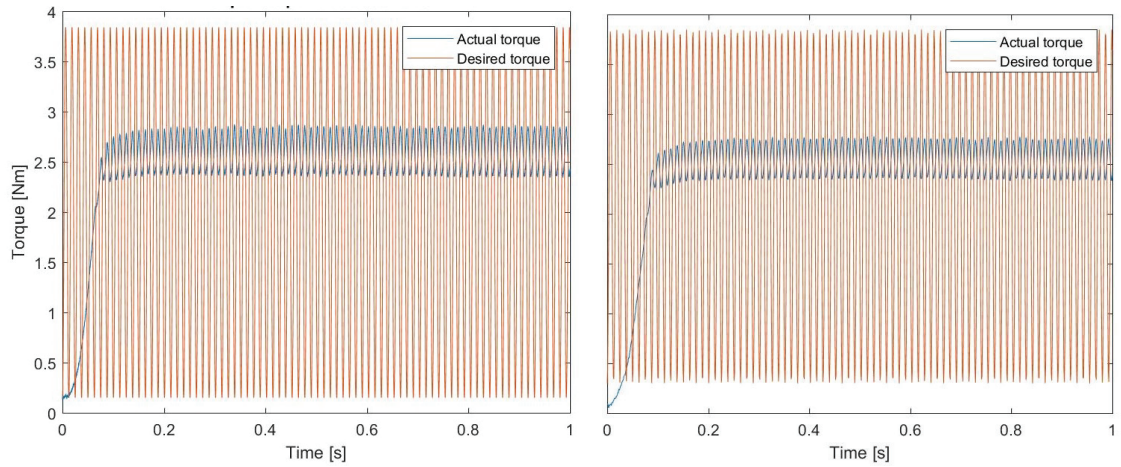

Figure C.29. The frequency of the torque response is 500 rad/s; (a) first and (b) second MR brake.

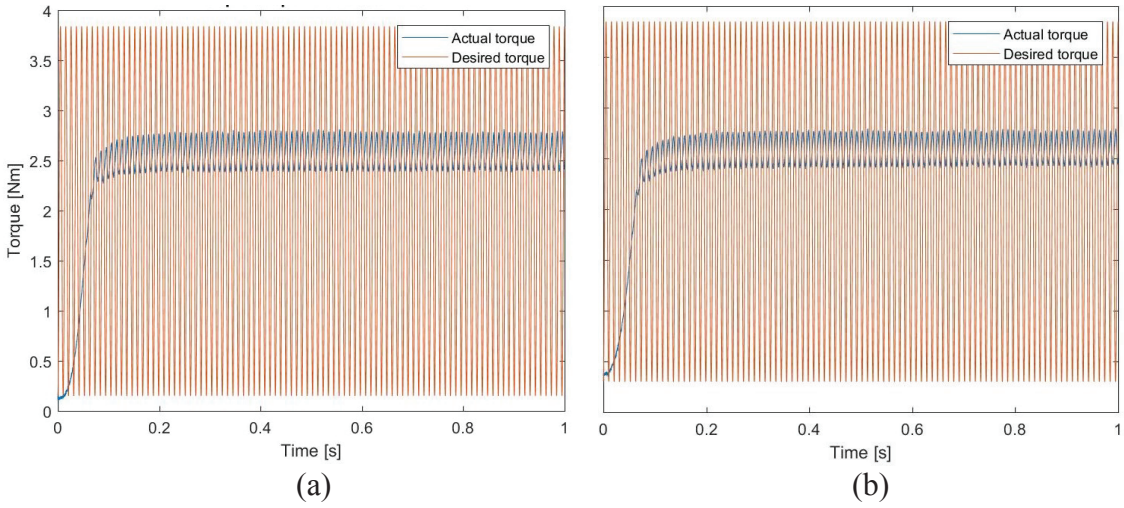

Figure C.30. The frequency of the torque response is 600 rad/s; (a) first and (b) second MR brake.

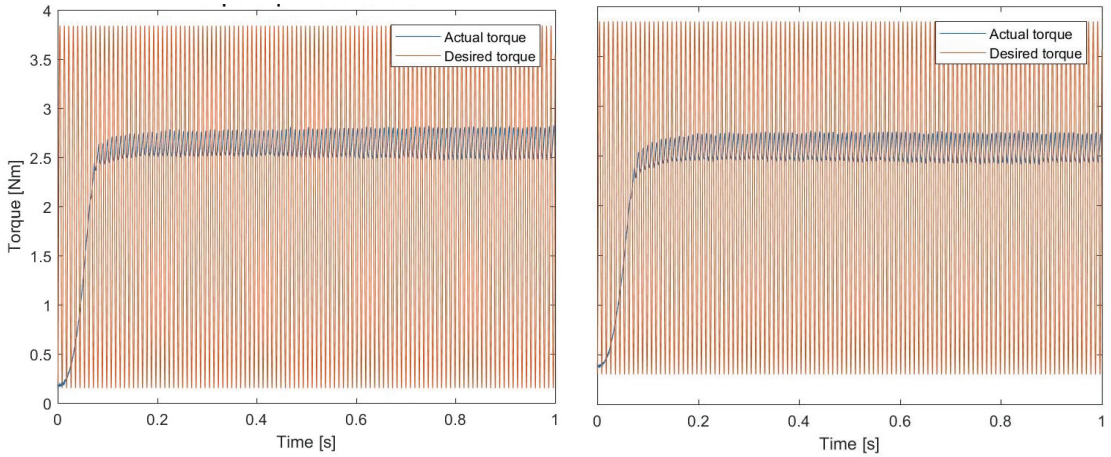

(a) (b)

Figure C.31. The frequency of the torque response is 700 rad/s; (a) first and (b) second MR brake.

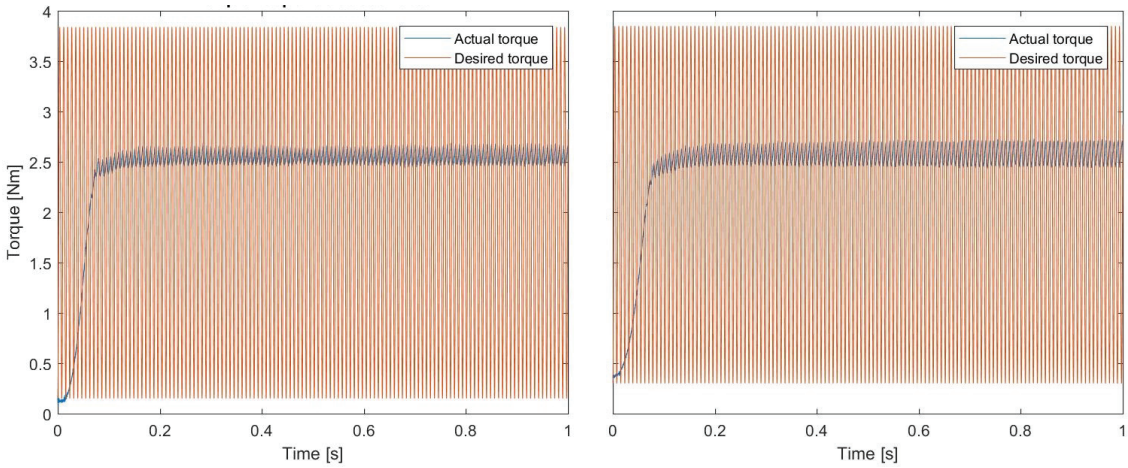

(a) (b)

Figure C.32. The frequency of the torque response is 800 rad/s; (a) first and (b) second MR brake.

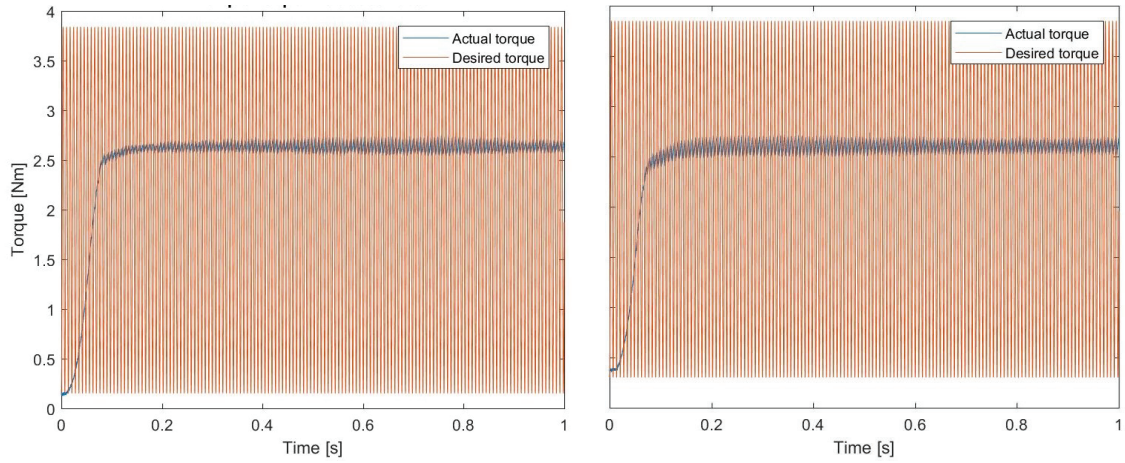

(a) (b)

Figure C.33. The frequency of the torque response is 900 rad/s; (a) first and (b) second MR brake.

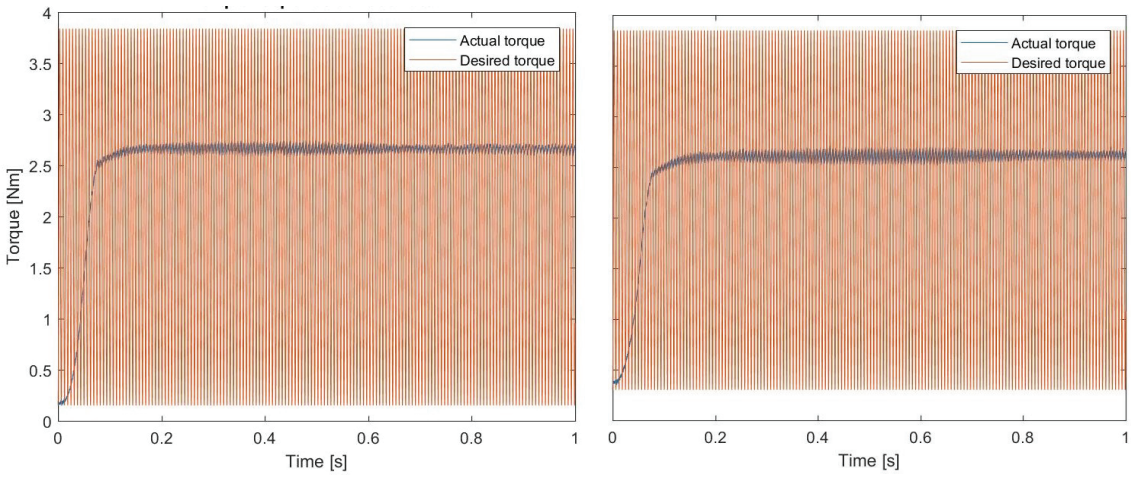

(a) (b)

Figure C.34. The frequency of the torque response is 1000 rad/s; (a) first and (b) second MR brake.